The Dissertation Committee for Morgann Elizabeth Berg certifies that this is the approved version of the following dissertation:

Magnetic Force Microscopy Studies of Magnetic Domain Structure in $LaCoO_3$ and UMn_2Ge_2

Committee:

Alejandro L. de Lozanne, Supervisor

John T. Markert

Maxim Tsoi

Zhen Yao

Jianshi Zhou

Magnetic Force Microscopy Studies of Magnetic Domain Structure in $LaCoO_3$ and UMn_2Ge_2

by

Morgann Elizabeth Berg, B. S. Phy.

Dissertation

Presented to the Faculty of the Graduate School of

The University of Texas at Austin

in Partial Fulfillment

of the Requirements

for the Degree of

Doctor of Philosophy

The University of Texas at Austin

December, 2014

Dedication

This dissertation is dedicated to my parents and to my families- the one I was blessed with, the ones I chose and the ones who chose me. But most especially this dissertation is dedicated to my son Devin. Of all the support I have received from family and friends this dissertation probably asked the most from him. He is the light that will light me up from within always.

Acknowledgements

I would like to thank my advisor Alex for so many things, but especially for his patience which I think I tested often. I thank him for welcoming me into his group and being a constant presence along my (sometimes meandering) path through doctoral research. There is a great deal about his methodology to admire and his example will always be something I look to.

It feels like the amazing people I have worked with are too long to list, but I will do my best. Dr. Jeehoon Kim and Dr. Suenne Kim as graduate students working in Alex's lab were my first mentors in the laboratory and were extremely generous with their time and practical instruction in all lab matters and also their friendship. Jeehoon brings an unparalleled enthusiasm to his work, is full of good ideas, and remains an exemplary figure for me to this day. Dr.'s Casey Israel, Tien-Ming (Ming) Chuang, Junwei Huang, Changbae Hyun, and Seongsoo Kweon are dedicated and talented researchers who were delightful to work with. Dr. Alfred Lee first introduced me to Ming's design for an atomic force microscope as a new graduate student and I took everything he said to heart. I couldn't have asked for a better teacher about the ins and outs of the design or for a better example of citizenship in the lab, in research and in the NSF IGERT traineeship in which we both served. As some of his fardels became mine, I admire his canny critical-thinking, humor and enlightened way of being. Dr. Neliza Leon-Brito who also trained with me became a cherished companion who brought deliberation and pragmatism and a self-abnegating devotion to her work in addition to a wonderfully unique perspective. Dr. Frank Ruzicka really warmed up the lab and rounded out the group with his positivity, humor and humanity. I keenly miss working with all of

them and eagerly anticipate their continued success. I am brimming with warmth and pride as I get to name them all by the titles they earned.

Leu-Jen Chen who arrived not much later than Neliza and I has applied himself most dedicatedly to the construction and operation of the spin-polarized scanning tunneling microscope. It is amazing to hear him play classical guitar. Xinzhou Tan, the newest addition to our lab, is an especially eager problem-solver who has already accomplished so much and I anticipate that he will accomplish much more. I wish them all the best in their endeavors.

Many thanks to the architects of the Atomic and Molecular Imaging of Interfaces and Defects IGERT program in which Alfred, Neliza and I and many others participated and to Annie Harding, the IGERT program coordinator and indefatigable motor who drove us all forward. It was a bright spot in my graduate career to work with Prof. Shih, Annie and the cohort of student researchers and wonderful people who I consider my comrades, namely, Alex, Carol, Charlotte, Chris, Guru, Julian, Micah, Michael, and Sarah. In addition to Prof. Shih's tireless dedication to the success of the IGERT program, I appreciate his patience tolerating my use of his lab's commercial scanning probe microscope and his encouragement throughout the IGERT program and my graduate career.

Professor Markert's group first introduced me to SQUID magnetometry and I am indebted to Mark Monti, Isaac Manzanera, and Jeremy Paster for all their help and advice and neighborliness. Extremely helpful discussions with Professor Markert regarding all sorts of magnetic behavior and his guidance from as early as my undergraduate work are invaluable to me. I am deeply humbled by the breadth of Dr. Zhou's knowledge of materials and experiment which made his willingness to help fill in critical gaps left in

my training a revelation to me. I cannot possibly be more grateful for his help. Prof. Demkov sparked my interest in $LaCoO_3$ and allowed me the opportunity to train on molecular beam epitaxy with his very talented and eminently capable post-doc Dr. Agham Posadas. Where my committee members have served as mentors and sounding boards during my graduate research, Agham has been something of a co-mentor who I have truly enjoyed working with and sharing research. Prof. Demkov is an exceptionally shrewd individual and gifted investigator who, with remarkable proficiency, leads a group of bright individuals hot on the trail of complex oxides. I am lucky to have collaborated with them, playing a guest role in their group at times.

My friends and loved ones have doled out a great deal of support and withstood a lot of non-communication while I labored in the shadow of exceptional individuals and researchers to find my own way to proficiency in research. I'm so grateful for their openhandedness and fortitude and I couldn't have accomplished this without them.

Paraphrasing these acknowledgements, it really does take a village to raise a physicist.

Magnetic Force Microscopy Studies of Magnetic Domain Structure in $LaCoO_3$ and UMn_2Ge_2

Morgann Elizabeth Berg, Ph. D.

The University of Texas at Austin, 2014

Supervisor: Alejandro L. de Lozanne

Magnetic force microscopy studies in varying temperature and applied external magnetic field of magnetic thin films of $LaCoO_3$ under strain and single crystal UMn_2Ge_2 have been performed. In the case of $LaCoO_3$ thin films the aim is an understanding of the response of the magnetic microstructure to different signs and degrees of strain and a further attempt to distinguish the effect of defects from strain-induced effects. In UMn_2Ge_2 the magnetic microstructure is imaged for the first time and signatures of a possible phase transition at 150 K and crystalline anisotropy are explored. The first portion of this dissertation focuses on the synthesis methods used to produce the samples investigated and the critical role of synthesis in producing high-quality samples. This is followed by a discussion of characterization techniques used to obtain local and global magnetic and structural characteristics, with particular emphasis on magnetic force microscopy including noise characteristics and a discussion of achieving a high force gradient sensitivity by optimizing the fiber-optic interferometer used for cantilever deflection detection. Design elements and features of the multi-mode variable-temperature atomic force microscope used to obtain magnetic force microscopy images are presented and results for $LaCoO_3$ and UMn_2Ge_2 are discussed.

Table of Contents

List of Tables

List of Figures

Chapter 1: Introduction

Complex functional materials feature competing microscopic phases that contrive to alter the macroscopic state of a material. They exhibit exotic behavior and play an especially critical role in the evolution of today's technology. Superconducting, multiferroic and magnetoresistive materials are most readily identified as complex functional materials but the response of magnetic domains to temperature and applied field that affects the macroscopic state of a ferromagnet qualifies ferromagnets as complex functional materials as well. To better understand the microscopic interactions that give rise to this complexity it is not sufficient to rely solely on macroscopic measurement and we must be able to probe these interactions locally.

One major breakthrough in direct measurement of local interactions came with the introduction of scanning probe microscopy (SPM) inaugurated by the invention of the scanning tunneling microscope (STM) in 1984. The techniques and technical refinements which followed the invention of the STM enabled mapping of surface topography for both conducting and insulating surfaces at the atomic scale and mapping long-range magnetic and electrostatic interactions. Key technical adaptations which allowed for SPM measurement in various environments have enabled surface mapping of complex functional materials at low-temperatures and applied electric and magnetic fields to probe the behavior of microscopic domains as they vary across phase transitions. Magnetic force microscopy (MFM), a flavor of SPM utilized for this thesis work, is a particularly useful technique for imaging magnetic domains across phase transitions and has been applied to two complex functional materials of interest, $LaCoO_3$ and UMn_2Ge_2.

A significant contribution to micro- and macroscopic electronic properties of complex functional materials can originate from defect structures and chemical inhomogeneity introduced during synthesis and post-synthesis treatments (e. g. annealing). For this reason, methods of synthesis and post-synthesis processing must be carefully chosen and optimized. In order to ensure deposition of high-quality crystalline thin film samples of $LaCoO_3$ molecular beam epitaxy was used.

Chapters 2 and 3 of this thesis will deal with sample fabrication and characterization techniques, including the basic principles of magnetic force microscopy, resolution and noise considerations. Chapter 4 describes design and operation details for components of a home-built multi-mode variable-temperature atomic force microscope (VT-AFM) used to obtain the MFM results featured in this thesis. Following the description of the VT-AFM, I will present MFM results for $LaCoO_3$ and UMn_2Ge_2. The first samples examined are thin films of $LaCoO_3$ strained to various substrates. Using MFM, we are able to image the magnetic domain rearrangement over the ferromagnetic to paramagnetic phase transition in films deposited on $SrTiO_3$-buffered Si (100), $BaTiO_3$-terminated $SrTiO_3$-buffered Si (100) and a commercial $LaAlO_3$ substrate. The results will be discussed in Chapter 5.

The second sample is a single crystal sample of the permanent magnetic material UMn_2Ge_2. There are indications of a possible structural transition concurrent with magnetic ordering of the uranium sublattice, but until this study no microscopic imaging of domain structure and domain evolution across this transition has been performed. Indications of uniaxial anisotropy are demonstrated by comparison of MFM images of UMn_2Ge_2 to Kerr effect measurements on $Nd_2Fe_{14}B$. With the aid of Laue diffraction

results for the sample the anisotropy direction is determined. The results and discussion of UMn_2Ge_2 will be presented in Chapter 6.

Chapter 2: Sample Fabrication Methods

This chapter discusses the fabrication techniques used to generate the materials featured in this work, that is, growth of $LaCoO_3$ thin films using molecular beam epitaxy (MBE) and synthesis of UMn_2Ge_2 plates via a flux-assisted molten reaction. In the case of MBE a broad description of reflection high-energy electron diffraction (RHEED) characterization employed in tandem to synthesis is included, as well as a brief discussion of other synthesis methods typically used to produce samples of $LaCoO_3$.

2.1 Molecular Beam Epitaxy

The $LaCoO_3$ (LCO) films featured in this study were grown via molecular beam epitaxy (MBE). MBE is accomplished by thermal evaporation of high purity elemental sources in a high vacuum environment which generates beams of molecules. These molecular beams react at the sample surface to form the desired materials. A prerequisite of MBE is a high vacuum environment, essential for preventing contamination of the substrate and growing thin film by ambient gases. MBE as a film growth technique allows for layer-by-layer deposition control on the atomic level, a capability as yet unsurpassed by many other thin film growth techniques. This technique was first introduced in the 1960's for deposition of III-V semiconductors.[1,2]

The LCO films were grown in a DCA M600 MBE system[3] using elemental molecular beams of lanthanum and cobalt in the presence of a gaseous mixture of atomic and molecular oxygen (O/O_2). Some thin film samples featured in this work were grown on commercial substrates of $LaAlO_3$ (LAO) and $SrTiO_3$ (STO) while one film was deposited on a buffer layer of STO on Si(001). This buffer layer was deposited on the Si substrate using MBE growth as well.

Two effusion cells were loaded, one with a 99.9% pure lanthanum source and the other with a 99.999% pure strontium source. The effusion cells and sources were also provided by DCA Instruments. 99.95% pure cobalt metal was loaded directly into a water-cooled copper hearth, melted locally and evaporated for deposition using an ultra-high vacuum (UHV) compatible Telemark 568 linear multi-pocket electron beam source.[4]

The mixture of atomic and molecular oxygen used to oxidize the films was generated by induction heating of high-purity oxygen gas using an inductively coupled plasma (ICP) torch. An ICP torch operates on the basis of sending an alternating current (AC) of radio frequency (RF) through a metal coil that surrounds a confinement tube filled with gas. The magnetic field flux generated by the RF coil will induce a voltage that transfers energy to the gas, heating it, and thus producing a plasma.

In the case of this study, the percentage of atomic oxygen in the O/O_2 mixture was about ~10%. Atomic oxygen was produced by produced by passing 99.999% pure oxygen gas through an Oxford Applied Research HD 25 RF atom source.[5] The flow rate of the high-purity oxygen gas to the RF atom source was controlled by an Oxford Applied Research PLV1000 piezoelectric gas doser.[5]

The resultant plasma within the RF atom source is magnetically confined and the RF atom source is water cooled. Within the confinement tube a portion of the molecular oxygen is converted to atomic oxygen and/or oxygen ions. This mixture then flows into the MBE chamber via a showerhead aperture at one end of the RF atom source, which is pointed toward the substrate. An ion deflection plate near the aperture diverts the path of oxygen ions, allowing only neutral species in the oxygen beam to reach the substrate. During growth, the background pressure of the chamber increased from a base pressure

of 5×10^{-10} to about 3×10^{-5} Torr due to the introduction of this O/O_2 mixture. A fixed partial pressure of molecular oxygen is maintained in the MBE chamber after growth by turning off the plasma torch and allowing the continuous flow of O_2 while the sample cools down to room temperature. This limits the formation of oxygen vacancies in the deposited film.

Multi-component MBE film growth is accomplished by using one of two basic techniques: co-deposition or shuttered growth. In both cases, the sources, housed in effusion cells, sublimate at some characteristic temperature. The molecular beams are thus generated by heating the elemental sources until they sublimate, and the flux of the molecular beams is controlled by further adjusting the temperature of each elemental source. A quartz crystal microbalance (QCM) is typically employed to provide information about the flux of an individual source by exploiting the predictable change in resonance frequency with a change in mass of a quartz resonator. Usually, prior to deposition, the QCM is exposed to the molecular beams of each source individually and the source fluxes are calibrated. After the fluxes have been calibrated, the QCM is used in a similar fashion to determine the thickness of the film as it is being deposited. This enables control of the length of time the constituent beams are incident on the substrate surface and control of the thickness of the deposited film. Where the co-deposition and shuttered growth techniques diverge is in the way that the relative ratios of the materials deposited are controlled. During shuttered growth, molecular beams are alternated such that only one element is being deposited at any given time. Consequently, the film stoichiometry is controlled by the time a shutter controlling the flow of a molecular beam is open relative to that of the other shutters.

For co-deposition all the constituent molecular beams are deposited on the substrate surface simultaneously such that stoichiometry is determined by the ratio of the fluxes of the individual molecular beams. In this work, $LaCoO_3$ films were grown using the co-deposition technique exclusively. The current of the e-beam evaporating the cobalt source and the temperature of the lanthanum source were adjusted to yield a growth rate of LCO films roughly between 2-5 Å/min.

In situ reflection high-energy electron diffraction (RHEED) was implemented during film growth to verify the crystallinity of $LaCoO_3$ thin films in real time as they were deposited. During MBE growth of LCO thin films, 18 keV electrons were forward scattered from the sample surface at a grazing angle of ~3.0° using a STAIB RHEED gun.[6] The scattered electrons are detected on a phosphorous screen. The small grazing angle of incident electrons ensures scattered electrons will interact minimally with the bulk of the sample. As a result RHEED is very surface sensitive, to within a few monolayers of the sample surface, making it very well-suited for MBE growth.

Minimization of the interaction depth of electrons allows diffracted electrons to be treated as if they are diffracted by a 2D plane. Momentum transfer for elastically scattered electrons amounts to a reciprocal lattice vector and diffraction occurs at the intersection of the reciprocal lattice with the Ewald sphere. Thus, observing diffraction spots from the substrate surface yields information regarding the surface termination, and monitoring diffraction spots during growth provides information about the crystallinity and roughness of the thin film surface and even relaxation of the film with increasing thickness. A kSA 400 CCD camera is used for detection of the RHEED pattern in real-time prior to and during growth of LCO thin films and companion software from K-space was used for analysis.[7]

In principle, though, RHEED is also capable of measuring the growth rate, film thickness and composition. Growth rate is typically indicated by the oscillation of the intensity of diffraction spots as atomic layers are deposited. RHEED has been developed to the point where the technique is sensitive to monolayer coverage for both shuttered[8] and co-deposition[9] growth. In the case of STO, RHEED has been shown to be sensitive to stoichiometry, but prior calibration with careful analysis of the shape of the RHEED oscillation profile and interpretation of changes in the slope of the oscillation envelope during shuttered dosing was required to do this.[10] This offers another means to control stoichiometry in addition to the QCM. However, different contributions from substrate surface termination/roughness, flux calibration errors and/or instabilities in molecular beam sources, film roughening and relaxation, and non-stoichiometry of atomic layers can all produce changes that are similar to one another in the intensity and shape of RHEED oscillation profiles and diffraction spots. This can render the full complement of analytical information available from RHEED difficult to access.

2.1.1 Alternative Synthesis Methods for $LaCoO_3$

Industrial coatings for gas sensing[11, 12] and solid-oxide fuel cells[13] are produced by a number of techniques among them electrohydrodynamic deposition[14, 15], sol-gel[16], chemical vapor deposition (CVD) methods and even hybrid approaches that employ more than one technique[17, 18]. These techniques do not typically produce single crystal $LaCoO_3$ thin films, however, and all characterization of films must be performed post-deposition. They lack a means to monitor film growth *in situ*, as the films are deposited.

Sol-gel methods have been reported to produce textured, porous films with oxygen vacancy and distributions advantageous for catalytic activity.[12] Subsequent

thermal processing for these films to modify microstructure is also typically performed near or at temperature ranges where thermal decomposition[19] and interface diffusion of chemical species[20,21] can occur. Polymer-assisted deposition techniques applied to perovskite thin films more recently show promise in film and surface morphology[22] but whether or not this technique produces epitaxial $LaCoO_3$ thin films suitable for strain studies is debatable and requires further investigation.[23]

Few instances of LaCoO3 thin films grown using CVD are reported in the literature.[24,25] CVD followed by processing at higher temperatures is known to produce defects and deposition byproducts, and often impurities and vacancies are purposefully produced. For perovskite oxide materials, sensing and catalytic performance requires optimizing grain size and dopant, defect and vacancy distributions to tailor grain boundary transport and bulk grain conductivity and the valence state of chemical species.[26] Indeed for LCO grown on MgO and $LaAlO_3$ substrates using CVD, fluoride contamination and La_2O_3 phase formation is reported.[27]

Sputtered $LaCoO_3$ films[28,29,30] are also less commonly featured in the literature but lanthanum cobaltite films adequate for epitaxial strain studies have been successfully grown using sputtering techniques.[31,32,33,34] Nearly all of these sputtered films are doped, however.

Deposition of $LaCoO_3$ thin films intended for epitaxial strain studies seeking to understand effect of strain on the valence and spin state of cobalt is most often accomplished using pulsed laser deposition (PLD). PLD is an atomic layer deposition technique that uses laser ablation to produce a physical vapor of source elements, rather than sublimation of source elements for producing elemental beams as in MBE. As with MBE, RHEED can be incorporated for *in situ* growth monitoring in real time with PLD.

It bears consideration though is whether PLD can produce low defect density films. In the literature, there are numerous reports of defect formation in oxide materials deposited using PLD.[35,36,37] By no means are defects undesirable, however, and controlling defect density has been proposed as a means to obtain favorable properties in oxide materials.[38,39] Realizing ideal PLD growth of thin film oxides involves optimizing many parameters and on a material-by-material basis, including optimization of laser parameters for ablating the elemental sources.[40]

In previous work, x-ray diffractometry results for an $LaCoO_3$ thin film deposited on $SrTiO_3$ using PLD revealed cracking which the authors attributed to structural relaxation, leading them to speculate that a lattice mismatch of +2.76 % represented an upper bound of tensile strain that could be applied to LCO thin films.[41] Given that bulk, relaxed $LaCoO_3$ is non-magnetic, reports of a higher saturation magnetization for a relaxed thin film of $LaCoO_3$ deposited on a $LaAlO_3$ substrate using PLD when compared to a compressively strained film indicate defects are at play.[42]

Discussed in some detail in the chapters to follow are observations of periodic strain modulation and local vacancy ordering (hence modulation of the spin-state of Co) in strained strontium-doped $LaCoO_3$ thin films and more recent reports of similar patterns observed in strained undoped $LaCoO_3$ thin films, all grown by PLD. These reports rely on transmission electron microscopy (TEM) data. Reports of ferroelasticity in $LaCoO_3$ lead this author to suspect that the milling and mechanical processing of these samples for TEM measurements could lead to spontaneous strain formation within the film and it is not clear that these features are intrinsic to the films.

2.2 METAL FLUX SYNTHESIS

The single crystal samples UMn_2Ge_2 (UMG) measured using MFM were synthesized by reacting the constituent elements in the presence of a molten zinc flux. Samples for other studies have been grown more commonly using arc melting.[43] Metal flux synthesis of intermetallic compounds is a rather straightforward technique that provides a number of advantages to traditional solid state techniques. This technique of preparing alloys in the presence of a molten metal flux is long-established and likely to be older than the earliest reference available in the literature to this author, referring to synthesis of mercury-rich alloys of Fe, Co, Ni, Cu, Mn, Zn, and Sn using a mercury solution.[44]

Metal flux synthesis makes use of a metal with a low melting point relative to those of the reagents and in which the reagents have some solubility. Fluxes themselves can also serve as reactants, contributing to the formation of a compound. Given the high melting points of the constituent elements, a metal flux with a comparatively low-melting point reduces the reaction temperature significantly. As you can imagine, the metal flux must also have a sufficiently large difference between its melting and boiling points. In the case of UMG, zinc's melting point of 419.5°C is slightly less than half the temperature of the melting point of germanium and about a third of the melting point of uranium and manganese. Zinc's boiling point is nearly 500°C higher than its melting point.

A suitable choice of flux also facilitates greater diffusion of the reagents for single crystal growth and prevents defect formation. Generally flux reactions are performed at lower temperatures, so the reactivity of the reagents with impurities is typically less than in traditional synthesis techniques performed at higher temperatures. Most flux reactions

are also performed in an excess of flux, making it more likely for impurities to react with the flux rather than the reagent. This is especially important to promote an oxygen-free environment for molten metal reactions where the reagents are susceptible to oxidation.

For growth of ternary intermetallic compounds like UMG an advantage of metal flux synthesis is that less thermodynamically stable ternary phases for a given set of reactants can be made more accessible due to the reduction of reaction temperature and enhanced diffusion of reactants. In more traditional techniques, promotion of ternary phase formation and prevention of the formation of more thermodynamically stable binary phases is resource intensive and can require repeated steps of grinding and heating the reagents, using very long annealing steps in heating profiles, and using less-stable binary or ternary phase materials to start. Most reports of UMG samples produced by arc melting required lengthy annealing treatments over a period of days at high temperatures.

Thus, choosing a suitable flux requires a working knowledge of the phase diagrams of the flux material, reactants and reaction container materials as well as those of any stable compounds formed by combinations of the flux material, reactants and reaction container materials. In addition, the ability to separate the metal flux from the reaction products either by chemical or mechanical means is also a very important consideration.

Chapter 3: Sample Characterization Methods

This chapter discusses the background and working principles of the techniques employed to characterize the materials featured in this work. The chapter will be divided amongst global characterization techniques used, that is, X-ray diffraction and SQUID magnetometry, and local measurement using scanning probe microscopy (SPM). In the case of SPM I will quickly zoom in on the related topic of magnetic force microscopy (MFM) which is the main technique used by this author to image local magnetic domain distributions in the samples featured in this thesis. The MFM used is non-commercial; its design will be featured in a later section. But as this instrument is "home-grown" I will discuss relevant noise and resolution considerations. For the commercial X-ray diffractometer and SQUID magnetometer in-depth considerations of noise and resolution will be omitted.

3.2 GLOBAL CHARACTERIZATION TECHNIQUES

3.2.1 X-ray Diffraction

With typical wavelengths for X-rays on the order of 0.01 to 10 nm, the first observations of X-rays in the late 1800's initiated a surge of potential for research of structures with very high resolution. Wilhelm Röntgen's systematic studies of X-rays near the turn of the 20^{th} century came on the heels of great progress in crystallography due to a comprehensive theoretical description of crystal structures and symmetries that was advanced by notable contributions from Miller, Bravais, and Schönflies among others. Crystalline materials feature an ordered array of constituent atoms, ions, molecules, or even proteins that recur at regular intervals or periods. The first X-ray

scattering experiments are attributed to Max von Laue who recognized that visible light had wavelengths too long to probe the spacing of atoms in a crystal and, as a result, proposed and experimentally utilized X-ray scattering as a means to examine crystalline structure.

3.2.1.1 Principles of X-ray Diffraction in Crystalline Media

Mathematically, the periodicity of a crystal structure can be reduced to a fundamental vector basis, a unit cell, such that a set of discrete translation operations on the bases, referred to as Bravais lattice vectors, can generate the position of any element in the crystalline lattice according to:

$$\vec{\boldsymbol{s}} = c_1\vec{\boldsymbol{a}}_1 + c_2\vec{\boldsymbol{a}}_2 + c_3\vec{\boldsymbol{a}}_3 \,, \tag{3.1}$$

where $\vec{\boldsymbol{a}}_1$, $\vec{\boldsymbol{a}}_2$, and $\vec{\boldsymbol{a}}_3$ are the Bravais lattice vectors. Elastic scattering of X-rays by electrons in the crystal typically dominates the diffraction signal. So in addition to considering the periodicity of the crystalline structure we assume the local electron density, $\rho(\vec{\boldsymbol{r}})$, is also periodic in space and:

$$\rho(\vec{\boldsymbol{r}} + \vec{\boldsymbol{s}}) = \rho(\vec{\boldsymbol{r}}) \,. \tag{3.2}$$

Given that the electron density is periodic, we may expand this periodic function into a Fourier series:

$$\rho(\vec{\boldsymbol{r}}) = \sum_{G} \rho_G \, e^{i(\vec{\boldsymbol{G}} \cdot \vec{\boldsymbol{r}})} \,. \tag{3.3}$$

Thus the Fourier coefficient in the series presented in eqn. 3.3 is:

$$\rho_G = \frac{1}{V_{cell}} \int_{cell} \rho(\vec{\boldsymbol{r}}) e^{-i(\vec{\boldsymbol{G}} \cdot \vec{\boldsymbol{r}})} \, dV \,, \tag{3.4}$$

where $V_{cell}$is the volume of the unit cell. In order to preserve the translational invariance of the electron density we are lead to construct a set of reciprocal lattice bases $\vec{\boldsymbol{b}}_1$, $\vec{\boldsymbol{b}}_2$, and $\vec{\boldsymbol{b}}_3$ such that:

$$\vec{\boldsymbol{G}} = d_1\vec{\boldsymbol{b}}_1 + d_2\vec{\boldsymbol{b}}_2 + d_3\vec{\boldsymbol{b}}_3\,, \tag{3.5}$$

$$\rho(\vec{\boldsymbol{r}} + \vec{\boldsymbol{s}}) = \sum_G \rho_G\, e^{i[\vec{\boldsymbol{G}}\cdot(\vec{\boldsymbol{r}}+\vec{\boldsymbol{s}})]} = \rho(\vec{\boldsymbol{r}}) \;\rightarrow \vec{\boldsymbol{b}}_i \cdot \vec{\boldsymbol{a}}_j = 2\pi\delta_{ij}\,, \tag{3.6}$$

$$\vec{\boldsymbol{b}}_i = \frac{2\pi}{V_{cell}}\epsilon_{ijk}\left(\vec{\boldsymbol{a}}_j \times \vec{\boldsymbol{a}}_k\right). \tag{3.7}$$

These bases can be used to construct yet another Bravais lattice in that a set of discrete translation operations on the bases will produce the position of any element in the reciprocal lattice. The fundamental vector basis defining a unit cell in reciprocal space is referred to as the Brillouin zone.

In a typical x-ray diffractometer where the length scales on which the experiment is conducted are much longer than the wavelength of the X-rays themselves, we may describe X-ray radiation diffracted by a crystalline medium as a plane wave scattered by scattering centers in the crystal. This scattering results in a phase difference between the incident and scattered beam, $\exp\{i[(\vec{\boldsymbol{k}} - \vec{\boldsymbol{k}'})\cdot\vec{\boldsymbol{r}}]\}$. The scattering wavevector is defined as the change in wavevector between the incoming and outgoing wave, that is:

$$\Delta\vec{\boldsymbol{k}} = \vec{\boldsymbol{k}'} - \vec{\boldsymbol{k}}\,. \tag{3.8}$$

Given that the electrons contribute largely to scattering of X-rays, the amplitude of the scattered wave should be proportional to the integral over the volume of the crystal of the local electron density multiplied by the phase factor, thus:

$$A = \int \rho(\vec{\boldsymbol{r}})e^{-i(\Delta\vec{\boldsymbol{k}}\cdot\vec{\boldsymbol{r}})}\,dV = \sum_G \int \rho_G\, e^{i[(\vec{\boldsymbol{G}}-\Delta\vec{\boldsymbol{k}})\cdot\vec{\boldsymbol{r}}]}\,dV\,. \tag{3.9}$$

The condition that all scattered X-rays interfere constructively is met when the change in the wavevector is equal to a particular reciprocal lattice vector, that is:

$$\Delta\vec{\boldsymbol{k}} = \vec{\boldsymbol{G}}\,. \tag{3.10}$$

If you consider a linear crystal with scattering centers located at every lattice point $\vec{\boldsymbol{d}}_m = m\vec{\boldsymbol{a}}$, where m is an integer, the sum of the amplitude of scattered radiation over all M lattice points according to eqn. 3.9 would be:

$$A \propto \sum_{m=1}^{M-1} e^{-i\left(\Delta\vec{\boldsymbol{k}}\,\cdot\, m\vec{\boldsymbol{a}}\right)} = \frac{1 - e^{-iM\left(\Delta\vec{\boldsymbol{k}}\,\cdot\,\vec{\boldsymbol{a}}\right)}}{1 - e^{-i\left(\Delta\vec{\boldsymbol{k}}\,\cdot\,\vec{\boldsymbol{a}}\right)}}\,. \tag{3.11}$$

The intensity of the scattered radiation would then be proportional to the modulus of the amplitude squared and:

$$I \propto \frac{\sin^2\left[\frac{M}{2}\left(\Delta\vec{\boldsymbol{k}}\,\cdot\,\vec{\boldsymbol{a}}\right)\right]}{\sin^2\left[\frac{1}{2}\left(\Delta\vec{\boldsymbol{k}}\,\cdot\,\vec{\boldsymbol{a}}\right)\right]}\,. \tag{3.12}$$

This diffraction will be maximal when the dot product in the argument of eqn. 3.12 is an integer multiple of 2π. If we alter the dot product slightly such that:

$$\left(\Delta\vec{\boldsymbol{k}}\,\cdot\,\vec{\boldsymbol{a}}\right) = 2\pi l + \epsilon\,, \tag{3.13}$$

where l is an integer and ϵ is chosen to yield the position of the first zero in the argument $\sin\left[\frac{M}{2}\left(\Delta\vec{\boldsymbol{k}}\,\cdot\,\vec{\boldsymbol{a}}\right)\right]$ such that:

$$\sin\left[\frac{M}{2}(2\pi l + \epsilon)\right] = -\sin\left(\frac{M\epsilon}{2}\right) = 0 \;\rightarrow \epsilon = \frac{2\pi}{M}\,. \tag{3.14}$$

Thus the width of the first-order diffraction peak is inversely proportional to M, making it quite narrow for macroscopic values of M. This result holds for a three-dimensional crystal as well.

Now that we have considered the diffraction conditions resulting from the scattering of radiation from a periodic electron density within a crystal lattice, we may consider the contribution of each atom within the basis of the unit cell to the local

electron density. The scattered amplitude from a unit cell may be written as a superposition of the contributions from each atom in the basis such that:

$$S_{\vec{k}} = f_1 e^{-i(\Delta\vec{k}\cdot\vec{r}_1)} + f_2 e^{-i(\Delta\vec{k}\cdot\vec{r}_2)} + f_3 e^{-i(\Delta\vec{k}\cdot\vec{r}_3)} + \cdots = \sum_{j=1}^{n} f_j e^{-i(\vec{G}\cdot\vec{r}_j)}, \quad (3.15)$$

where f_j accounts for a difference in electron distribution per atom and is known as the atomic form factor. The atomic form factor is given by the Fourier transform of the electron charge distribution:

$$f_j = \int \rho_j(\vec{r} - \vec{r}_j) e^{-i[\vec{G}\cdot(\vec{r}-\vec{r}_j)]}\, dV. \quad (3.16)$$

3.2.2 SQUID Magnetometry

Imaging local behavior of magnetic domains in magnetic materials, global characterization of magnetic field and temperature dependent properties is essential and is frequently performed using a commercial magnetometer based on implementation of a Superconducting QUantum Interference Device or SQUID. Using SQUID magnetometry we obtain critical values of temperature and magnetic field strength around which we begin to explore local behavior via magnetic force microscopy. All samples examined in this study were measured using a Quantum Design $MPMS_2$ magnetic property measurement system[45] that operates in a temperature range of 1.9 K to 400 K and can apply magnetic fields as high as 7 T. SQUID magnetometers are among the most sensitive detectors of magnetic flux and, as a result, can detect anything that can be converted to a magnetic flux, namely current, voltage, magnetic field and susceptibility. The minimum detectable signal of the SQUID system used for this work is less than 10^{-6} emu at applied magnetic fields above 0.25 T and less than 10^{-8} emu at applied field strengths below 0.25 T. The SQUID owes its sensitivity to interference of electron wave functions across a barrier that weakly couples two superconductors. This barrier is

commonly referred to as a Josephson junction, named for the physicist who theoretically predicted tunneling between superconductors after the emergence of Ginzburg-Landau theory and BCS theory in the 1950s revolutionized our understanding of superconductivity.

In this section I will briefly describe the background, theory and principles of SQUID operation. Two main classifications of SQUIDs exist: *rf* SQUIDs and *dc* SQUIDs. An *rf* SQUID employs one junction in a superconducting ring to which a radio-frequency magnetic flux is applied. A *dc* SQUID features two junctions in parallel in a superconducting ring that is biased with a constant current. The SQUID data presented in this thesis were all obtained using a *dc* SQUID and thus I will limit my discussion of SQUIDs to *dc* SQUIDs.

3.2.2.1 An Introduction to Superconductivity

H. K. Onnes early experiments with cryogenics enabled a first look at low temperature properties of materials, resulting in the first observation of superconductivity in mercury in 1911.[46] Superconductivity describes the property of certain materials that have zero electrical resistance below some characteristic temperature, T_c. As identified by Meissner and Oschenfeld in 1933[47], superconductors are perfectly diamagnetic, that is, they have a magnetic susceptibility of -1 and expel all magnetic flux from the interior of the superconductor to maintain zero magnetic field within the material. Analogous to T_c, there is also a critical strength of an external magnetic, H_c, beyond which a superconductor will transition back to a resistive state.

The observation of superdiamagnetism in superconductors prompted the development of a number of phenomenological models. Gorter and Casimir used

thermodynamics and Maxwell's equations to construct a two-fluid model where some electrons were in a normal state and others were in a superconducting state.[48] Shortly afterward, a superconducting alloy was identified that featured both a normal and superconducting region due to partial penetration of an external magnetic field above a critical value.[49] This type of material correspondingly had an upper and lower critical value of the external magnetic field. At external magnetic fields greater than the upper limit, superconductivity is destroyed; at external fields between the lower and upper limit coexisting normal and superconducting regions can be observed within some characteristic depth. Superconductors with two critical values of external magnetic field between which the normal phase and superconducting phase can be observed to coexist are branded type-II superconductors. Superconductors with one H_c above which superconductivity is abruptly destroyed are labeled as type-I superconductors.

Within the same year the first type-II superconductor was discovered, F. and H. London successfully explained the Meissner effect as a minimization of the electromagnetic free energy carried by superconducting current. In addition they predicted that external magnetic fields could penetrate superconductors up to some characteristic depth.[50] The London penetration depth would feature prominently in Ginzburg-Landau theory in the 1950s and Fritz London would extend the theoretical treatment of superconductors in magnetic fields to predict that magnetic flux threaded through a loop of superconducting material is quantized.[51]

Ginzburg-Landau theory was closely followed by the first microscopic theory of superconductivity proposed by Bardeen, Cooper and Schrieffer in which the superconducting current is composed of a superfluid of electron pairs called Cooper pairs that are coupled via phonon exchange. Just as London extended the treatment of

conductors in external magnetic fields to a straightforward examination of superconductors in external magnetic fields, in 1962 Brian Josephson would move beyond conventional theories of single electron tunneling to explore tunneling of Cooper pairs in superconductors.[52]

A SQUID operates based on these two consequences of superconductivity, that is, flux quantization and the Josephson Effect. Both concepts will be treated in the sections to follow.

3.2.2.2 Flux Quantization

Consistent with Ginzburg-Landau theory the characteristics of a superconductor near the superconducting transition can be expressed as a function of a complex order parameter, Ψ, given by:

$$\Psi(\vec{\boldsymbol{r}}, t) = |\Psi(\vec{\boldsymbol{r}}, t)| e^{i\varphi(\vec{\boldsymbol{r}}, t)} . \tag{3.17}$$

The local density, η, of superconducting electrons can be expressed as the modulus of the order parameter squared, that is:

$$|\Psi(\vec{\boldsymbol{r}}, t)|^2 = \eta . \tag{3.18}$$

Thus the complex order parameter can be viewed as a wave function describing a condensate of coherent Cooper pairs with an amplitude and phase, φ. This parameter does not describe the probability amplitude for a single particle, but rather reflects the macroscopic ensemble of superconducting electrons.

Using eqn. 3.17 it is useful to construct something like a probability current, $\vec{\boldsymbol{j}}$, that is:

$$\vec{\boldsymbol{j}} = \frac{1}{m'} \left\{ [\Psi^*(\vec{\boldsymbol{r}}, t)\, \hat{p}\, \Psi(\vec{\boldsymbol{r}}, t) - \Psi(\vec{\boldsymbol{r}}, t)\, \hat{p}\, \Psi^*(\vec{\boldsymbol{r}}, t)] - q' \vec{\boldsymbol{A}} |\Psi(\vec{\boldsymbol{r}}, t)|^2 \right\}, \tag{3.19}$$

where $\vec{\boldsymbol{A}}$ is the vector potential of the magnetic field, m' and q' are the mass and charge of the Cooper pair, respectively, and the momentum operator, $\hat{\boldsymbol{p}}$, is:

$$\hat{p} = -i\hbar\nabla\,. \tag{3.20}$$

Substituting eqn. 3.20 into the expression for probability current, we arrive at:

$$\vec{\boldsymbol{j}} = \frac{1}{\Lambda}\left[\frac{2\hbar}{q'}\nabla\varphi(\vec{\boldsymbol{r}},t) - \vec{\boldsymbol{A}}\right], \tag{3.21}$$

where the constant Λ is defined as:

$$\Lambda \equiv \frac{m'}{q'\eta}\,. \tag{3.22}$$

Integrating eqn. 3.21 about a closed contour in the superconductor, we obtain:

$$\Lambda\left(\oint \vec{\boldsymbol{j}}\cdot d\vec{\boldsymbol{l}}\right) + \oint \vec{\boldsymbol{A}}\cdot d\vec{\boldsymbol{l}} = \frac{2\hbar}{q'}\oint \nabla\varphi(\vec{\boldsymbol{r}},t)\cdot d\vec{\boldsymbol{l}}\,. \tag{3.23}$$

Ultimately we expect that the probability current within a superconductor should vanish leaving us to tackle:

$$\Lambda\oint \vec{\boldsymbol{A}}\cdot d\vec{\boldsymbol{l}} = \frac{2\hbar}{q'}\oint \nabla\varphi(\vec{\boldsymbol{r}},t)\cdot d\vec{\boldsymbol{l}}\,. \tag{3.24}$$

We know from Gauss' law and Stoke's Theorem that:

$$\oint \vec{\boldsymbol{A}}\cdot d\vec{\boldsymbol{l}} = \int_S (\nabla\times\vec{\boldsymbol{A}})\cdot d\vec{\boldsymbol{s}} = \int_S \vec{\boldsymbol{B}}\cdot d\vec{\boldsymbol{s}} = \Phi_S\,, \tag{3.25}$$

where Φ_S is the magnetic flux through the surface, S, defined by the closed contour. Consider now the phase term on right hand side of eqn. 3.24. The phase variation cannot be discontinuous because the wave function must be single-valued at any point in the superconductor. If the superconducting object is simply connected all closed contours can be reduced to a path with no length, a point, and thus the magnetic flux must be zero as in the Meissner effect. If the superconducting object is annular, when a complete turn of the annulus is reached, the phase must return to the same value and:

$$\oint \nabla\varphi(\vec{\boldsymbol{r}},t)\cdot d\vec{\boldsymbol{l}} = 2\pi N\,, \tag{3.26}$$

where N is the number of turns.

Therefore, the total magnetic flux through a superconducting loop must be quantized, that is:

$$\Phi_S = \frac{2\hbar}{q'} 2\pi N = N \frac{\hbar}{2e} = \frac{N}{2\pi} \Phi_0 \,, \tag{3.27}$$

where $\Phi_0 \equiv \frac{h}{2e}$, is the magnetic flux quantum.

3.2.2.3 The Josephson Effect

Let's now consider a basic tunneling structure with a barrier between two superconducting regions. The following treatment of Cooper pair tunneling that I outline here was originally used by Feynman[53] to describe Josephson phenomena and is a very simple but key derivation. Cooper pairs in each region have their respective wave functions Ψ_a and Ψ_b; and correspondingly each region has their respective Cooper pair densities η_a and η_b. If we now take weak coupling into account, the state wave function of this two-state system, Ψ, is:

$$\Psi = \Psi_a + \Psi_b \,. \tag{3.28}$$

The time dependence of the system is given by the Schrödinger equation:

$$i\hbar \frac{\partial \Psi}{\partial t} = \hat{H}\Psi \,, \tag{3.29}$$

where the Hamiltonian operator, $\hat{H}$:

$$\hat{H} = \hat{H}_a + \hat{H}_b + \hat{H}_T \,, \tag{3.30}$$

contains the Hamiltonians for the unperturbed states and a tunneling Hamiltonian as an interaction term between the two states. The tunneling Hamiltonian can be expressed as:

$$\hat{H}_T = \kappa(\Psi_a {\Psi^*}_b + \Psi_b {\Psi^*}_a) \,, \tag{3.31}$$

where the coupling constant, κ, measures the interaction strength between the two superconducting regions. Thus:

$$i\hbar \frac{\partial \Psi_a}{\partial t} = E_a \Psi_a + \kappa \Psi_b \,, \tag{3.32}$$

$$i\hbar\frac{\partial\Psi_b}{\partial t} = E_b\Psi_b + \kappa\Psi_a\,, \tag{3.33}$$

where E_a and E_b are the ground state energies of the two superconductors. If a *dc* voltage is chosen to lie between the Fermi levels of each region such that $E_a - E_b = 2eV$ and eqn.'s 3.32 and 3.33 become:

$$i\hbar\frac{\partial\Psi_a}{\partial t} = -eV\Psi_a + \kappa\Psi_b\,, \tag{3.34}$$

$$i\hbar\frac{\partial\Psi_b}{\partial t} = eV\Psi_b + \kappa\Psi_a\,. \tag{3.35}$$

An important step in solving the time-dependent Schrödinger equations of the system is expressing the wave functions Ψ_a and Ψ_b in a form consistent with eqn.'s 3.17 and 3.18 and defining a phase difference, φ, such that:

$$\Psi_a = \sqrt{\eta_a}e^{i\varphi_a}, \Psi_b = \sqrt{\eta_b}e^{i\varphi_b}, \varphi \equiv \varphi_b - \varphi_a\,, \tag{3.36}$$

which yields:

$$\frac{i\hbar}{2\eta_a}\frac{\partial\eta_a}{\partial t} - \hbar\frac{\partial\varphi_a}{\partial t} = -eV + \kappa\sqrt{\frac{\eta_b}{\eta_a}}e^{i\varphi}\,, \tag{3.37}$$

$$\frac{i\hbar}{2\eta_b}\frac{\partial\eta_b}{\partial t} - \hbar\frac{\partial\varphi_b}{\partial t} = eV + \kappa\sqrt{\frac{\eta_a}{\eta_b}}e^{-i\varphi}\,. \tag{3.38}$$

Using Euler's formula and separating real and imaginary terms we obtain:

$$\frac{\partial\eta_a}{\partial t} = \frac{2\kappa}{\hbar}\sqrt{\eta_a\eta_b}\sin\varphi\,, \tag{3.39}$$

$$\frac{\partial\eta_b}{\partial t} = -\frac{2\kappa}{\hbar}\sqrt{\eta_a\eta_b}\sin\varphi\,, \tag{3.40}$$

$$\frac{\partial\varphi_a}{\partial t} = \frac{\kappa}{\hbar}\sqrt{\frac{\eta_b}{\eta_a}}\cos\varphi - \frac{eV}{\hbar}\,, \tag{3.41}$$

$$\frac{\partial\varphi_b}{\partial t} = \frac{\kappa}{\hbar}\sqrt{\frac{\eta_a}{\eta_b}}\cos\varphi + \frac{eV}{\hbar}\,. \tag{3.42}$$

We immediately see that time rate of change in the pair density in one superconducting region is opposite to the other as one would expect and it follows that:

$$\frac{\partial \varphi}{\partial t} = \frac{2eV}{\hbar} = \frac{2\pi}{\Phi_0} V \,. \tag{3.43}$$

This indicates that the form of the time dependence of the phase difference is linear, scaled by the voltage, that is:

$$\varphi = \varphi_0 + \frac{2\pi}{\Phi_0} Vt \,. \tag{3.44}$$

We can also define a pair density current, J:

$$J \equiv \frac{\partial \eta_a}{\partial t} = -\frac{\partial \eta_b}{\partial t} = \frac{2\kappa}{\hbar} \sqrt{\eta_a \eta_b} \sin \varphi \,. \tag{3.45}$$

If we assume $\eta_a = \eta_b = \rho$, where ρ is a constant, eqn. 3.45 reduces to:

$$J = J_0 \sin \varphi = J_0 \sin(\varphi_0 + \frac{2\pi}{\Phi_0} Vt), \tag{3.46}$$

$$J_0 \equiv \frac{2\kappa}{\hbar \rho} . \tag{3.47}$$

Eqn.'s 3.43 and 3.46 constitute the Josephson effect and from eqn. 3.46 it is clear there is a current across the junction at zero voltage. In the absence of an external field, the occurrence of a direct current proportional to the sine of the phase difference across the tunneling barrier is dubbed as the *dc* Josephson effect. Eqn. 3.47 defines the critical density current of a Josephson junction beyond which a finite voltage develops across the junction and the *V-I* characteristics revert to ohmic behavior. The voltage at which the resistance changes is related to the superconducting energy gap of the superconductor, Δ, that is the *V-I* characteristics become ohmic at $V > \frac{2\Delta}{e}$. Exemplary *I-V* characteristics for a Josephson junction illustrating the *dc* Josephson effect are presented in fig. 3.1.[54] Upon application of a non-zero voltage *dc* voltage, an alternating current with frequency $\omega = \frac{2eV}{\hbar}$ develops. This is called the *ac* Josephson effect.

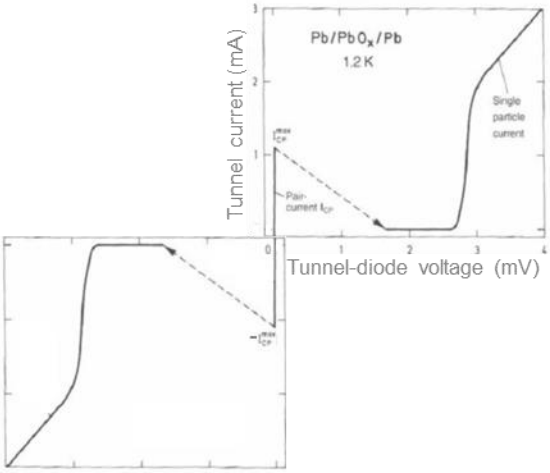

Figure 3.1 *dc* Josephson effect measured for a $Pb/PbO_x/Pb$ tunneling junction adapted from ref. [54].

3.2.2.4 Operation of dc SQUIDs

Soon after Josephson published his seminal theoretical work on tunneling in superconductors, the first Josephson junction was constructed by John Rowell and Phillip Anderson at Bell Labs.[55] Consider a simple schematic of *dc* SQUID shown in fig. 3.2 consistent with ref. [55] that features a superconducting ring broken by two Josephson junctions. When you turn on a magnetic field with the magnetic flux threaded through the loop , the integral of the phase around the loop reduces to the phase differences across the junctions that is:

$$\frac{2e}{\hbar}\oint \vec{\boldsymbol{A}}\cdot d\vec{\boldsymbol{l}} = \frac{2\pi\Phi}{\Phi_0}, \tag{3.48}$$

$$\oint \nabla\varphi(\vec{\boldsymbol{r}},t)\cdot d\vec{\boldsymbol{l}} = \varphi_L - \varphi_R = 2\pi N\,, \tag{3.49}$$

analogous to eqn.'s 3.24 and 3.26, where $\varphi_L$and φ_R represent the phase differences across the left junction and the right junction, respectively. The total current through the parallel junctions is:

$$I = I_L + I_R = (I_0)_L \sin\left(\varphi_R + \frac{2\pi\Phi}{\Phi_0}\right) + (I_0)_R \sin(\varphi_R)\,. \tag{3.50}$$

If the critical currents for both junctions are identical, eqn. 3.50 simplifies to:

$$I(\Phi) = 2I_0 \cos\left|\frac{\pi\Phi}{\Phi_0}\right|. \tag{3.51}$$

Additionally, the form of the phase difference across each junction changes and eqn. 3.46 is modified such that:

$$J = J_0 \sin\varphi = J_0 \sin(\varphi_0 + \frac{2e}{\hbar} Hdw) = J_0 \sin(\varphi_0 + 2\pi\frac{\Phi_j}{\Phi_0})\,, \tag{3.52}$$

where $d = \lambda_a + \lambda_b + \tau$ is the sum of the penetration depths of each superconductor and the thickness, τ, of the tunneling barrier, w is the width of the junction, and H is the magnetic field. The product dw defines an effective surface through which the magnetic field penetrates and thus Hdw represents the magnetic flux through the junction.

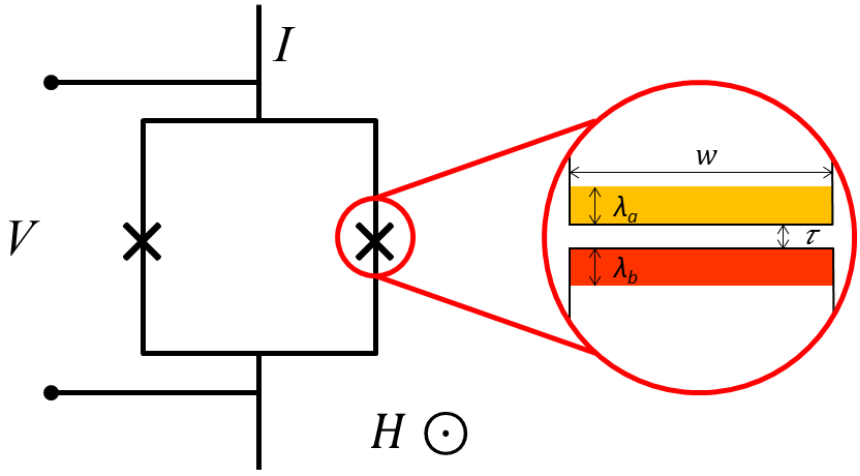

Figure 3.2 Schematic of a *dc* SQUID with a magnified view of one Josephson junction in the superconducting loop.

Thus the dependence of the current through the junction on the magnetic flux threaded through the junction has the form:

$$I(\Phi_j) = I_0 \left| \frac{\sin \pi \frac{\Phi_j}{\Phi_0}}{\pi \frac{\Phi_j}{\Phi_0}} \right| , \tag{3.53}$$

where $\Phi_j = Hdw$ is the magnetic flux through the junction.

The dependence of the total current through the loop on applied magnetic field is analogous to the convolution of interference from an aperture with the dimensions of the loop with the interference from two slits of some finite width, illustrated by fig. 3.3 obtained from ref. [56].

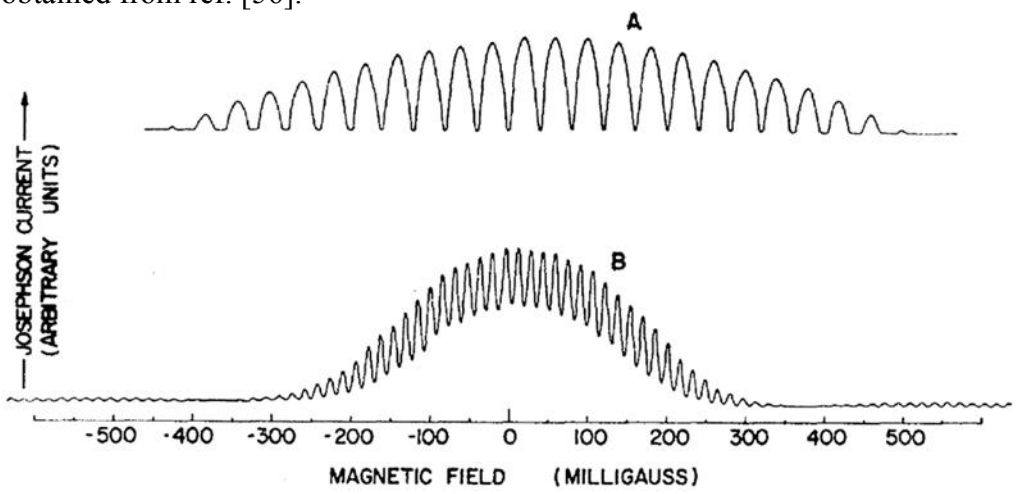

Figure 3.3 Experimental trace of I_{max} versus magnetic field showing interference and diffraction effects from ref. [56].

3.3 LOCAL CHARACTERIZATION TECHNIQUE

3.3.1 Scanning Probe Microscopy

The invention of the scanning tunneling microscope (STM) in 1981[57,58] and the subsequent invention of the atomic force microscope (AFM) in 1986[59] led to the inception of a branch of microscopy known broadly as scanning probe microscopy (SPM).

STM measures tunneling current between a very sharp, electrically conductive tip held about an atom's diameter from a metallic sample that is biased with a voltage. Depending on the sign and magnitude of the bias voltage, the direction of the tunneling current can be varied and electrons in the tip or the sample can be probed, and the exponential decay of atomic wavefunctions into the tunnel barrier renders the tunneling current extremely sensitive to distance. As a result, atomic resolution of surfaces was attainable using STM soon after its launch.[60] AFM, invented to image surfaces of insulating materials as well as conducting materials, generates surface images by scanning a sharp probe attached to a cantilever over a surface where forces between the tip of the cantilever and the sample are used to control the vertical distance. AFM, originally projected to reach atomic resolution, eventually achieved that benchmark though not right away.[61] SPM developed afterwards as the concept of a tunneling probe was generalized to any generic probe where the interaction volume can be reduced so that local interactions can be utilized to measure surface properties.

Consequently, SPM is a very diverse field that includes all techniques that use various local interactions between a physical probe and sample surface to obtain topographic surface profiles and probe other physical properties of surfaces. The

necessary components for a generalized SPM setup are illustrated in Fig. 3.4. An SPM utilizes a probe that responds monotonically to small distance changes in a measurable way. A sensor detects this response and converts it to an electronic signal that is amplified and fed into control electronics. The control electronics are interfaced to a user via a computer that employs software to process the surface profile data, converting it into a 3-D image of the sample surface and adjusting the probe-sample separation to maintain feedback parameters input by the user. Piezoelectric actuators provide coarse and fine control of the probe-sample separation as well as lateral motion and positioning of the probe or sample, including the raster motion required for scanning.

Beyond atomically resolved surfaces, SPM techniques have been developed to resolve single electron charges and nuclear spins as in a single-electron transistor scanning electrometer (SETSE)[62] and microscopy force detection of magnetic resonance of nuclear spins in nuclear magnetic resonance force microscopy (NMRFM)[63]. More recent developments include measuring the magnetic penetration depth in superconductors by obtaining Meissner response curves using magnetic force microscopy (MFM).[64,65]

The Nobel Prize awarded to the inventors of the STM in 1986 reflects the countless avenues of research which surface imaging in real space on the atomic scale opened up to the scientific community.

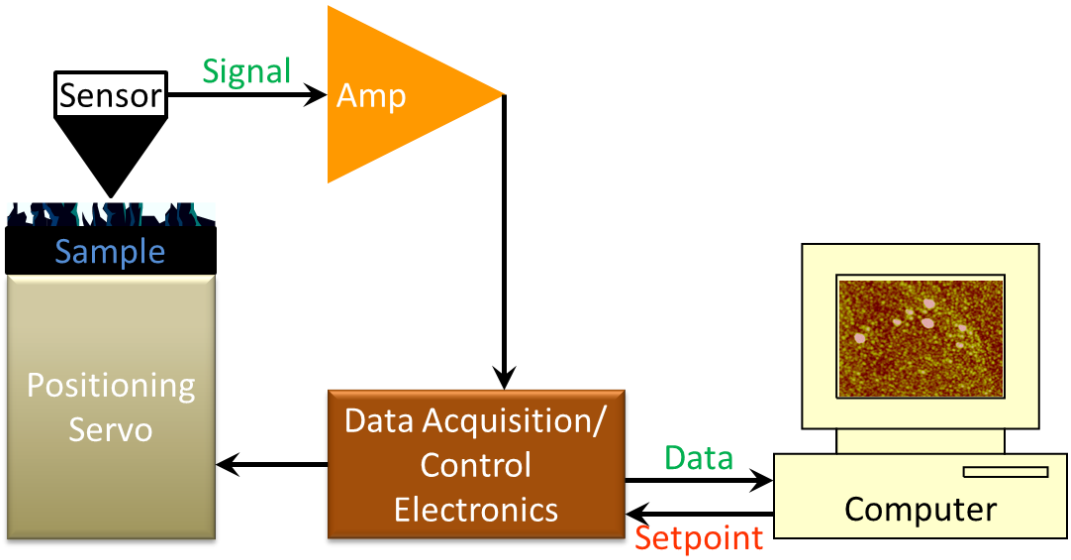

Figure 3.4 Block diagram representation of a basic scanning probe microscopy setup.

3.3.1.1 Basic Principles of Atomic Force Microscopy

It is necessary to consider the working principles of atomic force microscopy before we enlarge our scope to include magnetic interactions between a magnetic probe and sample as in magnetic force microscopy. The basic AFM probe features a sharp tip suspended on the end of a cantilever. As the probe is scanned over a sample surface of interest, the deflection of the cantilever is recorded as a function of the (x, y) position, yielding a raster image composed of the deflection signal at each pixel. The cantilever is treated as a spring and its deflection is converted into a force using Hooke's law. In standard applications, commercially available cantilevers with sharp tips are patterned from silicon and have spring constants ranging from about 0.01 N/m to 50 N/m.

In the static mode of AFM operation the deflection of the cantilever according to Hooke's law is linearly proportional to the force, F, exerted on the tip by the sample. That is:

$$\Delta z = \frac{F_z}{k}, \tag{3.54}$$

where k is the cantilever spring constant in the z-direction. As the tip will be brought into contact with the sample surface in this mode of operation, soft cantilevers are typically employed to minimize damage to the tip and sample. Issues with this mode of imaging become immediately apparent. So long as the force gradient is smaller than the spring constant of the cantilever, the cantilever will be deflected towards the sample surface due to attractive forces between the tip and sample. At the point the force gradient becomes higher than the spring constant of the cantilever, the tip position is not stable and it jumps to contact.[66] This jump-to-contact makes it impossible to image the attractive force regime at small distances from the surface prior to contact and also prohibits true atomic resolution. In addition, while the tip and sample are in contact lateral forces due to friction can flex the cantilever during raster scanning. In fact, this effect has been exploited for detection of local variation of frictional forces of surfaces.[67]

More commonly, dynamic modes of AFM measurement are employed where cantilevers are either mechanically or electrostatically driven and the change in their oscillation amplitude and/or frequency due to interaction forces between tip and sample are measured and analyzed.

Dynamic modes of AFM operation can be grouped into two categories- tapping mode or intermittent contact mode and non-contact mode. With intermittent contact the cantilever is driven at or near its resonance frequency with large amplitude typically on the order of hundreds of nanometers. In this mode of AFM operation, the oscillation

amplitude serves as the main feedback parameter where the feedback loop is set to maintain constant oscillation amplitude during approach and scanning. The amplitude set point can be chosen such that contact interactions are minimally destructive to tip and sample. Once the oscillation amplitude has been decreased due to contact forces between tip and sample and contact has been established, contact between tip and sample lasts only briefly during a portion of the cantilever's swing and for this reason intermittent contact mode is also referred to as tapping mode. Cantilevers with stiffness on the order of one to tens of N/m are typically used for intermittent contact versus the cantilevers used for contact mode with spring constants less than 10 N/m and even as little as tenths of N/m.

The non-contact mode of AFM operation necessarily tracks the oscillation of an AFM cantilever where the tip is not in contact with the sample surface. This mode is often (but not always) frequency modulated, that is, the feedback loop system adjusts the tip-to-sample distance to maintain a constant oscillation frequency. This mode operates in a weaker attractive force regime but can be operated very near to the contact regime through the use of stiff cantilevers necessarily to avoid jump-to-contact. Typical oscillation amplitudes for non-contact modes are on the order of tens of nanometers but very stiff cantilevers ($k \sim 10^4$ N/m) with sub-nm oscillation amplitude driven very close to the sample surface under ultra-high vacuum conditions can provide atomic resolution of surfaces.[68]

In this case the motion of the cantilever can be treated as that of a damped harmonic oscillator driven by an external force that is sinusoidal in time with frequency, ω. Assuming that the driving force produces a cantilever deflection in the z-direction, the equation of motion of the cantilever is:

$$\ddot{z}(t) + D\dot{z}(t) + {\omega_0}^2 z(t) = F(t)\,, \tag{3.55}$$

$$F(t) = F_0 \cos(\omega t) = Re\left[F_0 e^{-i\omega t}\right], \tag{3.56}$$

where D is a damping factor and $\omega_0 = \sqrt{k/m}$ is the resonant frequency of the cantilever.

Given a driving force that is sinusoidal in time, the deflection of the cantilever is sinusoidal in time and depends on the frequency of oscillation of the driving force as well as the phase difference between the drive oscillation and the oscillatory response of the cantilever. We seek to arrive at an ansatz whose real part satisfies eqn. 3.55 above and with some foresight choose:

$$z(t) = z_0 e^{-i(\omega t+\varphi)} = \mathbb{Z}_0 e^{-i\omega t}\,, \tag{3.57}$$

where the real amplitude, z_0, and phase information is included in the complex amplitude $\mathbb{Z}_0$. Employing this ansatz we arrive at the following expressions:

$$\frac{\mathbb{Z}_0}{F_0} = \frac{1/m}{{\omega_0}^2 - 2i\gamma\omega_0\omega - \omega^2}\,, \tag{3.58}$$

$$|\mathbb{Z}_0| = \sqrt{|\mathbb{Z}_0|^2} = \frac{\frac{F_0}{m}}{\sqrt{({\omega_0}^2 - \omega^2)^2 + 4\gamma^2{\omega_0}^2\omega^2}}\,, \tag{3.59}$$

$$\varphi = \tan^{-1}\left(\frac{2\gamma\omega_0\omega}{{\omega_0}^2 - \omega^2}\right), \tag{3.60}$$

$$\gamma \equiv \frac{D}{2}\frac{1}{\sqrt{km}}. \tag{3.61}$$

Eqn. 3.58 has poles at:

$$s_\pm = -\gamma\omega_0 \pm i\omega_0\sqrt{1-\gamma^2} = -\gamma\omega_0 \pm i\omega_D\,. \tag{3.62}$$

where ω_D is considered the damped natural frequency.

It is useful here to introduce the quality factor. For dynamic mode AFM, cantilevers with very small damping are used ($\gamma \ll 0.01$) which allows us to consider the damped natural frequency to be very near to the resonant frequency of the cantilever. The quality factor, Q, of the cantilever reflects the ratio of the energy stored in the cantilever spring to the energy lost in a given oscillation cycle:

$$Q = 2\pi \frac{{}^{1}\!/_{2}\, k{z_0}^2}{\pi D {z_0}^2 \omega_0} = \frac{k}{D\omega_0} = \frac{1}{2\gamma}. \tag{3.63}$$

Thus, eqn.'s 3.58, 3.59, and 3.60 become:

$$\frac{\mathrm{Z}_0}{F_0} = \frac{{}^{1}\!/_{m}}{{\omega_0}^2 - {}^{i\omega_0\omega}\!/_{Q} - \omega^2}, \tag{3.64}$$

$$|\mathrm{Z}_0| = \sqrt{|\mathrm{Z}_0|^2} = \frac{\frac{F_0}{m}}{\sqrt{({\omega_0}^2 - \omega^2)^2 + \left({}^{\omega_0\omega}\!/_{Q}\right)^2}}, \tag{3.65}$$

$$\varphi = \tan^{-1}\left[\frac{\omega_0\omega}{Q({\omega_0}^2 - \omega^2)}\right]. \tag{3.66}$$

As the AFM probe approaches the surface, the forces of interaction between the tip and sample act as a force in parallel to the driving force, shifting the resonant frequency:

$$\omega_0' = \omega_0 \sqrt{1 - \frac{1}{k}\frac{\partial F}{\partial z}}. \tag{3.67}$$

If we assume the positive z-direction points away from the sample surface, an attractive force produces a positive force derivative that reduces the resonant frequency of the cantilever, effectively softening it. Frequency shift values due to long-range magnetic forces acting on a magnetic force microscopy probe presented later in this thesis are on the order of tenths to tens of Hertz, smaller than the bandwidth of frequency

measurement (~10^2 Hz.) and much smaller than the typical width of the resonance peak (~10^3 Hz.).

3.3.1.2 Basic Principles of Magnetic Force Microscopy

The utility of an AFM setup is that it can be readily modified to accommodate imaging of local magnetic properties using MFM. MFM is realizable by coating an AFM tip with magnetic material where interaction forces between the tip and sample include not just mechanical forces but also those which arise from the interactions between the stray magnetic field, $\vec{B}(\vec{r})$, at the sample surface and the magnetic moment of the tip, $\vec{m}_{tip}(\vec{r})$. We can obtain the expression for the force due to magnetic interactions between the tip and sample from the expression of the potential energy. We integrate over the interaction volume of the tip, summing up all the contributions of each dipole moment on the tip in the presence of the stray magnetic field from the sample, and arrive at the following expression for the potential energy:

$$U = -\int_{tip} \vec{m}_{tip}(\vec{r}) \cdot \vec{B}(\vec{r})\, d\vec{r}\,. \tag{3.68}$$

Assuming that the magnetization is constant in the tip, the expression for interaction force due to magnetic interactions:

$$F = -\nabla U = \int_{tip} \vec{m}_{tip}(\vec{r}) \cdot \nabla \vec{B}(\vec{r})\, d\vec{r}\,. \tag{3.69}$$

If we assert that tip motion is constrained to the z-direction, we expect the magnetic flux density to vary only in the z direction, and we can discard x and y contributions to magnetic field gradient in eqn. 3.69. In reality we do expect variation in the magnetic flux density in x and y to contribute, though negligibly. Furthermore, if we invoke the point-

dipole approximation[69], treating the magnetic moment of the tip as a point-dipole pointing entirely in the z-direction, then we obtain:

$$F = m_z \frac{\partial B(z)}{\partial z}. \tag{3.70}$$

However, if one were to attempt measuring the static deflection of a cantilever due to the force gradient of a magnetic field at some tip-sample separation, this measurement would be limited by 1/*f* noise. Rather than attempting to measure the force due to the local magnetic field this way, we apply a driving force to mechanically oscillate the cantilever and measure frequency shift due to magnetic interactions between the tip and sample as in dynamic mode AFM.

The gradient of the magnetic force due to stray magnetic fields in the sample cause a shift in the resonant frequency of the cantilever consistent with eqn. 3.70, where:

$$\frac{\partial F}{\partial z} = m_z \frac{\partial^2 B(z)}{\partial z^2}. \tag{3.71}$$

Provided that the force gradient is small compared to the spring constant of the cantilever, the shift in the resonant frequency of the cantilever can approximated to be:

$$\Delta f = f_0' - f_0 \approx -\frac{f_0}{2k}\frac{\partial F}{\partial z}, \tag{3.72}$$

and a phase shift results according to:

$$\Delta\varphi = -\frac{Q}{k}\frac{\partial F}{\partial z}. \tag{3.73}$$

For imaging in MFM, the driving frequency or the phase difference between the drive frequency and cantilever response is set and magnetic interactions can be imaged by recording the local shift in frequency or phase. Magnetic forces between tip and sample dominate for tip-sample separations in the range of roughly 50-100 nm. Thus, frequency shift images of local magnetic interactions are obtained during "lift mode" where the topographic profile is obtained in one scan line and then the surface is retraced at a fixed tip-sample separation and the frequency shift at each pixel is measured.

3.3.1.3 Resolution and Noise Considerations

The ultimate limit on force sensitivity of an AFM cantilever is set by thermal vibrations of the cantilever. From the equipartition theorem, thermal fluctuations at temperature T have an energy which we can equate to the energy of the thermal fluctuations in the amplitude of oscillation of cantilever such that:

$$E_T = \frac{1}{2}k_B T = \frac{1}{2}k\langle z_{th}^2 \rangle . \tag{3.74}$$

It will be useful to recognize that eqn. 3.74 represents the cantilever response function in frequency so that we may define:

$$G(\omega) \equiv \frac{|\mathrm{Z}_0|}{F_0} = \frac{{}^{1}/_{m}}{\sqrt{({\omega_0}^2 - \omega^2)^2 + \left({}^{\omega_0 \omega}/_{Q}\right)^2}}, \tag{3.75}$$

and consider that:

$$z_{th} = G(\omega)F_{th}(\omega) , \tag{3.76}$$

where $F_{th}(\omega)$ is the thermal drive. We assume that the thermal drive is equally distributed over all frequencies, or that thermal noise is white ($F_{th}(\omega) = F_{th}$). We, at least, assume this for the range of frequencies relevant to cantilever operation. We can calculate the mean square of the thermal fluctuation amplitude as in the right hand side of eqn. 3.74:

$$\langle z_{th}^2 \rangle = \int_{-\infty}^{\infty} G^2(\omega)F_{th}^2 \, d\omega = \frac{\pi Q \omega_0}{k^2}F_{th}^2 = \frac{k_B T}{k} \rightarrow F_{th} = \sqrt{\frac{k \, k_B T}{\pi Q \omega_0}}. \tag{3.77}$$

As the thermal noise source decreases with increasing Q, using high-Q cantilevers is expected to greatly reduce the thermal noise away from resonance. Therefore, we might confine our perspective to the thermal noise produced at frequencies within the side bands of the oscillator:

$$\langle F_{th}^2 \rangle = \int_{-\Delta\omega}^{\Delta\omega} F_{th}^2 \, d\omega = \frac{4\, k\, k_B T B}{\pi Q \omega_0}, \tag{3.78}$$

where $B = \frac{\Delta\omega}{2\pi}$ is the bandwidth. This result is consistent with Albrecht et al.[70] where the minimum detectable force gradient was determined to be:

$$\delta F'_{min} = \sqrt{\frac{4\, k\, k_B T B}{\omega_0 Q \langle z_{osc}^2 \rangle}}, \tag{3.79}$$

where $\langle z_{osc}^2 \rangle$ is the mean square amplitude of the self-oscillation of the cantilever.

In addition to fundamental limitations in force sensitivity due to fluctuations in the cantilever deflection, we are limited by noise in the sensor used to detect the cantilever's deflection. We employ a fiber-optic Fabry-Perot interferometer as our detector. This interferometer is constructed by coupling a single-mode commercial laser source to the primary input of a fiber optic coupler that splits the laser light amongst a primary output which serves as a reference and a secondary output that is connected to an optical fiber whose cleaved end is positioned above the back of the cantilever. The light reflected by the back of the cantilever reenters the fiber and interferes with the back-reflected light from the glass-air interface. This interference is exploited to measure cantilever deflection. The instrumentation and principles of operation of the interferometer will be discussed in more detail in chapter 4.

The power of reflected light, P_r, generated between two identical reflective plates with some characteristic reflectivity, $\mathcal{R}$, separated by some distance, z, is given to be[71]:

$$P_r = P_0 \frac{F \sin^2 \frac{\delta}{2}}{1 + F \sin^2 \frac{\delta}{2}}, \tag{3.80}$$

$$F \equiv \frac{4\mathcal{R}}{(1-\mathcal{R})^2}, \tag{3.81}$$

$$\delta = \frac{4\pi n z}{\lambda_0}, \tag{3.82}$$

where P_0, n, and λ_0 are the power of the incident light, the index of refraction of the medium between the reflective plates and the wavelength of the light source in vacuum, respectively. In the case of our setup where the reflectivities of the surfaces in the interference cavity are different, we can generally conclude that the reflected power is a function of the reflectivities and separation distance between the fiber and cantilever such that:

$$P_r = P_0 \times f\left(\mathcal{R}_{glass}, \mathcal{R}_c, z\right), \tag{3.83}$$

where $\mathcal{R}_{glass}$ and $\mathcal{R}_c$ are the reflectivities of the cleaved end of the fiber and the cantilever, respectively. The current, i, at the photodiode produced by the reflected light is thus:

$$i = \eta P_r, \tag{3.84}$$

where η is the responsivity of the photodiode. The associated spectral shot noise density at a given frequency is:

$$\Omega_{shot}(\omega) = \sqrt{2e\eta P_r}. \tag{3.85}$$

The associated current and voltage noise over the bandwidth of the measurement is simply:

$$\langle i_{shot}^2 \rangle = \int_{-\Delta\omega}^{\Delta\omega} \Omega^2(\omega)\, d\omega = 2e\eta P_r B, \tag{3.86}$$

$$\langle V_{shot}^2 \rangle = 2e\eta P_r B R^2, \tag{3.87}$$

where R is a resistive load. If the sensitivity of the diode, S, is:

$$S = \frac{\Delta V}{\Delta z} = \eta R \frac{dP_r}{dz} = \eta R P_0 \frac{df}{dz}. \tag{3.88}$$

The minimum detectable change in the fiber and cantilever separation is:

$$\delta z_{min} = \frac{\sqrt{\langle V_{shot}^2 \rangle}}{S} = \sqrt{\frac{2eB}{\eta P_0} \times f\left(\mathcal{R}_{glass}, \mathcal{R}_c, z\right)} \times \left(\frac{df}{dz}\right)^{-1}. \tag{3.89}$$

Eqn. 3.89 indicates that photodiode shot noise depends on the make-up of the interference cavity and the inverse root of the incident power.

The resistive load on the photodiode at some temperature is subject to Johnson-Nyquist noise with a spectral noise density:

$$\Omega_J(\omega) = \sqrt{4k_B TR}. \tag{3.90}$$

Thus, the associated current and voltage noise over the bandwidth of the measurement is:

$$\langle V_J^2 \rangle = \int_{-\Delta\omega}^{\Delta\omega} \Omega_J^2(\omega)\, d\omega = 4k_B TRB\,, \tag{3.91}$$

$$\langle i_J^2 \rangle = \frac{4k_B TB}{R}. \tag{3.92}$$

For the laser source employed in our interferometer, it is important to consider at least briefly the functional forms of noise in the laser output. For a single-mode laser there is intensity noise and phase noise. Intensity noise is a product of mode-partition noise, mode-hopping noise, 1/*f* noise and spontaneous emission. There are complicated theories that seek to arrive at a functional form of the laser intensity noise which properly accounts for all these contributions, but for practical purposes we may utilize the following expression from ref. [72] which represents the intensity noise of a typical laser diode:

$$i_{intensity}^2 = \eta^2 P_0^2 \times 10^{-13} \left[V^2/_{Hz}\right], \tag{3.93}$$

$$V_{intensity}^2 = \eta^2 P_0^2 R^2 \times 10^{-13} \left[V^2/_{Hz}\right]. \tag{3.94}$$

Phase noise results from the finite coherence length of a laser and depends on the optical path length along which the light travels. Phase noise causes a finite laser

linewidth, limits temporal coherence and is strongly related to frequency noise. According to ref. [73], the laser phase noise has the form:

$$\langle i_{phase}^2 \rangle = \eta^2 P_0^2 4\pi \Delta\nu B\tau \,, \tag{3.95}$$

$$\langle V_{phase}^2 \rangle = \eta^2 P_0^2 R^2 4\pi \Delta\nu B\tau \,, \tag{3.96}$$

where $\Delta\nu$ and τ are linewidth of the laser and the optical path length difference, respectively. Given that the noise sources are independent of one another and uncorrelated, the noise contribution due to thermal cantilever motion, shot noise, laser intensity noise, and laser phase noise may be calculated by taking the square root of the sum of the mean-squared values of the individual noise terms (see fig. 3.5). The total noise contribution can be obtained by scaling the root sum of the mean-squared values of these noise terms according to the current-to-voltage gain curve of the system and then accounting for Johnson noise at the output.

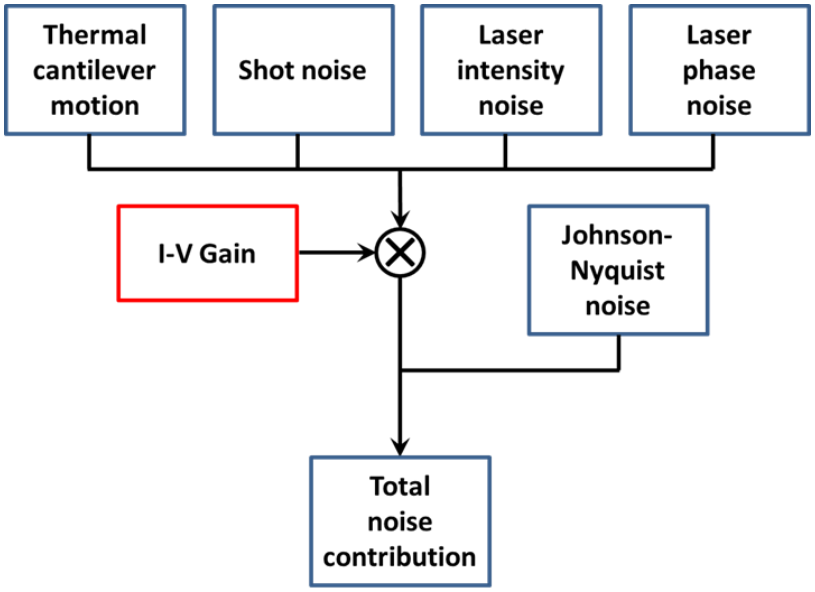

Figure 3.5 Block diagram representation of the addition of noise contributions due to thermal vibrations of the cantilever, laser diode and photodetector noise, and Johnson-Nyquist noise.

Chapter 4: Multi-mode Atomic Force Microscope

This chapter is devoted to detailing the various design aspects and capabilities of the multi-mode variable-temperature atomic force microscope (VT-AFM) designed previously by Tien-Ming Chuang and implemented in this study to carry out local MFM measurements on $LaCoO_3$ and UMn_2Ge_2.[74] This design accommodates operation in a high-vacuum environment at cryogenic temperatures and in applied magnetic fields on the order of Teslas. It implements a number of home-built parts and electronics.

Essentially, we mechanically drive commercial cantilevers at or near their resonance frequency and use a fiber-optic interferometer to sense the amplitude of cantilever deflection. A commercial photodetector converts the interference signal to a voltage and amplifies it. Amplitude-modulated feedback for approaching and scanning is controlled by a NanoScope™ IIIa controller with an Extender™ Module and control software. Coarse approach where the sample "walks" into contact with the AFM probe results from stick-slip motion provided by legs coupled mechanically to piezo actuators. Walking is manually controlled by firing a sequence of voltage pulses to the walking piezos from home-built 3-channel walking electronics constructed from a system of relays. Additionally, the design includes a lateral walker to change the lateral position of the tip. A piezo tube actuator provides fine positioning and raster motion for scanning.

Modest alterations to the experimental setup from its previous configuration have been proposed and in some cases fulfilled in order to accommodate operational obstacles. I will introduce these modifications and contrast them to their previous arrangements as it becomes relevant to the discussion of the design of the VT-AFM.

4.1 CRYOSTAT AND LOW-TEMPERATURE OPERATION

The body of the microscope (see fig. 4.1(b)) is designed to be compact. One of the advantages of this compact design is the rapid thermal cycling. The design permits suspending the microscope body from a stainless steel tube which is inserted into a narrow stainless steel vacuum can with a 1.25" outer diameter. The 0.035" thick wall of the stainless steel vacuum can is thin to minimize heat loss due to thermal conduction. A four-way cross at the top of the tube terminated at each leg by 2-3/4 inch conflat flanges provides an inlet for an optical fiber feedthrough, a vacuum port, and a Detoronics 41-pin electrical feedthrough.

After high vacuum is achieved, the entire microscope cryostat can be immersed either directly into a cryogen bath or into a cryostat. The relative abundance and low cost of liquid nitrogen make it a good candidate for direct immersion of the VT-AFM. The electrical feedthrough enables electrical signals from the VT-AFM at cryogenic temperatures to be measured and processed at room temperature, eliminating the need for electronics to be adapted for operation in a cryogenic environment.

For experiments requiring access to temperatures below liquid nitrogen temperature we prefer to use a Kadel Engineering dewar. The Kadel dewar is vapor-shielded and an Oxford Instruments superconducting coil magnet is integrated into the dewar, allowing for applied magnetic fields as high as 8 T. Alternatively, helium dewars can be equipped with a liquid nitrogen jacket for heat shielding but turbulence due to liquid nitrogen boil-off can produce unwanted vibration. The compactness of the microscope and tight tolerances of the cryostat provide the added benefit of compatibility with small bore magnets, driving down the cost of the coil magnet by requiring less

material to construct the magnet and reducing liquid cryogen consumption during operation.

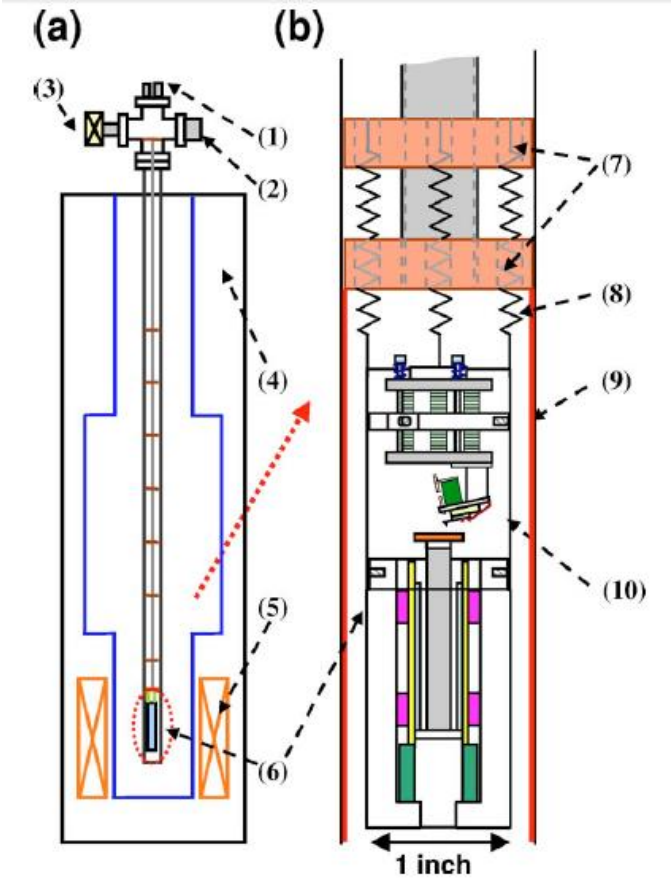

Figure 4.1 (a) Schematic drawing of VT-AFM and cryostat from ref. [74]. (1) Optical fiber feedthrough and BNC electrical feedthrough. (2) 41-pin electrical feedthrough. (3) Valve and gauge. (4) Helium Dewar. (5) Superconducting magnet. (6) LT-SFM body. (b) Zoom in of LT-SFM body inside the pipe. (7) OFHC heatsink. (8) Optional spring. (9) Copper sheath on the inner wall. (10) Microscope main body.

A support for the microscope is constructed from a platform anchored to an optical table and a pipe that sits between a clamp below and a forked clamp above. The pipe is aligned concentric to a pole in the platform and the lower clamp is fastened directly to the pole but underneath the pipe. A flange below the feedthrough of the

microscope rests above the forked clamp, propping the microscope up over the top of the pipe. Then the height of the pipe and thus the microscope are adjusted by adjusting the position of the lower clamp. This allows adjustment of the position of the microscope with respect to the level of the cryogenic bath for either direct immersion or vapor cooling where the microscope hovers above the bath.

The stainless steel tube from which the microscope is suspended is 50” in length, the vacuum can is 53” long including the flange and the electrical interface extends the length of the entire microscope cryostat to beyond 60”. The Kadel dewar is 55” in length, thus a clearance greater than 10’ is required to insert the cryostat into the dewar. Due to this required clearance, the cryostat support had to be relocated to another part of the lab, one end of the platform for the cryostat support had to be shaved off, and a system of ropes and pulleys suspended from the ceiling for hoisting the cryostat needed to be implemented in order to use the Kadel dewar.

Once in the cryostat under high vacuum, the body of the microscope is cooled mainly by radiative cooling from the inner wall of the vacuum can. Six baffles are attached to the stainless steel tube minimize heat loss due to room temperature radiation. Two copper heatsinks are also attached to the bottom of the tube, which are in thermal contact via an Oxygen-Free High Conductivity rod. Copper wires running from connectors for the microscope to the electrical feedthrough above at room temperature are thermally anchored to the OFHC rod.

Originally, when the VT-AFM design was completed, a means to improve the thermal link between the copper Heatsink and the inner wall of the vacuum can was proposed. Widening the bottom of the vacuum can and inserting a copper sheath that would contact both the copper heatsinks and the wall of the vacuum can simultaneously

was recommended.[74] Alternatively, we have used helium gas to facilitate thermal exchange between the microscope and the inner wall of the vacuum can. Using exchange gas also provides the added benefit of damping cantilever motion and reducing the cantilever quality factor that increases under high vacuum, so that a long ring-down time for the cantilever can be avoided. In addition, helium exchange gas can be introduced into the Kadel dewar to facilitate heat exchange between the liquid cryogen reservoir and the microscope cryostat. Fig. 4.2(a) shows a typical cooling curve of the VT-AFM sample stage to liquid nitrogen temperatures.

Two 50 Ω, 1 W metal film resistors are mounted with thermally conductive epoxy on either side of the sample stage for varying the sample temperature and a LakeShore Cryogenics Cernox sensor is epoxied underneath the sample stage. A Stanford Research Systems (SRS) 830 lock-in amplifier provides an AC reference voltage at a particular frequency that is applied across the Cernox sensor. The resulting voltage across the Cernox sensor is read into a National Instruments LabVIEW program through a GPIB interface between the SRS lock-in and a PCI data acquisition card. The LabVIEW program converts the voltage response from the Cernox sensor into a resistance which can then be converted to a temperature using a calibration curve. Upon input of a desired temperature into a separate LabVIEW program that is interfaced via a 9-pin serial port connector to an SRS SIM960 PID Controller, the program adjusts the current fed into the metal film resistors which heat the sample stage via Joule heating.

Once an experiment is completed, any remaining cryogens can be removed from the dewar and the microscope cryostat, still filled with helium exchange gas, can be left in the dewar to warm up. If the Kadel dewar is used, gas pressure in the space surrounding the microscope cryostat is prone to build during warm-up so that either a

safety valve or pumping down on the space with a roughing pump during warm-up is necessary to prevent forceful ejection of the microscope cryostat. Flowing either helium or nitrogen gas through the liquid cryogen reservoir during warm-up also ensures that water vapor from the air does not condense into the reservoir. Care must be taken not to warm up the system too rapidly in order to prevent damage to the piezos, but the rate of temperature increase is satisfactorily slow using the methods described here. A typical warm-up curve is given in fig. 4.2(b).

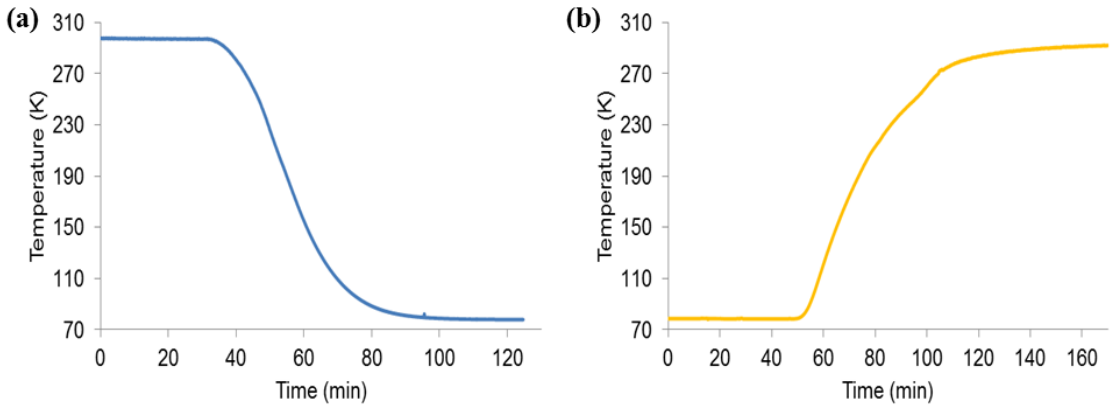

Figure 4.2 (a)Cooling and (b) warming curves of the VT-AFM sample stage obtained using a Cernox temperature sensor.

4.2 FIBER-OPTIC INTERFEROMETER

Of the deflection sensing techniques published in the literature, really only two methods- piezoresistive cantilevers[75] and fiber-optic interferometry[76] (Rugar et al. 1989) are suited to low-temperature AFM operation. The more popular beam-bounce method employed in many commercial AFMs encounters problems at low temperature, among them are difficulty in aligning the cantilever and sensor and inoperability of laser diodes and photodiodes in that temperature range. Piezoresistive cantilevers are in short supply,

however, and deposition of magnetic material on the end of the cantilever is required for local magnetic measurements. In this case, tracking the deflection of readily-available commercial cantilevers (usually silicon-based) under a fiber-optic interferometer appears to be a feasible route and allows for more measurement versatility.

Previously, an InGaAsP Fabry-Perot laser diode with a wavelength of 1310 nm, manufactured by PD-LD, was used as a light source for the interferometer. This wavelength is chosen because it lies above the absorption bandgap of silicon, minimizing heating of cantilevers and thermal noise. For laser stability, the original design included coupling the diode to a copper heatsink that was thermally connected to a thermistor. During standard operation of the interferometer, we did not find it necessary to use the thermistor. Over time the performance of the diode degraded, however, and employing the thermistor did not slow its decline. The performance of the homebuilt current source for the laser appeared normal. Anticipating that some of the electronic components in the photodiode preamplifier may have also broken down, new electronic components were installed in the photodiode preamplifier circuit but to no avail. To address this, a Thorlabs S1FC1310 Fabry-Perot benchtop laser source was installed to serve as a light source for the interferometer.

The laser light source is equipped with an FC/PC bulkhead connector for easy connection to the optical fiber which joins the laser output to the primary input of a 10/90 coupler. The coupler splits the laser light, transmitting 90% of the light through the primary output, and the remaining 10% through the secondary output. The primary output, terminated with an FC/APC connector to minimize light reflected back to the coupler, serves as a reference signal which can be monitored to measure the laser performance. The coupler also attenuates back-reflection to the laser source to prevent

instabilities in the laser due to optical feedback. The secondary output of the coupler is connected to an unjacketed Corning SMF-28 single mode optical fiber which is fed into the microscope cryostat via a vacuum feedthrough. The end of the fiber is cleaved by hand to be as flat as possible and produces some back-reflection of incident light. It is also positioned by hand above the back of the cantilever whose surface is usually treated to be highly reflective. The light reflected by the back of the cantilever reenters the fiber and interferes with the back-reflected light from the glass-air interface. Ultimately, the cantilever deflection is measured from this interference. Of the light reentering the coupler, 10% of the light back-reflected from the secondary output plus 90% of the light back-reflected from the primary output returns to the laser while 90% of the back-reflected light from the secondary output plus 10% of the back-reflected light from the primary output is transmitted through the secondary input of the coupler. Hence back-reflection into the laser source is minimal and the secondary input provides the interference signal. The secondary input is terminated by an FC/APC connector which is connected to the FC input of a Thorlabs PDA10CS InGaAs transimpedance amplified photodetector with switchable gain which detects and amplifies the interference signal.

We treat the interference between the light wave reflected from the cleaved end of the fiber and the light wave reentering the fiber core after being reflected from the back of the cantilever as interference between two coherent plane waves. The total wave equation, $\psi(\vec{\boldsymbol{r}}, t)$, is a superposition of the two waves $\psi_1(\vec{\boldsymbol{r}}, t)$ and $\psi_2(\vec{\boldsymbol{r}}, t)$:

$$\psi(\vec{\boldsymbol{r}}, t) = \psi_1(\vec{\boldsymbol{r}}, t) + \psi_2(\vec{\boldsymbol{r}}, t) = A_1(\vec{\boldsymbol{r}})e^{-i[\omega t - \varphi_1(\vec{\boldsymbol{r}})]} + A_2(\vec{\boldsymbol{r}})e^{-i[\omega t - \varphi_2(\vec{\boldsymbol{r}})]}. \quad (4.1)$$

The intensity of the reflected wave, $I(\vec{\boldsymbol{r}})$, is proportional to the modulus squared of the wave function and has the form:

$$I(\vec{\boldsymbol{r}}) = I_1(\vec{\boldsymbol{r}})^2 + I_2(\vec{\boldsymbol{r}})^2 + 2\sqrt{I_1(\vec{\boldsymbol{r}})I_2(\vec{\boldsymbol{r}})}\cos[\varphi_1(\vec{\boldsymbol{r}}) - \varphi_2(\vec{\boldsymbol{r}})]. \quad (4.2)$$

The expression for the reflected power, P, is related to the reflected intensity when we consider the transmission and reflection intensity coefficients of the fiber and the reflection intensity coefficient of the cantilever, that is:

$$P = P_0\left(R_f + R_c{T_f}^2 + 2\sqrt{R_f R_c}\cos\Delta\varphi\right) = P_0[R_f + R_c(1-R_f)^2 + 2\sqrt{R_f R_c}\cos\Delta\varphi]\,. \tag{4.3}$$

where P_0 is the power of the incident light, R_f and R_c are the reflected intensity coefficients of the fiber and cantilever, respectively, and T_f is the transmission intensity coefficient of the fiber. The square of the transmission intensity coefficient in the second term of the expression reflects the requirement that the incident light be first transmitted to the back of the cantilever and then transmitted back into the fiber after it is reflected by the cantilever.

It is useful here to consider the average power, P_{av}:

$$P_{av} = P_0\left[R_f + R_c\left(1-R_f\right)^2\right]. \tag{4.4}$$

Given the index of refraction for the Corning SMF-28 single mode fiber provided by the specification sheet we can calculate R_f to be:

$$R_f = \left(\frac{n_{fiber}-n_{air}}{n_{fiber}-n_{air}}\right)^2 \sim 3.5\%\,. \tag{4.5}$$

Considering $R_f \ll 1$, eqn. 4.4 reduces to:

$$P_{av} \cong P_0\left(R_f + R_c\right), \tag{4.6}$$

and eqn. 4.3 becomes:

$$P = P_{av}\left[1 + \frac{2\sqrt{R_f R_c}}{\left(R_f + R_c\right)}\cos\Delta\varphi\right].$$

The form of the phase difference in eqn. 4.6 above also follows from two-wave interference, that is:

$$\Delta\varphi = \frac{4\pi}{\lambda}d\,, \tag{4.7}$$

where λ is the wavelength of the light and d is the fiber-cantilever separation. Given eqn.'s 4.6 and 4.7 we can arrive at an analytical expression for dependence of the power on the fiber-cantilever separation:

$$\frac{\Delta P}{\Delta d} \propto \sin\left(\frac{4\pi d}{\lambda}\right) . \tag{4.8}$$

Thus the interferometer is most sensitive to cantilever motion when the fiber-cantilever separation is odd multiples of an eighth of the wavelength, or:

$$d = (2n-1)\frac{\lambda}{8} , n = 1, 2, 3, \ldots \tag{4.9}$$

Beyond the initial alignment of the fiber above the back of the cantilever, the fiber-cantilever distance is further controlled by coupling the fiber to a piezostack and an optimal distance is maintained during operation using a homebuilt proportional-integral (PI) controller.

To calibrate the interferometer, the interference signal is measured as a function of fiber-cantilever distance by sweeping through a range of voltages applied to the piezoelectric stack. The output of the photodetector is DC coupled to the input of an Agilent 34401A digital multimeter which displays the average voltage signal from the photodetector. The display of the multimeter is read via a GPIB interface into LabVIEW software that compares the voltage signal at the fringe peaks and troughs, which are averaged to serve as a setpoint for the PI controller. The region of the interference fringe where the signal responds linearly to a voltage change in the piezostack, and hence a change in fiber-cantilever distance, provides a limit on the AC voltage used to excite cantilever motion. After the multimeter, the deflection signal is interfaced to the NanoScope™ controller and a homebuilt PI controller for the interferometer in parallel.

Our homebuilt PI controller features a multi-stage circuit. One stage features a variable resistor following a precision voltage reference which determines the setpoint of

the PI controller. Another stage features a differential amplifier that compares the voltage signal of the deflection input to the setpoint and outputs the difference between the two with a gain of unity. RC filters on both the setpoint voltage and deflection input ahead of the differential amplifier attenuate signals with frequencies above 100 Hz. The next stage features an integrator circuit and proportional response circuit connected in parallel to a summing amplifier. The gain of the proportional response is controlled using a variable resistor and the time constant of the integrator is controlled by switching between multiple terminals, each with a distinct resistance. An inverting amplifier allows the slope of the response to be switched and the final stage includes a high-voltage power operational amplifier which can access the full range of the fiber piezostack extension for fixing in on a fringe. An offset stage allows for varying the voltage output to the piezostack up to 120 VDC to sweep through fringes.

An alternative design for the PI controller is included in Appendix A that does not require a high-voltage operational amplifier to provide the output to the piezostack in order to adjust and maintain the optimal fiber-cantilever distance. This provides a reduction in cost of the materials as well as the operation of the PI controller. The range of output voltage to the piezostack is reduced from 120 V to ±15 V, potentially reducing the power output by a factor of 8. Also a voltage follower prior to the differential stage stabilizes the voltage signal of the deflection input.

At liquid nitrogen temperatures, the capacitance of the piezostack reduces by a factor of six and at helium temperatures the performance of the piezostack is so diminished that a full fringe cannot be resolved given the full range of the applied DC voltage. For low temperature use, proper alignment of the piezostack is essential.

Consider a representative schematic of the fiber-cantilever holder design currently in use presented in fig. 4.3.

The piezostack will provide maximal extension when it is oriented perpendicular to the plane of the cantilever chip. The epoxy joint at point (4) fails fairly frequently, shearing off the end of the piezostack casing. To repair this optimally, the surface of the fiber-cantilever mounting base at point (4) must be flat and the surface of the piezostack casing must also be flat prior to epoxy application. Repeated damage to the piezostack casing guarantees that this is not the case. Moreover, the piezo plate to drive cantilever motion is also not guaranteed to be flat against the surface of the fiber-cantilever mounting base. An angle (β in fig. 4.3) between the piezostack and the surface of the fiber-cantilever mounting base other than 90° can reduce the total range of displacement between the end of the optical fiber and cantilever.

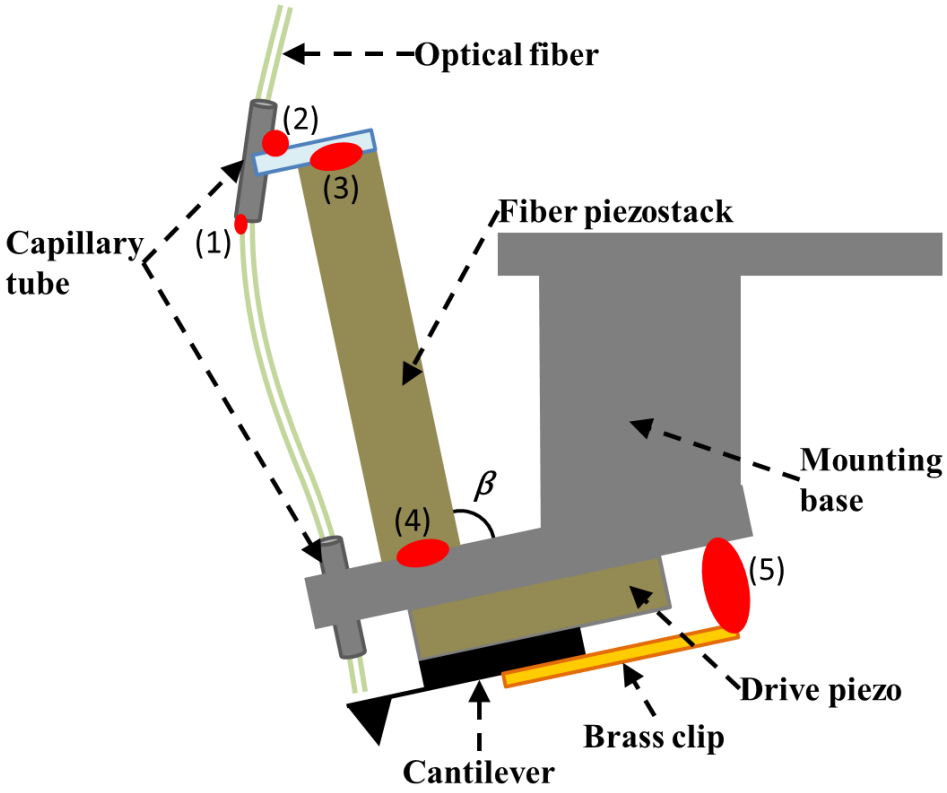

Figure 4.3 Schematic drawing of the fiber-cantilever holder (side view) with red spots indicating locations of epoxy joints labeled (1)-(5).

To address this issue, a modification to the fiber-cantilever mounting base is proposed such that a support beneath the piezostack adjusting the fiber position is used to ensure proper alignment and also reduce the torque about the epoxy joint at point (4) that arises from regular handling. An additional site-specific clamp would also ensure that the piezostack is in good contact with the fiber-cantilever mounting base at point (4) during repair. Additionally, this clamp could also hold the fiber guide with capillary tube in place during repair of the epoxy joints at points (1), (2), and (3). Currently, epoxy joint (1) is necessarily broken each time the fiber needs to be re-cleaved and the joint at (2) is often broken in tandem. Potentially, the epoxy joint at point (2) could be eliminated

entirely by constructing a fiber guide by welding a stainless steel tube to a plate. A schematic drawing of the proposed modifications to the fiber-cantilever mounting base is shown in fig. 4.4.

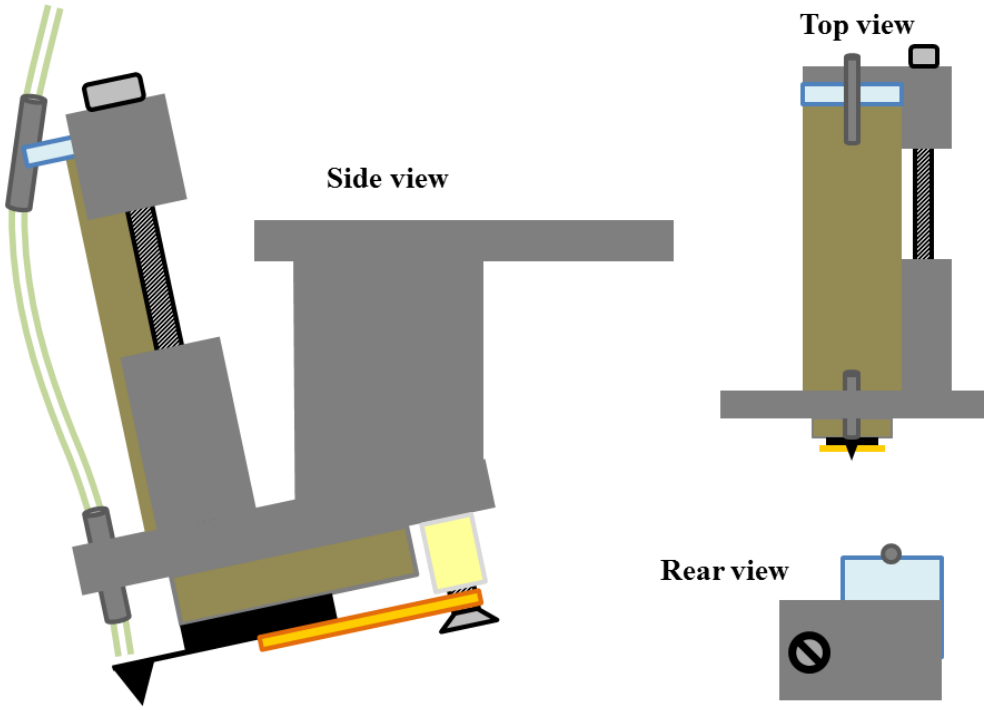

Figure 4.4 Schematic drawing of the fiber-cantilever mounting base featuring a removable clamp for ensuring proper alignment and support of the fiber piezostack and fiber guide during repair. This schematic also includes a screw to clamp the cantilever clip.

4.3 VERTICAL AND LATERAL POSITIONERS

The Pan-style coarse approach mechanism[77], known to perform reliably even at low temperatures, is the basis for the vertical walker implemented in this VT-AFM design. The "legs" of the walker are comprised of three piezostacks coupled mechanically to titanium rods which have sapphire pads attached to them. These sapphire

pads are in contact with a corresponding set of sapphire pads attached to a stainless steel tube that surrounds the sample stage and piezo tube scanner. Two of the legs are fixed with respect to the body of the microscope while the third leg is clinched by a stainless steel spring plate. The spring plate provides the necessary tension for friction between the sapphire plates to produce stick-slip motion of the sample stage. Given that the cantilever remains fixed, walking the sample upwards toward the tip is accomplished by applying a DC voltage simultaneously to the three piezostacks. The sample stage displaces with the extension of the piezostacks because of the static friction between the sapphire plates. Then the voltage to each piezostack is abruptly lowered, one after another in rapid succession, overcoming the static friction between the sapphire plates and allowing the leg to slip without displacing the sample stage. This sequence of voltage pulses for the three walker legs constitutes one step upward. Stepping upward continues until an amplitude setpoint input to the NanoScope™ controller is reached and contact has been achieved. Reversing the polarity of the voltage pulse sequence reverses the motion and downward motion of the sample stage occurs.

The sawtooth profile of the voltage pulses to the legs originally required complicated electronics that were eventually replaced using an ingeniously simple design published recently.[78] Basically, the intrinsic delay in switching to the "on" state of the mechanical relays provides the slow actuation part of walking and the quick switch to the "off" state provides the fast actuation. Because walking is accomplished by actuating three piezostacks, a three-channel circuit is required rather than a six-channel circuit as published in the literature.

Originally, the VT-AFM design provided for a lateral walker for lateral displacement of the tip. This walker also operated on the principle of stick-slip motion

but the legs for the walker were constructed by sandwiching shear piezo plates that displace orthogonally to one another. The current design is presented in fig. 4.5.

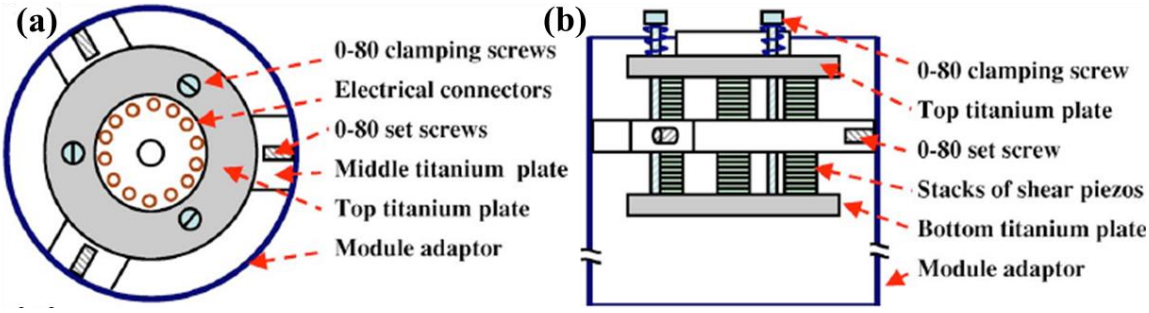

Figure 4.5 (a) Top and (b) side view of the lateral positioner schematic drawing from ref. [74].

It features upper and lower titanium plates which are clamped to a middle plate, also titanium. A group of three stacks of shear piezo plates are epoxied on either of the middle plate. A sapphire plate is epoxied to the end of each stack as well as to the top and bottom titanium plates so that the stacks and the upper and lower plates may slide against one another. The range of the lateral walker is estimated to be a circle of 3.3 mm, limited by the diameter of the SFM body. Again, complicated walking electronics were required to provide a sawtooth voltage profile and the number of conductive epoxy joints (12 epoxy joints with 1 epoxy joint per two shear piezo plates with four piezo plates per stack and 6 shear piezo plate stacks) between plates and the number of wires required (13 connections with 1 wire per shear piezo plate stack per direction for 6 shear piezo plate stacks and 1 common connection) made the lateral walker susceptible to failure at multiple points. A simpler design would be to replace the 6 stacks of shear piezos with a two piezostacks (see fig. 4.6). It features fewer epoxy joints and wired connections,

conforms to the geometry already present in the current design, and can utilize walker electronics already implemented for the vertical walker.

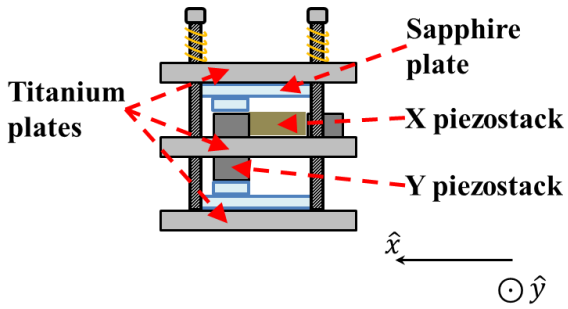

Figure 4.6 Schematic drawing of an alternate design for the lateral positioner (side view).

4.4 PIEZOELECTRIC TUBE SCANNER

The Pan-style coarse approach mechanism, known to perform reliably even at low temperatures, is the basis for the vertical walker implemented finer control of vertical and lateral displacement of the sample stage is accomplished by attaching the sample stage to one end of a piezo tube scanner. A piezo tube scanner is constructed by coating the outer and inner surface of a tube made of piezoelectric ceramic material with a metallic layer and then quartering the outer electrode by removing some of the metallized coating.

The sample stage moves along the x-axis (y-axis) by varying the voltage applied to the x- and y-electrodes with respect to a fixed voltage applied to the inner electrode. Varying the voltage applied to the inner electrode with respect to a fixed voltage applied to the x- and y-electrodes produces motion of the sample stage in the z-direction.

Quantitatively, the lateral and vertical motions are determined by:

$$\delta x = \frac{2\sqrt{2}}{\pi} d_{31} \frac{V_x}{t} \frac{L^2}{2r}, \tag{4.10}$$

$$\delta z = d_{31} \frac{V_z}{t} L, \tag{4.11}$$

where d_{31} is the piezo electric coefficient of the scanner tube material, V_x and V_z are the voltages applied to one of the outer electrodes and to the inner electrode, respectively, and L, t, and r are the length, thickness and inner radius of the scanner tube. For the EBL Products Inc. piezo tube scanner used in this design and a maximum voltage of 200 V applied to the outer electrodes, we can expect a maximum lateral scanning range of 90 μm and a vertical scanning range of 11 μm at room temperature and a maximum lateral scanning range of 30 μm and a vertical scanning range of 4 μm at liquid nitrogen temperature.

Over the course of normal operation and multiple scans we expect piezo performance to change and we also anticipate variation in the performance of one piezo tube scanner to another. In addition, when piezo tube scanners have broken, we have filed them down to the remainder of their usable length. To compensate for this, we scan a reference sample with features of characteristic size to calibrate the voltages applied to the piezo tube scanner during scanning. Using a reference sample, the lateral range of the piezo tube scanner currently in use in our setup is reduced by a factor of 4 and the vertical scanning range is reduced by a factor of 3 when scanning at liquid nitrogen temperatures versus scanning at room temperature. This is fairly consistent with the maximum scanning range calculations.

Chapter 5: $LaCoO_3$

Transition metal oxide compounds with perovskite and perovskite-like structures have garnered much attention due to the wide range of electronic phenomena they exhibit, among them colossal magnetoresistance[79], superconductivity[80], ferromagnetism[81], ferroelectricity and multiferroicity[82]. The rare-earth cobaltite family, $LnCoO_3$ (fig. Figure 5.1), has received continued interest as structural changes due thermal expansion and ionic radius of the rare-earth element determine transport and magnetic properties.[83,84,85] The sensitivity of weakly distorted CoO_6 octahedra to temperature and decreases in ionic radius is the expected source of anomalous thermal expansion behavior that coincides with changes in the spin state of the Co ion and insulator-metal transitions.

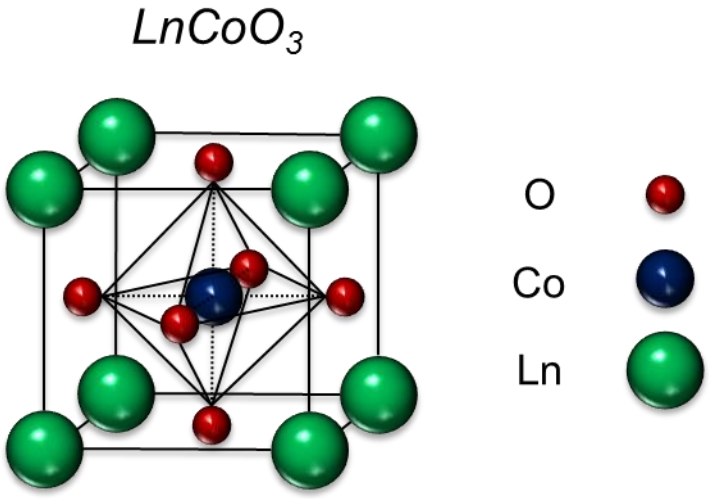

Figure 5.1 Perovskite crystal structure of lanthanide cobaltites.

For an isolated Co ion, all 3*d* orbitals are degenerate in energy. When the Co ion is octahedrally coordinated by oxygen atoms in a perovskite crystal, however, the lobes of the d_{xz}, d_{yz}, and d_{xy} orbitals that point between the ligands are lower in energy with

respect to the d_z^2 and $d_{x^2-y^2}$ orbitals. d_{xz}, d_{yz}, and d_{xy} orbitals are grouped and labeled t_{2g} states and d_z^2 and $d_{x^2-y^2}$ orbitals are grouped and labeled as e_g states. The magnitude of the energy difference between t_{2g} and e_g states, referred to as the crystal field splitting energy, when compared to the Hund's exchange energy determines which states electrons fill when the Co ion is introduced into a crystal field. It is easy to imagine that a distortion in the Co-O-Co bond length or bond angle might drop e_g states in energy, reducing repulsion of electrons from the negative lobes of d_z^2 and $d_{x^2-y^2}$ orbitals and altering the relationship between the crystal field splitting and Hund's exchange energies. This is the fundamental description explaining transitions of the spin state of Co ions that occur with distortion of CoO_6 octahedra prompted by thermal expansion and chemical pressure.

Of the rare-earth cobaltites, $LaCoO_3$ is particularly unique. Unlike other members of the $LnCoO_3$ family, stoichiometric $LaCoO_3$ features a rhombohedrally distorted perovskite cubic structure contrary to the orthorhombic distortion characteristically observed in other rare-earth cobalt oxide compounds. $LaCoO_3$ also has a complex and widely-debated magnetic character. For Co^{3+} ions with a $3d^6$ electron configuration, bulk $LaCoO_3$ in the ground state is non-magnetic with electrons filling t_{2g} states completely. This configuration is considered the low-spin (LS) ($t_{2g}^6 e_g^0$, S = 0) state. Bulk $LaCoO_3$ transitions from nonmagnetic to paramagnetic behavior in the temperature range 35 K < T < 100 K and another transition in the interval 300 K < T < 600 K which is accompanied by a semiconductor−metal transition.[86,87,88,89,90] These transitions reflect a distortion in the CoO_6 octahedra which stabilizes population of e_g states, resulting in either an intermediate-spin (IS) ($t_{2g}^5 e_g^1$, S = 1) or high-spin (HS) ($t_{2g}^4 e_g^2$, S = 2) state. The temperature dependence of these spin-state transitions reflects the role of structural

distortion of the LCO lattice in altering the configuration of Co ions. A main point of controversy for spin-state transitions in $LaCoO_3$ is whether the spin-state transition is from LS to an IS or HS state or a mixture of spin-states, or even from LS to a mixture of Co ions with different valencies and spin-states. An added complication to the interplay of structure and electronic properties is ferroelastic behavior in $LaCoO_3$.[91,92]

Just as puzzling and intriguing is the observation of ferromagnetism at low temperatures in $LaCoO_3$ single crystals[93,94,95], powders[93,96], and nanoparticles[90,95,97], and nanowires[98]. Ferromagnetic (FM) ordering in these systems appears to conflict with the commonly-held expectation of a low-spin, nonmagnetic ground state of $LaCoO_3$ at low temperatures. Measurements performed on nanoparticles demonstrate that unit cell volume and ferromagnetic moment exhibit a nearly linear dependence on the inverse of nanoparticle size, indicating that lattice distortion is the source of ferromagnetism in nanoparticles.[99]

Ferromagnetism in strained thin films of $LaCoO_3$ at low temperature has also been observed and reported on extensively.[100,101,102,103,104,105] Manufacturing strain states in thin films of $LaCoO_3$ by depositing them on substrates with commensurate structures that feature differing degrees of lattice mismatch provides a practical means to further examine the correlation between structure and electronic behavior in $LaCoO_3$. Inducing and tuning some of these electronic transitions by engineering the structure of $LaCoO_3$ with the deliberate introduction of strain also open possible avenues for device applications, some of which have already been realized for unstrained[106,107] and strained[108] $LaCoO_3$ thin films.

A great deal of debate focuses on the mechanisms by which Co ions order ferromagnetically at low temperatures in $LaCoO_3$ in these systems. It remains an open

question whether magnetic exchange amongst Co^{+3} ions in an intermediate-spin or a high-spin state is enough to bring about FM ordering or if it must be facilitated by the presence of magnetic Co^{2+} and Co^{4+} ions introduced by hole or electron doping. Also discussed in some detail in the chapter ahead is the observation that samples in different forms prepared by different methods show nearly the same Curie temperature (T_C) value, $T_C \sim 85$ K, including the thin film samples synthesized for this study.

This chapter aims to discuss the experimental signatures, global and local in nature, of ferromagnetic ordering in strained $LaCoO_3$ thin films and how they have been interpreted to reflect the configuration of Co ions in their various states. Direct imaging of local magnetic domains in strained $LaCoO_3$ thin films using magnetic force microscopy emerges as a necessary tool to characterize the local magnetic behavior as it pertains to the debate of whether spin-state transitions of Co^{3+} ions drive ferromagnetic behavior or local compositional variation. Results of SQUID magnetometry, x-ray diffractometry and magnetic force microscopy are presented for thin film samples of $LaCoO_3$ deposited on substrates of $LaAlO_3$, $SrTiO_3$, and $BaTiO_3$ using molecular beam epitaxy, each substrate imposing a different degree of strain on the LCO thin films.

5.1 STRAIN EFFECTS IN THIN FILMS OF $LaCoO_3$

In contrast to the rhombohedrally distorted perovskite structure observed in bulk $LaCoO_3$, substrate strain imposed on thin films of LCO induces a pseudotetragonal unit cell structure in LCO, depending on the choice of substrate.[109] At particular values of strain the LCO unit cell assumes a pseudocubic structure[109], which is expected to render thin film LCO nonmagnetic at low temperature[110]. Polycrystalline films have also been reported to exhibit paramagnetic behavior similar to bulk LCO.[100,111]

Initially, magnetization in thin films of LCO was shown to increase with increasing strain, whereas the Curie temperature appeared to saturate at $T_C \approx 85$K.[112] More recent work has suggested that not just the magnitude of strain but the sign of strain is significant for producing ferromagnetic films. Where numerous results indicate that compressive strain does not stabilize long-range ferromagnetic order in strained thin films[104,113,114,115,116], there are still a number of experimental and theoretical reports[110,112,117] which report ferromagnetism in films deposited on $LaAlO_3$ (LAO), under compressive strain. Featured later in this chapter are measurements for two LCO thin films grown on LAO where one sample is clearly shown to be ferromagnetic while the other is not.

The most recent study of compressively-strained LCO thin films deposited on LAO substrates with different crystallographic orientations revealed a ferromagnetic transition at $T_C \approx 85$ K for all LCO epitaxial films on (100) LAO, very weak ferromagnetism for films on (110) LAO, and ambiguous results for films on LAO (111).[117] It is expected that tetragonal distortion of CoO_6 octahedra is dominant in the LCO film on (100) LAO, while the rotation of CoO_6 octahedron is dominant in LCO film on (111) LAO, with the octahedra in LCO deposited on (110) LAO occupying some intermediate configuration, though this was not directly measured. Instead it was inferred that local distortion of the octahedra probably occurred for the largest out-of-plane strains reported for the LCO films on (100) LAO.

Given the tendency for strain in thicker films with a uniform crystallographic direction to be slightly relaxed due to the lattice relaxation effect[118], the linear relation between saturation magnetization and increasing thickness for strained LCO thin films beyond a particular thickness as observed in ref. [100] seems to support a picture where

exchange between a fractional population of higher-spin Co^{3+} ions and low-spin Co^{3+} ions drives ferromagnetic ordering. Echoed somewhat in the literature, this explains observation of higher magnetization values for thicker films than thinner films despite partial relaxation of strain in thicker films and saturation in the dependence of Curie temperature with strain.[119]

Most theoretical models agree at least that lowering of symmetry in CoO_6 octahedra from cubic octahedral to tetragonal prompts spin-state transitions in strained thin films of LCO and that ferromagnetically ordered states can result from promotion of Co^{3+} from LS to higher-spin states. A strain-stabilized spin-state transition was first suggested to be a LS to HS/LS crossover[111,112] but was later suggested to be LS to IS or LS/IS based on density functional calculations[110,120]. Both scenarios have been shown to support various experimental and theoretical results, but a consensus is not yet achieved. The LS-IS crossover does appear at first glance to be a less likely configuration with more than one theoretical study arriving at a solution where the IS state is half-metallic[115,120] while experimental results are as yet conclusive that LCO is insulating at low temperatures. Interestingly, calculations performed to predict magnetic states of strained LCO involve constrained-volume calculations[120,121] where experiment indicates that volume is not conserved and increases slightly with increasing strain[109] which would indicate that lattice distortion is not fully accommodated by octahedral rotation and change in Co-O-Co bond angle.

Calculations featured in ref. [115] endorse a HS/LS mixture for tensile-strained LCO thin films with a lattice mismatch greater than 2.5%. Previous theory was not able to arrive at a spin-state transition even for high tensile strain despite many experimental reports of ferromagnetism in thin films of LCO on STO which features a lattice mismatch

of 2.56% between the film and substrate. But it still remains a point of debate that intermediate strain values and even compressive strain have been found to produce ferromagnetic films. This incompatibility of theoretical and experimental results could be resolved if defects affecting the local strain profile in LCO thin films and/or the presence of Co^{+2} or Co^{+4} ions with hole-doping or local chemical inhomogeneity were found to produce magnetic behavior in films that do not have the requisite strain to induce spin-state transitions. Ref. [115] also claims that the resulting magnetic structure at this level of strain is a collinear antiferromagnetic ordering of locally ferromagnetic domains. Several other non-collinear magnetic structures were also observed to be degenerate in energy with the collinear antiferromagnetic configuration, but this unique solution for the magnetic structure will reenter the discussion when results for local magnetic force microscopy measurement of domains presented later in the chapter.

5.2 PREVIOUS EXPERIMENTAL RESULTS FOR $LaCoO_3$ THIN FILMS

This section highlights experimental results obtained previously for $LaCoO_3$ thin films that are particularly relevant to the experimental results obtained by this author for this work. The content will be grouped according to whether the measurement technique and results are global or local in scale.

5.2.1 Global Measurement

5.2.1.1 Diffraction and Spectroscopic Analysis

Typical X-ray diffraction (XRD) results for epitaxial thin films of $LaCoO_3$ deposited on $LaAlO_3$ (001) substrates are shown in fig. 5.2. XRD results for epitaxial thin films of $LaCoO_3$ deposited on $SrTiO_3$ (001) are given in fig. 5.3. Differences between the

pseudocubic lattice parameter of bulk $LaCoO_3$ and that of the $LaAlO_3$ and $SrTiO_3$ substrates place substrate peaks just ahead and behind $LaCoO_3$ film peaks, respectively. The division of the $LaAlO_3$ (002) peak into two subpeaks in fig. 5.2(c) is attributed to minor imperfections due to twinning of the $LaAlO_3$ crystal along the [010] tilt axis.[122]

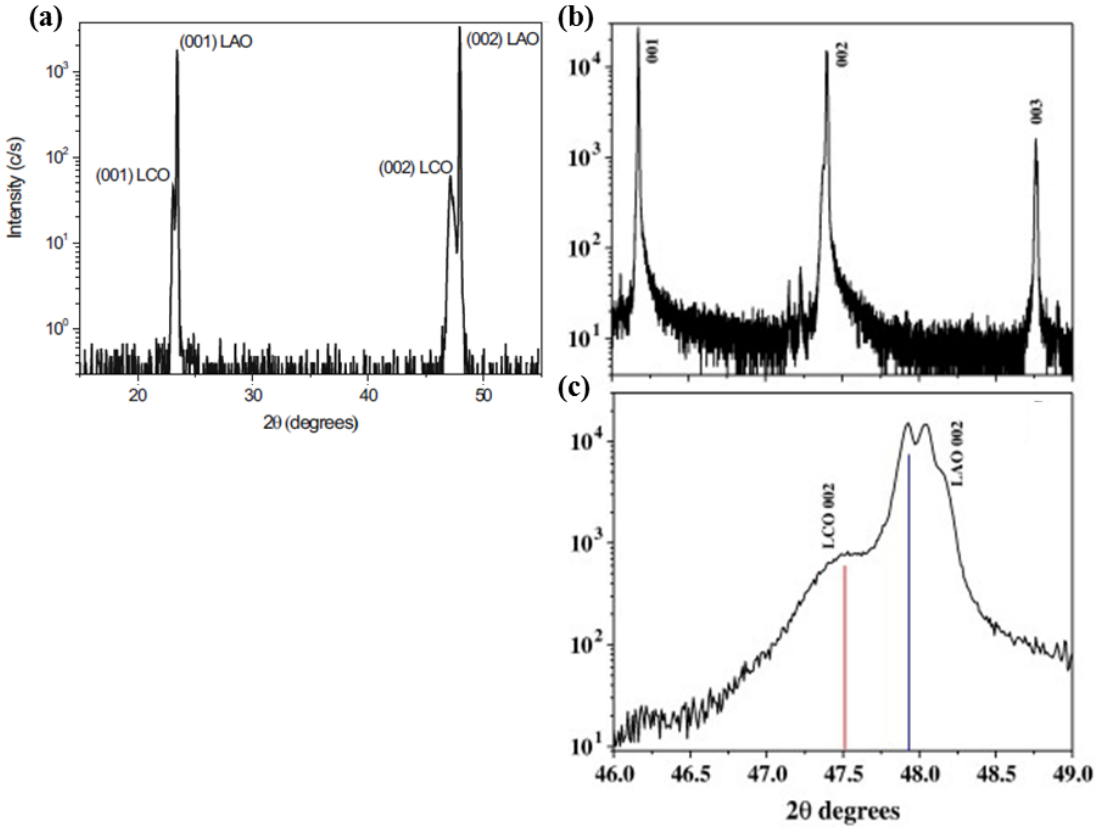

Figure 5.2 XRD results for thin films of epitaxial LCO deposited on $LaAlO_3$ substrates. (a) is taken from ref. [104] and (b), (c) are taken from ref. [122]. (c) Close-up of the region $46° < 2\theta < 49°$.

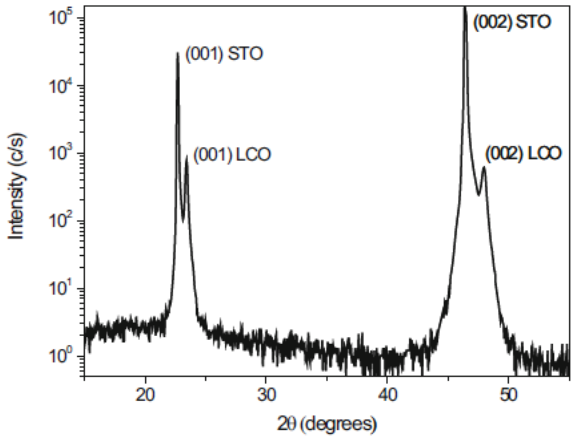

Figure 5.3 XRD results for a thin film of epitaxial LCO deposited on an $SrTiO_3$ substrate taken from ref. [104].

In the range of high tensile strain, few instances where $LaCoO_3$ films are deposited on substrates with a greater degree of lattice mismatch than $SrTiO_3$ (~2.63%) are reported. Dependence of XRD results on deposition temperature for an LCO film deposited on MgO substrates with a lattice mismatch of 9.7% are presented in fig. 5.4. The resultant LCO films were not single crystal and varied in texture between homogenous distributions of rounded grains to more densely distributed plate-like grains, on the scale of hundreds of nanometers in size. Though impurity peaks are significantly reduced with an increase in deposition temperature, they are not completely eradicated, as demonstrated by the disappearance of the La_2O_3 impurity peak for a deposition temperature of 700° and its reappearance in the film deposited at 800°. The authors took care to optimize the La:Co ratio for growth but found a slight excess of La in their films deposited on MgO. It is not clear if this is the cause of the La_2O_3 impurity peaks.[122]

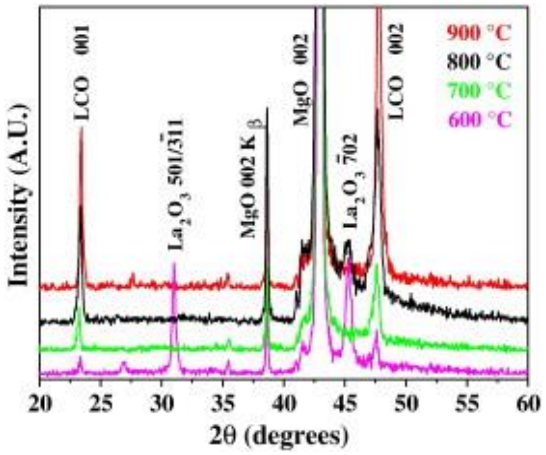

Figure 5.4 XRD patterns of $LaCoO_3$ films deposited on MgO (001) in the temperature range 600–900 °C from ref. [122].

XRD results shown in fig. 5.5 also confirm a tendency of thicker films to partially relax strain consistent with lattice relaxation effect reported in ref. [102].

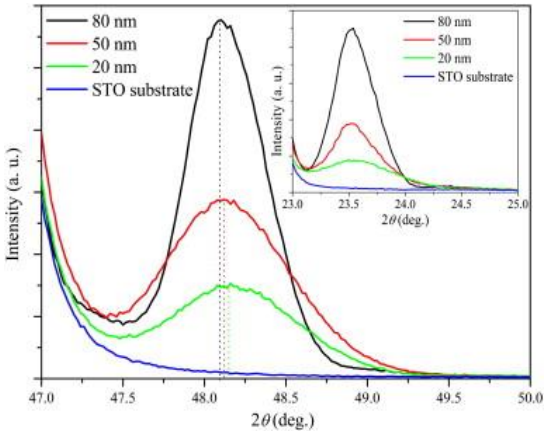

Figure 5.5 The (002) peaks in the XRD $\theta/2\theta$ symmetric scans of epitaxial $LaCoO_3$ thin films with different thicknesses deposited on $SrTiO_3$ substrates, taken from ref. [118]. Inset shows the (001) peaks of the LCO films.

In addition to diffraction data, X-ray absorption measurements provide a look at Co valence state and transitions from core O states to O 2*p* states hybridized with Co 3*d*, La5*d*, and Co 4*s*,*p* in $LaCoO_3$ samples. These measurements were used to confirm that the O spectra remains fairly fixed for epitaxially strained films of $LaCoO_3$ versus shifts in peak position and symmetry for polycrystalline $LaCoO_3$ films, as shown in fig. 5.6.[111] Biaxial tensile strain is expected to suppress octahedral rotation, freezing the spin state, which indicates that the ferromagnetic state in strained $LaCoO_3$ films is due to a high-spin configuration induced by structural distortion. Contributions from a small Co^{2+} signal were necessarily subtracted from the Co spectra (not shown) and by growth optimization could not be entirely avoided, which may indicate a residual oxygen deficiency.

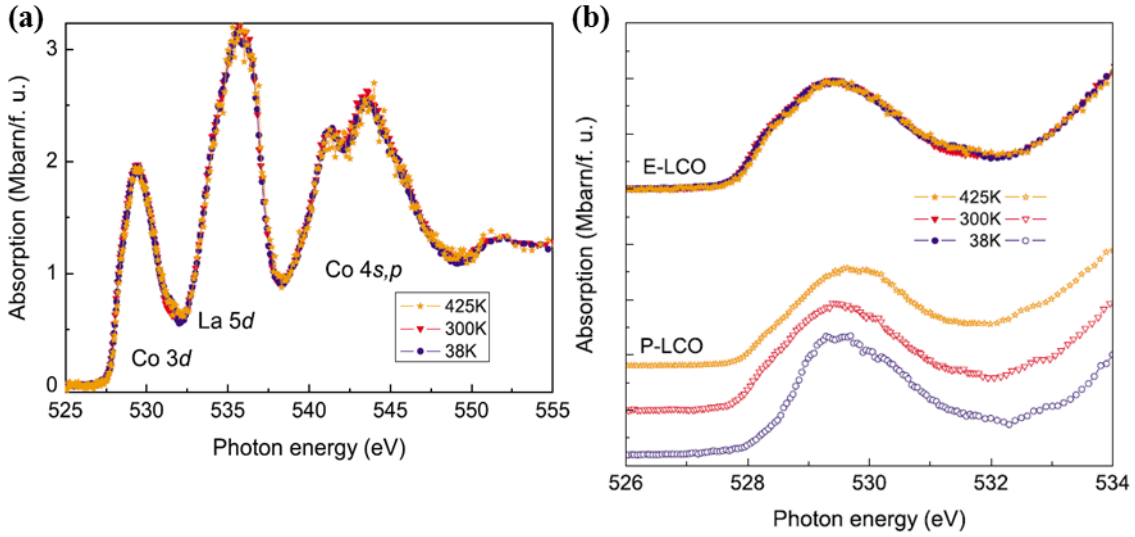

Figure 5.6 X-ray absorption results for LCO films taken from ref. [111]. (a) O 1*s* X-ray absorption spectra of an epitaxial thin film of $LaCoO_3$ taken at different temperatures. (b) O *K* low-energy region for an epitaxial $LaCoO_3$ film strained to an $(LaAlO_3)_{0.3}(Sr_2AlTaO_6)_{0.7}$ substrate (labelled "E-LCO") and a polycrystalline $LaCoO_3$ film (labelled "P-LCO"). The traces for P-LCO at different temperatures shown in (b) are offset for clarity.

That biaxial tensile strain locks Co ions in a high-spin state at low temperature seems to support the suggestion that biaxial compressive strain would cause increased octahedral rotation, producing a low-spin configuration. Magnetometry data, however, does not consistently show that $LaCoO_3$ thin films on $LaAlO_3$ under compressive strain are non-magnetic at low temperatures.

5.2.1.2 Magnetometry Data

Magnetization versus temperature data for LCO films on substrates with varying degrees of lattice mismatch does not indicate that an increase of tensile strain necessarily generates more magnetic moments.

As shown in fig. 5.7, there is a larger magnetic moment for LCO films on $(LaAlO_3)_{0.3}(Sr_2AlTaO_6)_{0.7}$ (LSAT) (001) substrates than those on $SrTiO_3$ (STO) (001) substrates which have a 1.84% and 2.63% lattice mismatch, respectively.

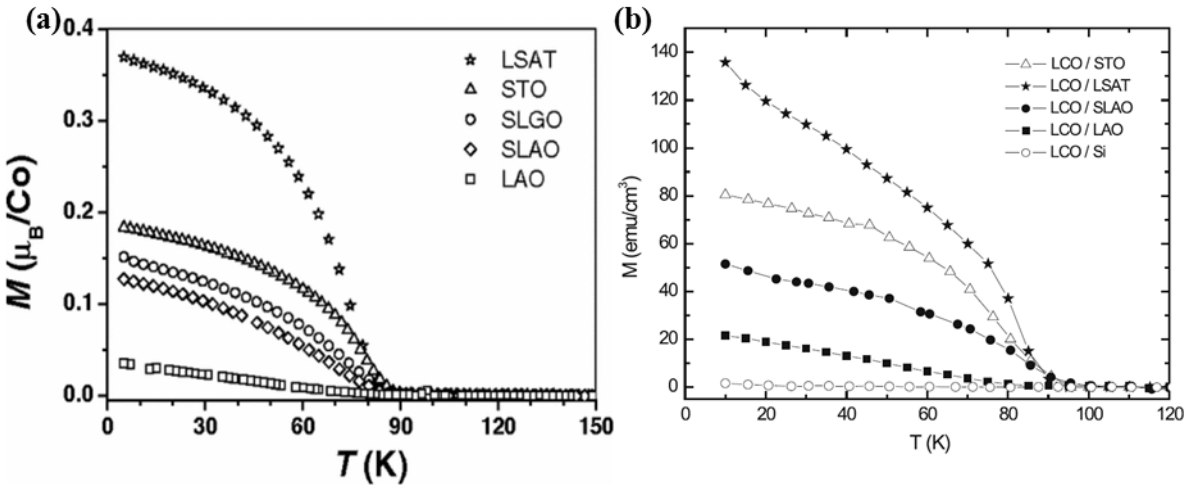

Figure 5.7 Field-cooled magnetization of LCO films on various substrate materials taken from (a) ref. [112] and (b) ref. [104]. Films were field-cooled in a magnetic field with a strength of (a) $\mu_0 H$=20 mT and (b) $\mu_0 H$=200 mT that was applied parallel to the film surface.

	D. Fuchs et al., ref. [112]		A. D. Rata et al., ref. [104]			
Substrate	Magnetic moment at 10K (μ_B/Co)	T_C (K)	Magnetic moment at 10K (μ_B/Co)	T_C (K)	H_C (mT)	Lattice mis-match (%)
$SrLaAlO_4$ (SLAO)	0.13	69	0.5	84	645	-1.31
$LaAlO_3$ (LAO)	0.03	43	0.3	75	475	-0.52
$(LaAlO_3)_{0.3}(Sr_2AlTaO_6)_{0.7}$ (LSAT)	0.37	76	0.8	85	560	1.84
$SrTiO_3$ (STO)	0.18	78	0.7	86	344	2.63

Table 5.1: Values of the magnetic moment at T=10 K and Curie temperature of 100 nm thick LCO thin films on various substrates taken from ref. [112] and ref. [104] and the room temperature values of substrate lattice mismatch (w.r.t. the bulk value of the LCO pseudocubic lattice parameter). Films were field-cooled in an in-plane magnetic field with a strength of 20 mT (ref. [112]) and 200 mT (ref. [104]).

Perhaps unexpectedly, susceptibility measurements between 100 K $\leq T \leq$ 150 K suggest that while the ferromagnetic moment for films deposited on STO below T_C is lower than films deposited on LSAT, the paramagnetic moment is greater for films deposited on STO above T_C (see fig. 5.8). The calculation assumes a single-ion picture that exhibits a Curie law temperature dependence of the magnetization with an effective paramagnetic moment μ_{eff} that varies with the Co-O-Co angle which is tied to the dimensions of the lattice. A lower ferromagnetic moment for a substrate that imposes

higher strain may be a result of strain relaxation beyond some critical in-plane tensile strain value.

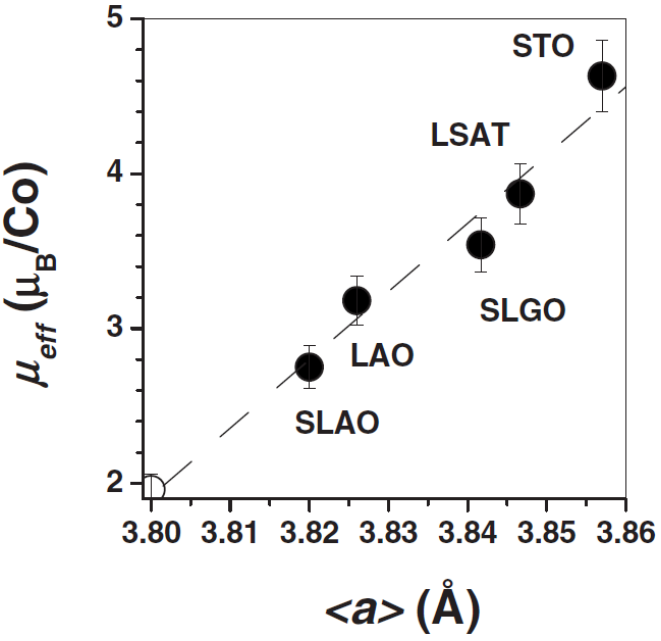

Figure 5.8 The effective paramagnetic moment μ_{eff} of LCO films as a function of the mean lattice parameter $< a >$ (closed symbols) taken from ref. [112]. The data points are labeled with the names of the corresponding substrates. The bulk value of LCO is displayed by the open symbol. The dashed line is a linear fit to the data points.

Another thing that is clear from the magnetization versus temperature data for LCO is that LCO/LAO is magnetic though it is not clear whether or not it is ferromagnetic. The gradual reduction of magnetization with temperature and no definitive T_C is not uncommon for magnetic clusters due to some impurity or defect, like that observed in spin glass.[123,124,125] In this case, localized magnetic clusters are perhaps better examined with a technique sensitive to local magnetization such as magnetic force microscopy.

If we examine hysteresis loops of $LaCoO_3$ films deposited on LAO and LSAT substrates shown in fig. 5.9 we get the impression that they are ferromagnetic.

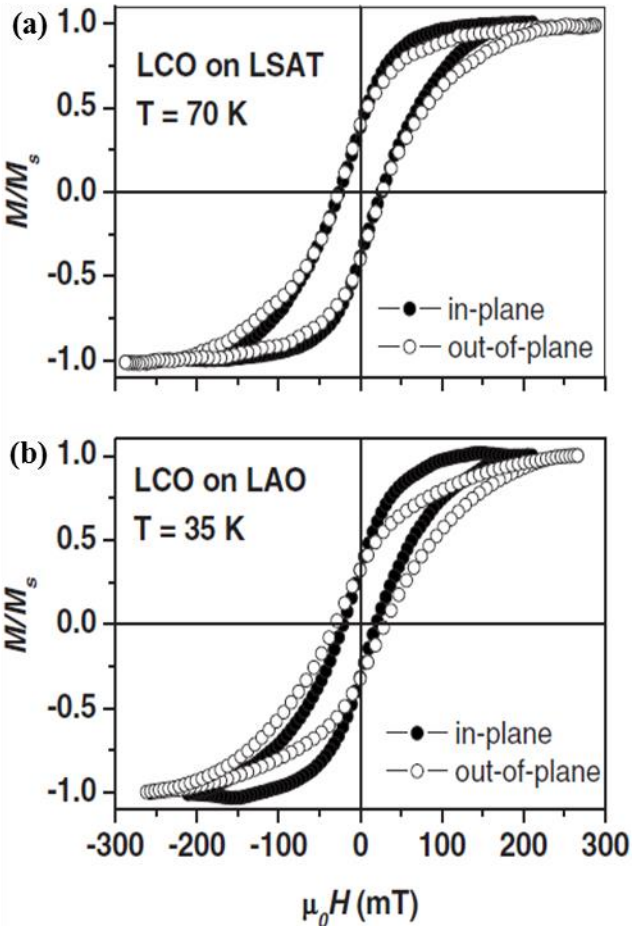

Figure 5.9 In-plane and out-of-plane magnetization reversal loops from ref. [112] normalized to the saturated magnetization M_s for LCO films on (a) LSAT and (b) LAO at $T/T_C \approx 0.8$.

5.2.2 Local Measurement

5.2.2.1 Magnetic Force Microscopy

To date, only one previous study has attempted to directly image magnetic domains in strained $LaCoO_3$ thin films using magnetic force microscopy.[126] $LaCoO_3$ thin films, 60 unit cells (~20 nm) thick, were deposited on $SrTiO_3$ (001) and $LaAlO_3$ (001) substrates using pulsed laser deposition (PLD). This study intended to contrast the effect on the local magnetic properties of these films due to bi-axial tensile and compressive strain provided by the lattice mismatch of STO and LAO, respectively.

The temperature dependence of the normalized local magnetic contrast change in MFM, shown in fig. 5.10(a), resembles that of other magnetization data presented in the previous section. The LCO film on STO is ferromagnetic with a $T_C \sim 80$ K and results for the LCO film on LAO are somewhat ambiguous but the magnetization drops before 100 K. That the properties of ferromagnetic domains on the surface of strained LCO thin films scale like bulk magnetization data confirms that ferromagnetism in strained LCO films is a bulk phenomenon and not limited to surfaces. However, it may be appropriate here to question at what thickness an LCO thin film develops characteristics consistent with bulk LCO, which really is a question of the critical thickness of LCO thin films where strain is either sufficiently buried or relaxed. Ref. [100] notes strain-influenced magnetic character in strained LCO thin films hundreds of nanometers thick. Fuchs et al.[119] and V. Mehta et al.[127] find that the thickness at which strain relaxes depends upon growth parameters and the presence of defects.

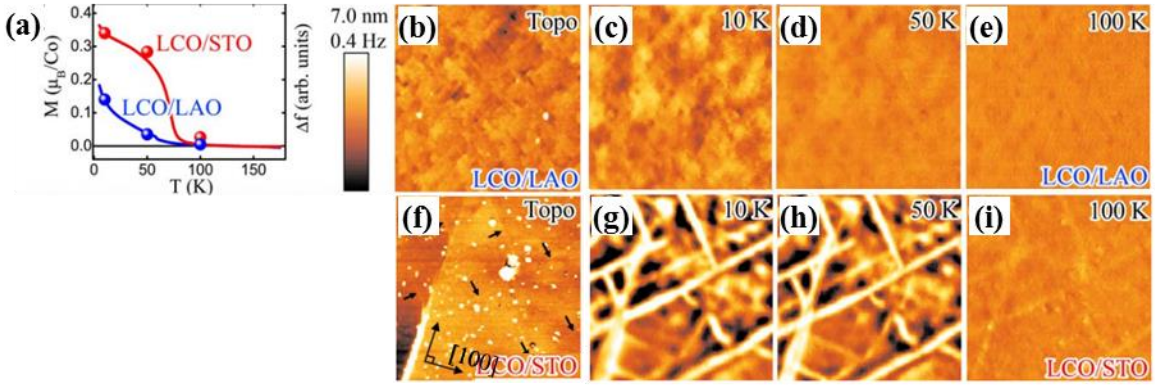

Figure 5.10 Temperature dependence of magnetization and MFM contrast of LCO films on LAO (blue) and STO (red) substrates from ref. [126]. A magnetic field of strength $\mu_0 H$=0.1T was applied during magnetization measurements. Topographic images of (b) LCO/LAO and (f) LCO/STO and MFM images of [(c)–(e)] LCO/LAO and [(g)–(h)] LCO/STO were taken during warming in an applied magnetic field of strength $\mu_0 H$=2.0T at the same location, respectively. The scan size is ~2×2 μm^2 for LCO/LAO and ~3×3 μm^2 for LCO/STO. The color scale range is 7 nm (0.4 Hz) for topography (MFM).

Weak line contrast above T_C in the LCO film deposited on STO and cluster contrast at 100 K in LCO on LAO indicates a magnetic susceptibility difference between the lines/clusters and the surrounding regions. The authors were able to verify this magnetic susceptibility difference beyond the ferromagnetic phase by noting a loss of contrast after removing the external magnetic field (reported in Park et al. but not shown). The line contrast in the MFM images of LCO/STO coincides with visible lines in the topography that are aligned with crystallographic directions in the film. Similar crosshatch patterns have been observed in manganite, ruthenates and heteroepitaxial semiconductors and, at least in the case of crosshatch in manganites, strain relaxation at grain boundaries and internal dislocations are correlated with crosshatching.[128] Because strain or rather strain relaxation is presumed to have produced the local magnetic

characteristics of these lines observed in LCO/STO, distinct in their magnetic character from that of the surrounding regions, strain does indeed play a role in magnetism in tensile-strained LCO on STO. For the LCO thin films featured in this study, the roles of chemical inhomogeneity and strain cannot be disentangled in their influence on local magnetic characteristics in strained LCO thin films.

The local chemical inhomogeneity and strain relaxation along twin domain boundaries and misfit dislocations revealed in these films would normally be overlooked using global diffraction and magnetometry measurements. Given the magnetometry and X-ray diffraction results previously published that are consistent with those published by Park et al., it seems that local measurement is essential to establish whether magnetism in strained LCO thin films are driven by defects and/or strain.

Moreover, the formation of other lanthanum cobalt oxide phases due to local variation in oxygen might also be overlooked in structural analysis techniques due to averaging.

5.2.2.2 Scanning Transmission Electron Microscopy

A number of intriguing results from transmission electron microscopy (TEM) studies have emerged since the atomic scale imaging and spectroscopic analysis of nanodomains in $La_{0.5}Sr_{0.5}CoO_{3-\delta}$ (LSCO).[129] In TEM high-angle forward scattering of energetic electrons against atomic nuclei in a thin, optically transparent material provide a contrast sensitive to the nuclear charge. Thus, this technique reveals the positions of columns of large atoms, in this case La, Sr, and Co cations, in the material with sub-angstrom resolution though it is not very sensitive to smaller atoms, like oxygen. The effects of oxygen or oxygen deficiency in crystalline oxides are often observed in relation

to their influence on the cation positions and brightness. In conjunction with TEM electron energy loss spectroscopy (EELS) is often employed to look at characteristic spectra of constituent atoms. Using EELS, changes in oxygen spectra can be used to infer causes for changes in the local characteristics of cations. Scanning TEM (STEM) data overlaid with EELS data for LSCO deposited on a $NdGaO_3$ substrate is given in fig. 5.11. In LSCO, ordered planes of O vacancies linked to the release of epitaxial strain were demonstrated to produce spin-state superlattices due to the modulation of the Co spin state in response to proximal vacancies. Interestingly, the valence of the Co ions was fairly uniform across oxygen-deficient planes and close to 2+. Notably this is a phenomenon observed in thin films of LSCO and is not observed in bulk.

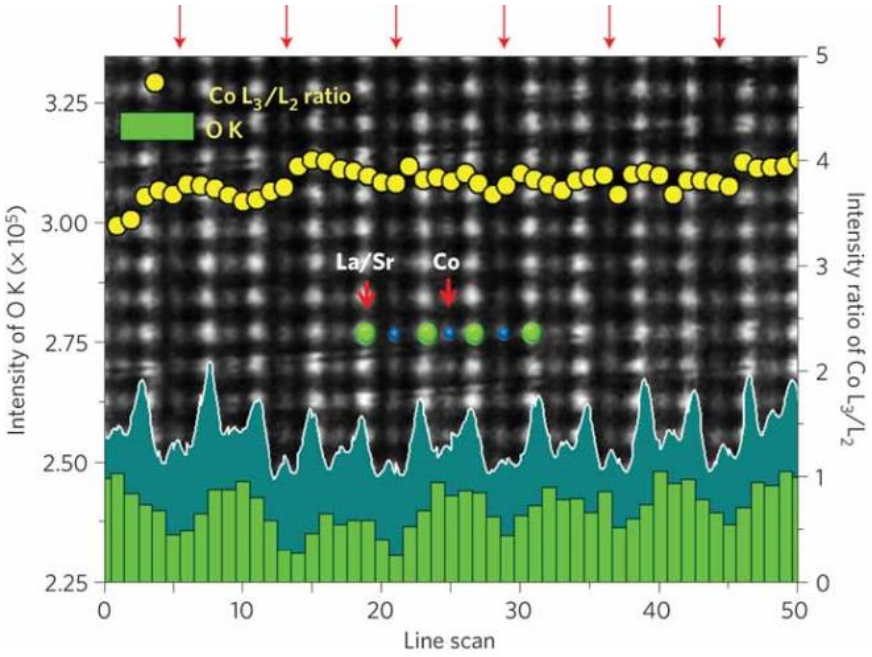

Figure 5.11 A representative STEM–EELS result for the bulk region of a (110)-oriented LSCO film grown on an $NdGaO_3$ substrate taken from ref. [130]. The alternating dark contrast (marked by red arrows) in every other Co–O plane results from the structural relaxation due to oxygen vacancy ordering in the planes (green bar graph shows O K edge intensity oscillation); an intensity modulation can also be seen in the overlaid line trace of the ADF signal (teal graph). The Co L_3/L_2 ratio (yellow circles) do not show significant modulations.

Local density of states calculations with density functional theory further indicated that the planes of oxygen vacancies accompanied a high-spin configuration of Co in LSCO with three spin-down channels mostly empty. Further investigation confirmed the stabilization of a brownmillerite structure in LSCO via the ordering of oxygen vacancies.[130]

Recently similar modulation in STEM contrast has been observed in $LaCoO_3$ on LAO, LSAT, and STO substrates (see fig. 5.12).[131] This modulation is apparently sensitive to strain. Due to XAS and ellipsometry measurements, the authors concluded

that Co^{2+} concentration is less than 5%, leading them to conclude that the modulation is not a result of nonstoichiometry and oxygen vacancy ordering. XAS and ellipsometry measurements, though sensitive to stoichiometry, are again non-local.

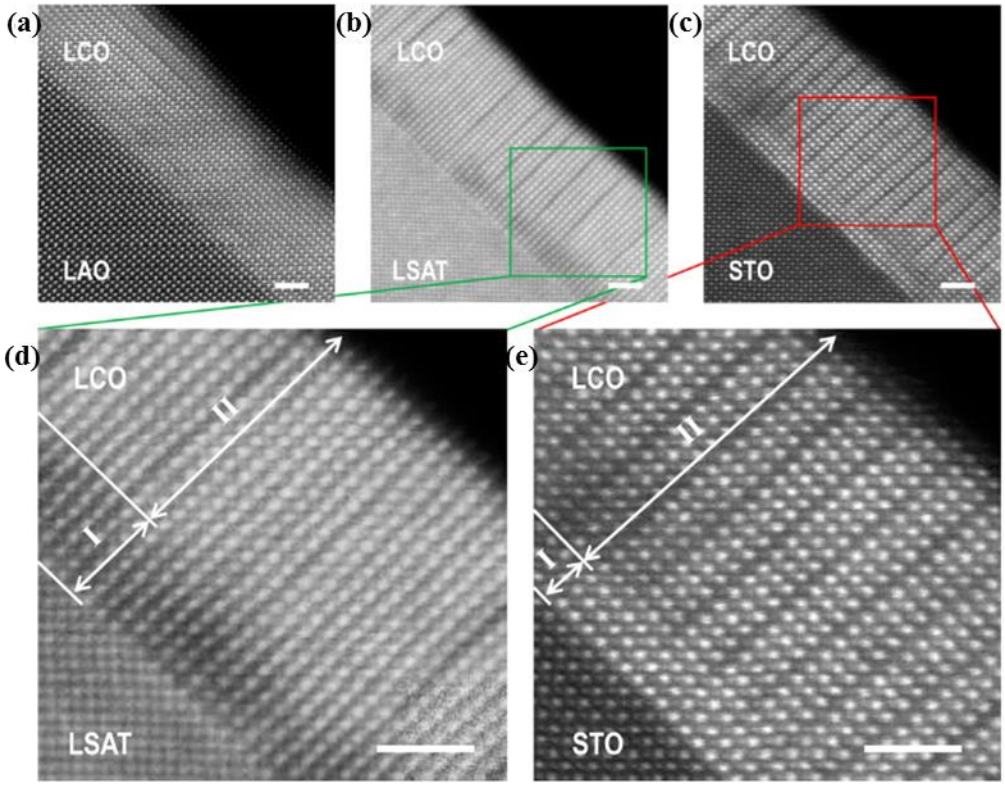

Figure 5.12 Microstructure and strain dependent lattice modulations from ref. [131]. *Z*-contrast STEM images for LCO films grown on (a) LAO, (b) LSAT, and (c) STO. For LCO grown on LAO, only a few horizontal dark stripes are observed as in (a). As the tensile strain is applied, vertical dark stripes start to appear as in (b). When more tensile strain is applied, the vertical dark stripes become regular with a $3a_0$ periodicity as in (c). Two distinct regions observed in LCO films grown on (d) LSAT and (e) STO. Region I corresponds to the "uniform region" without any dark stripes. Region II corresponds to the "atomic ordering region" with the dark stripes. The LCO film on STO has a thinner uniform region I as compared to the film on LSAT due to a larger mismatch. The scale bars correspond to 2 nm.

Bi$\check{s}$kup et al.[132] challenge this claim and based on local STEM and EELS measurements conclude that high-spin Co^{2+} states are antiferromagnetically aligned in the oxygen-depleted planes and ferromagnetically ordered in the stoichiometric planes. This suggests that ferromagnetism in tensile-strained films of LCO is vacancy-mediated and strain-enhanced rather than supporting a model of strain-induced promotion of Co^{3+} states from low spin to high spin.

An important point to address here is the possibility that the high-energy electron beam used in STEM can produce vacancies. The incident power on a given area of imaging under TEM depends on the dose rate and beam voltage. The dose rate refers to the number of electrons per area per unit time. Dark smudges (reminiscent of those in fig. 5.12(b) and 5.12(c)) due to beam damage can indicate upwards of 10% depthwise variation in stoichiometry.[133] Williams and Carter[134] indicates that an 80 kV electron beam such as the one used in the STEM study in ref. [131] can transfer 12.5 eV to oxygen. With oxygen vacancy formation energy in $LaCoO_3$ on the order of a few eV[135] the effect of the electron beam cannot be disregarded.

5.3 EXPERIMENTAL RESULTS FOR $LaCoO_3$ THIN FILMS

Our investigation of the effect of different strain states on $LaCoO_3$ began with deposition of $LaCoO_3$ thin films on $LaAlO_3$ and $SrTiO_3$ substrates using molecular beam epitaxy to enable comparisons with previously reported results for strained LCO thin films deposited using pulsed laser deposition. In situ monitoring during deposition was conducted using RHEED and the global structural, compositional and magnetic properties of the films were subsequently measured using XRD, XPS and SQUID magnetometry, respectively. Then the local magnetic characteristics of the films were

investigated using MFM. As such, this section will be organized so that exemplary RHEED, XRD and XPS data for $LaCoO_3$ on $SrTiO_3$-buffered Si will be presented first, SQUID data obtained for all samples will follow and then MFM data will be presented on a sample-by-sample basis. The RHEED, XRD, XPS and SQUID data for $LaCoO_3/SrTiO_3/Si(100)$ have already been published and are featured in ref.'s [105]* and [136]†.

Concurrent to this study, extensive efforts were invested in integrating functional oxide materials with silicon using virtual substrates. Initial progress was made with regards to deposition of $SrTiO_3$ on silicon.[137] Previous work indicated that functional oxide integration of $BaTiO_3$ on $SrTiO_3/Si$ stacks was also a possibility.[138] It was a logical progression to merge design objectives by incorporating $LaCoO_3$ thin films into $SrTiO_3/Si$ and $BaTiO_3/SrTiO_3/Si$ stacks both for strain studies and to probe tensile strain values which had not been previously investigated and to extend the range of functional oxide heterostructures integrated with silicon. Thus, $LaCoO_3$ thin films were deposited using MBE on commercial $LaAlO_3$ and $SrTiO_3$ substrates, on a virtual substrate comprised of a $SrTiO_3$ layer deposited on Si(100), and on a $BaTiO_3$ buffer layer deposited on an $SrTiO_3/Si(100)$ virtual substrate.

---

* For ref. 105 A. Posadas, M. Berg, H. Seo, D.J. Smith, A.P. Kirk, D. Zhernokletov, R.M. Wallace, A. de Lozanne, A. A. Demkov, Microelectron. Eng., 88(7), 1444 (2011), A. A. D. conceived the project; A. P. and M. B. grew samples; H. S. performed and interpreted DFT calculations; D. J. S. provided TEM measurements; A. P. K., D. Z., and R. M. W. provided XPS measurements and analysis; A.P. performed RHEED and XRD experiments, interpreted the results, and authored the manuscript.

† For ref. 136 A. Posadas, M. Berg, H. Seo, A. de Lozanne, A. A. Demkov, D. J. Smith, A. P. Kirk, D. Zhernokletov, R. M. Wallace, Appl. Phys. Lett., 98, 053104 (2011) , A. A. D. conceived the project; A. P. and M. B. grew samples; H. S. performed and interpreted DFT calculations; D. J. S. provided TEM measurements; A. P. K., D. Z., and R. M. W. provided XPS measurements and analysis; M. B. performed the SQUID measurements and SQUID data analysis; and A.P. performed XRD experiments and XRD data analysis, interpreted the results, and authored the manuscript.

5.3.1 RHEED Monitoring of MBE Deposition

The method for deposition of the $SrTiO_3$ layer on Si(100) for subsequent deposition of $LaCoO_3$ and for additional buffer layers, as is the case of the $BaTiO_3$ on STO/Si(100), is as follows. National Semiconductor epi-grade silicon (100) wafers are pre-cleaned by exposing them to UV/ozone for 15 min prior to loading them in the DCA 600 molecular beam epitaxy system. The Si(100) substrate is further prepared by desorbing SiO_2 from the wafer surface at 775°C, after which the wafer is cooled to 600°C and the clean Si(100) surface is exposed to half of a monolayer of Sr metal. Sr-passivation of the Si(100) surface induces a surface reconstruction that serves as a template for deposition of the initial $SrTiO_3$ (STO) layer.[139] After the Sr-passivation of the Si(100) surface, the wafer is cooled to 200°C prior to the deposition of $SrTiO_3$. Sr and Ti are initially co-deposited in a background oxygen pressure of 1×10^{-7} Torr up to deposition of two unit cells of $SrTiO_3$, then the oxygen pressure was increased to 7×10^{-7} Torr until another two unit cells were deposited, up to a total of 4 unit cells. The amorphous template STO layer was crystallized by an annealing treatment at 550°C (see fig. 5.13(a) and 5.13(b)) after which additional layers of STO were deposited at 550°C in a background oxygen pressure of 1×10^{-7} Torr. This procedure resulted in a $SrTiO_3$ buffer layer 15 unit cells thick on Si(100). The thermal expansion of the $SrTiO_3$ and Si layers are decoupled by forming an 80 Å-thick layer of SiO_2 between the layers by exposing the $SrTiO_3$/Si stack to oxygen at 650°C for 30 min with a background oxygen pressure of 1×10^{-5} Torr (see fig. 5.13(e) and 5.13(f)). RHEED is used to monitor surface reflections to confirm the characteristic 2 × 1 reflection pattern of a clean Si(100) surface after SiO_2 desorption[140] and to monitor the crystallinity of the $SrTiO_3$ layer during the various deposition steps.

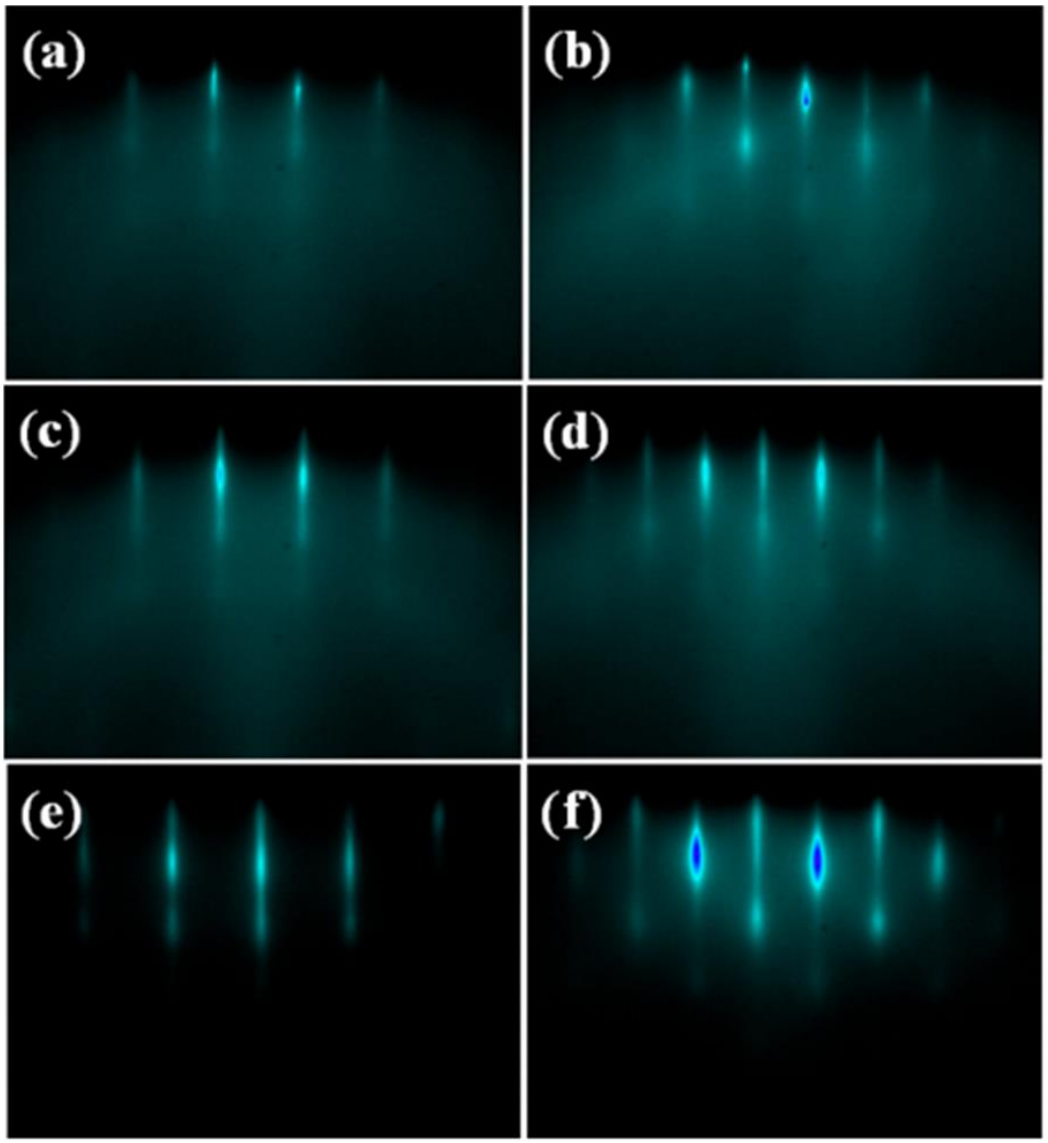

Figure 5.13 RHEED patterns after each growth step of $SrTiO_3$ on silicon, taken along the (a, c, e) <010> and (b, d, f) <110> directions. (a) and (b) were taken after the initial amorphous $SrTiO_3$ layer was crystallized. (c) and (d) were taken after the main $SrTiO_3$ layer was deposited and (e) and (f) were taken after a post-deposition anneal in oxygen at 650 °C.

For deposition of an additional buffer layer of $BaTiO_3$, the STO/Si(001) virtual substrate is transferred in-situ to an atomic layer deposition (ALD) chamber for chemical deposition of $BaTiO_3$. $BaTiO_3$ films were grown using barium bis(triisopropylcyclopentadienyl) and titanium tetraisopropoxide as metal precursors, and water as an oxidant. The film is grown by alternating dosing cycles where each metal precursor is introduced in a pulse sequence followed by dosing and purging sequences of water and ultrahigh purity argon gas, respectively. The composition is determined by the ratio of cycles where one metal precursor is pulsed versus another.

During growth the substrate temperature was maintained at 225°C, while a background pressure of ultrahigh purity argon gas was maintained at 1 Torr. The film composition is verified within 5% using in-situ X-ray photoelectron spectroscopy (XPS), where a commercial single-crystal $BaTiO_3$ substrate is used as a standard to determine the Ba:Ti ratio of ALD-grown $BaTiO_3$ films. Details regarding the growth technique and ALD system are provided in ref. [141].

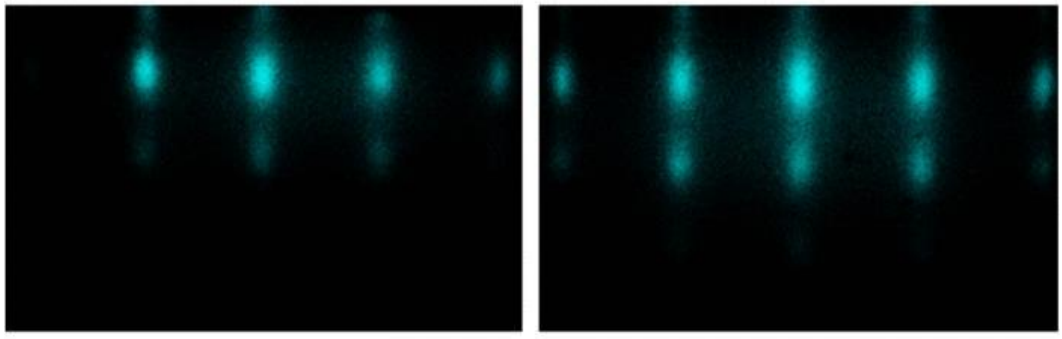

Figure 5.14 RHEED patterns from ref. [141] of a 7 nm BTO film on four-unit-cell STO-buffered Si(001) as-deposited (left) and after 5 minutes of vacuum annealing at 600 °C (right). Both images are taken along ⟨110⟩ direction of STO.

The fluxes of lanthanum from an effusion cell and cobalt from an electron beam evaporator were calibrated and then co-deposited at a rate of ~2 monolayers per minute onto the substrate until the desired thickness of a $LaCoO_3$ thin film has been deposited. The sample was cooled at 10°C per minute to room temperature in atomic oxygen maintained at a background pressure of 1×10^{-5} Torr. Film growth is monitored in situ using RHEED to confirm the crystallinity of the film and that the LCO thin film is epitaxially strained to the substrate.

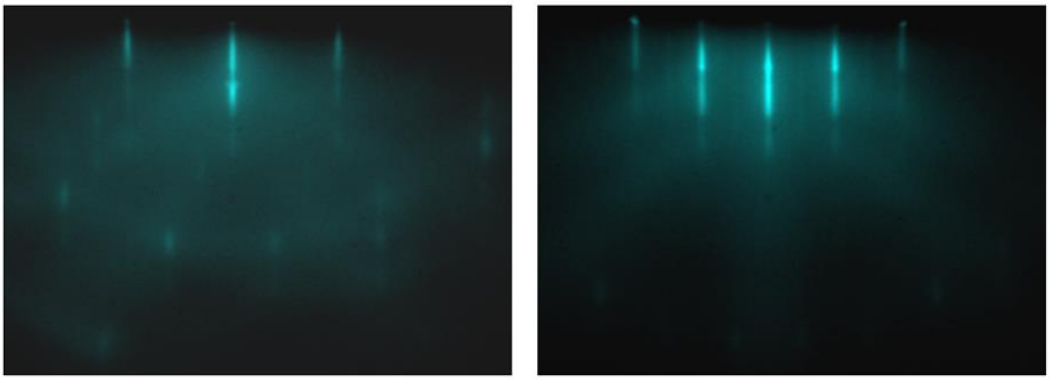

Figure 5.15 RHEED patterns of a 25 nm $LaCoO_3$ film grown on STO-buffered Si(001) as-deposited. The left image was taken along the <210>direction and the right image was taken along the <110> direction.

5.3.2 X-ray Characterization

After growth, X-ray diffraction was used to determine lattice constants and overall crystalline quality of the LCO thin films. A symmetric 2θ-θ scan of a 40 nm film on STO-buffered Si(100) (fig. 5.16(a)) shows only peaks from the silicon substrate and the 00l crystal planes of the $LaCoO_3$ film. A close-up of the region $44° < 2\theta < 52°$ in the vicinity of the 002 film peak (fig. 5.16(b)) reveals a c-axis lattice constant of 3.78 Å for $LaCoO_3$ and 3.89 Å for $SrTiO_3$. An asymmetric $2\theta-\theta$ scan with the offset angle ψ set to

cut across the (103) Bragg reflection (fig. 5.16(c)) indicates an in-plane lattice constant of 3.89 Å for $LaCoO_3$ which is identical to that of the $SrTiO_3$ buffer layer. In addition, a cross-sectional TEM micrograph of the stack (inset of fig. 5.16(a)) verifies that the $LaCoO_3$ film is epitaxially strained to the $SrTiO_3$ buffer layer and attests the structural quality of the film, buffer layer and substrate.

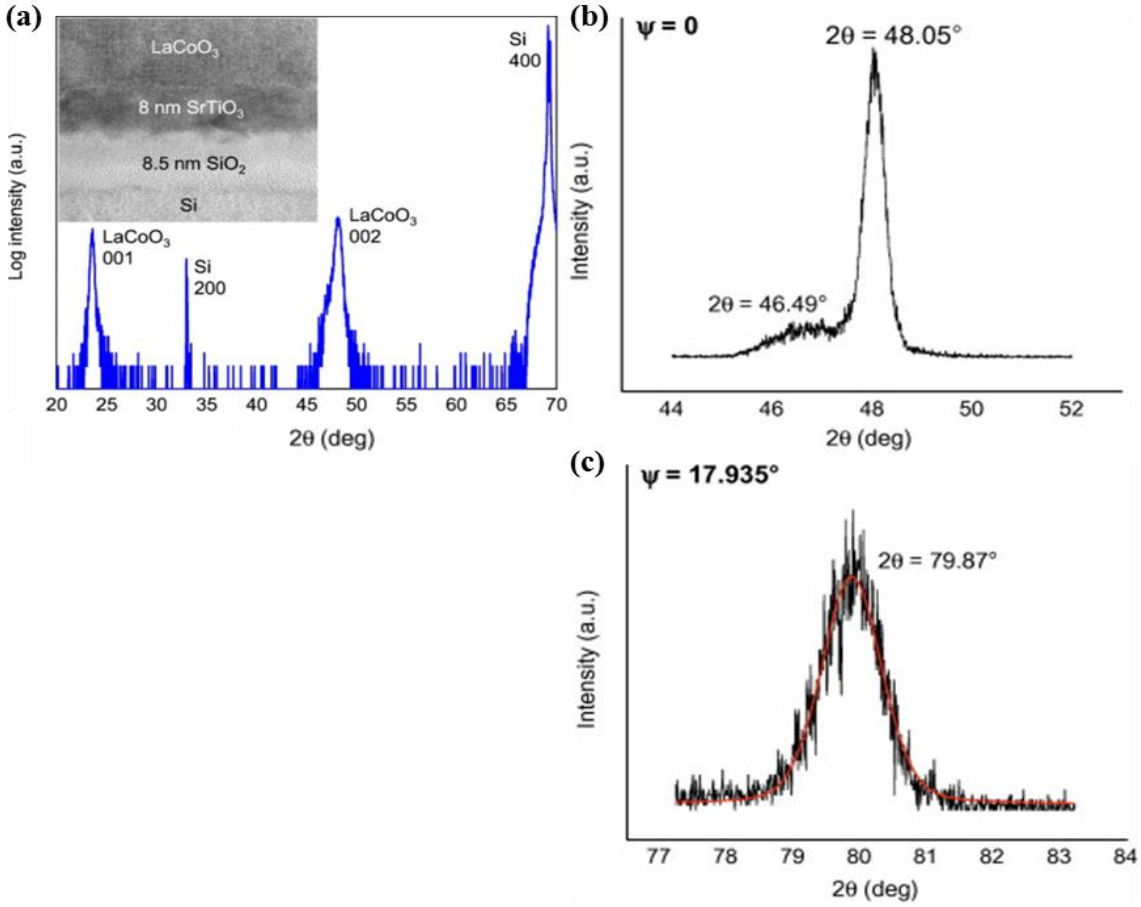

Figure 5.16 (a) XRD 2θ-θ scan of $LaCoO_3$ on $SrTiO_3$-buffered Si(100) from ref. [136]. The inset shows a high-resolution cross-sectional TEM micrograph of the LaCoO3 on $SrTiO_3$-buffered Si(100) stack with the different layers labeled. (b) Close-up of XRD data showing the (002) Bragg reflections of $LaCoO_3$ and $SrTiO_3$. (c) An asymmetric scan at a tilt angle of 17.94° of the (103) Bragg reflection of $LaCoO_3$. (b) and (c) are featured in ref. [105].

X-ray photoelectron spectroscopy (XPS) was also employed *ex situ* to verify that the lanthanum, cobalt, and oxygen spectra in the $LaCoO_3$ layer were consistent with spectra from $LaCoO_3$ single crystal samples, and there was no detectable Co metal in the thin film. XPS measurements were performed using a Kratos AXIS Ultra DLD utilizing a monochromated Al-Kα X-ray source (hν = 1486.5 eV), hybrid optics, and a multi-channel plate and delay line detector coupled to a hemispherical analyzer. The take-off angle of the photoelectrons with respect to the X-ray beam was 45°. Spectra for Co 2*p*, La 3*d*, O 1*s*, and C 1*s* were recorded using a single sweep and an aperture slot of 300 × 700 μm and pass energy of 20 eV. The measurements were repeated after a short Ar sputtering procedure using 4-keV Ar+ ions for 15 seconds with a 75 μA extraction current, which is confirmed to eliminate adventitious surface carbon contamination based on the C 1s signal. The current at the sample during the sputtering was 1.6 μA.

The XPS results are presented fig. 5.17. The absence of a signal at 778 eV in the Co 2*p* spectrum indicates that the presence of free Co metal in the sample is below the detection limits.[142] There is a 0.7 eV shift in the Co 2*p* spectrum towards higher binding energy after sputtering. This is consistent with previously reported spectra for single crystal $LaCoO_3$.[143] The energy shift after sputtering may suggest that the valency of surface Co ions is reduced from 3+ to 2+ due to surface oxygen depletion. The La 3*d* spectrum is consistent with a La^{3+} signal in the presence of an oxygen environment. The strong satellite peaks at higher binding energy can be attributed to a multielectron "shake up" process[144], and are clearly correlated with an oxidized La species. The O 1*s* spectrum after sputtering features a 0.4 eV shift to higher binding energy of the peak at 529.9 eV and a significant reduction in the intensity of the secondary oxygen peak at 532.2 eV. The peak at 529.9 eV is consistent with lattice oxygen in a perovskite, while the secondary

oxygen peak likely indicates the presence of surface hydroxyl groups[145] that have not been completely removed in the sputtering process.

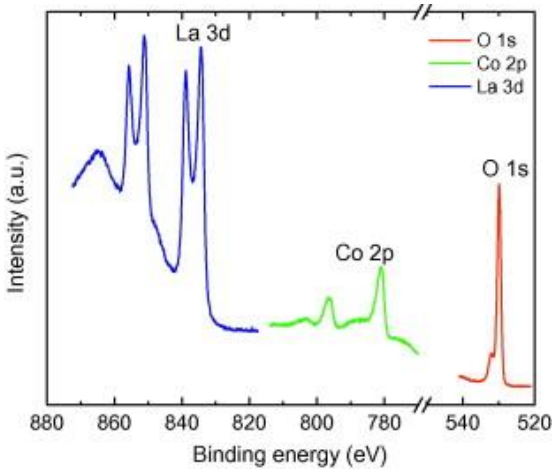

Figure 5.17 XPS spectra of $LaCoO_3$ after Ar sputtering from ref. [105]. Spectra for the Co 2*p*, La 3*d*, and O 1*s* are shown.

5.3.3 SQUID Magnetometry Data

For all thin film samples grown, SQUID magnetometry measurements were performed to verify the global magnetic characteristics of our LCO samples. Determination of the magnetic moment of LCO thin films as they vary with applied field and temperature requires precisely measuring the magnetic contribution of the substrate and background subtraction of that contribution from the data. The substrate contribution was not measured for most of the samples presented here and thus direct comparisons of the magnitude of the magnetic moment of and susceptibility calculations for the LCO thin film samples are not advisable. Thus, comments on SQUID results here will refer to measurements of the magnetic moment normalized for applied field and volume in the

case of magnetization versus temperature graphs and the magnetic moment normalized per cobalt atom and in the case of magnetization versus applied magnetic field graphs.

A comparison of the normalized magnetic moment in varying temperature and applied magnetic field for LCO films deposited on LAO, STO and STO-buffered Si(100) is given in fig. 5.18. It is clear that films deposited on STO exhibit a ferromagnetic-paramagnetic transition but is less obvious in the case of LCO deposited on LAO. The linear increase of magnetization below T_C of the LCO film on STO-buffered Si(100) likely reflects that the substrate or film or both are not completely saturated and moments progressively align with the field as the temperature decreases below T_C. All samples exhibit some degree of magnetic hysteresis. As with the data presented in ref.'s [104] and [112], the lack of a definitive T_C and the presence of a hysteresis loop in addition to the inability of the film to saturate may indicate glassy behavior.

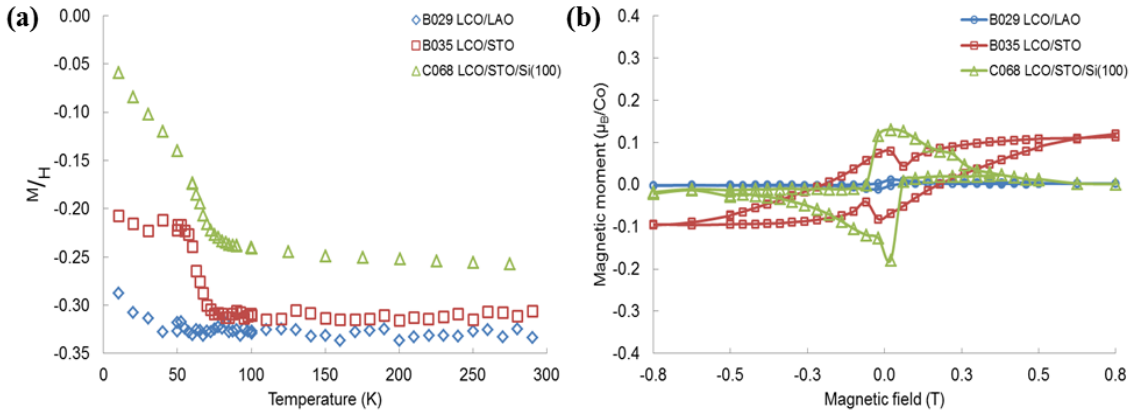

Figure 5.18 Variation of the normalized magnetic moment of $LaCoO_3$ thin films deposited on $LaAlO_3$, $SrTiO_3$ and $SrTiO_3$-buffered Si(100) substrates with (a) temperature and (b) applied magnetic field. The normalized magnetic moment versus temperature data are presented for field cooled samples; zero-field cooled data is not included in this figure.

Further comparison of magnetization versus applied field profiles for $LaCoO_3$ thin films deposited on LAO substrates as shown in fig. 5.19 confirms ferromagnetic character to a degree. Peaks in the data occur at ± 0.02 T for both LCO films on LAO substrates. An additional peak occurs at ±0.067 T in the magnetization versus applied field profile for the 40 nm LCO film shown in fig. 5.19(b).

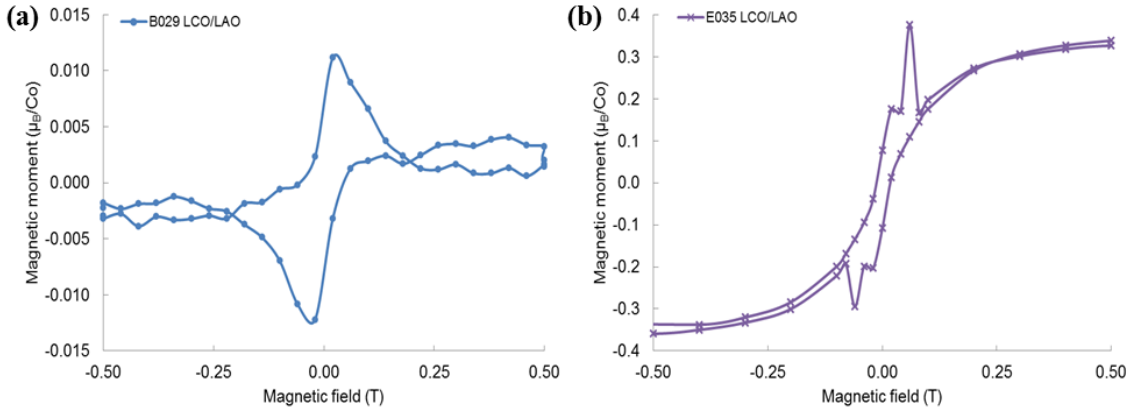

Figure 5.19 Variation of the normalized magnetic moment with applied magnetic field for a (a) 25 nm and (b) 40 nm LaCoO3 thin film deposited on $LaAlO_3$.

Point fluctuations in the magnetization versus applied magnetic field profiles (fig. 5.20) can occur due to substrate contributions. The linear diamagnetic background at high applied magnetic fields is subtracted from the data to remove substrate contributions but any non-linearity in the response of the substrate at low fields is not accounted for and thus cannot be ruled out as a contributing factor unless the entire substrate contribution is measured and removed. If the peaks at ±0.02 T can be attributed to substrate contributions, peaks for films grown on the same substrate material are expected to occur at the same field values. This would be a likely explanation for the presence of the peaks at ±0.02 T for both films grown on $LaAlO_3$.

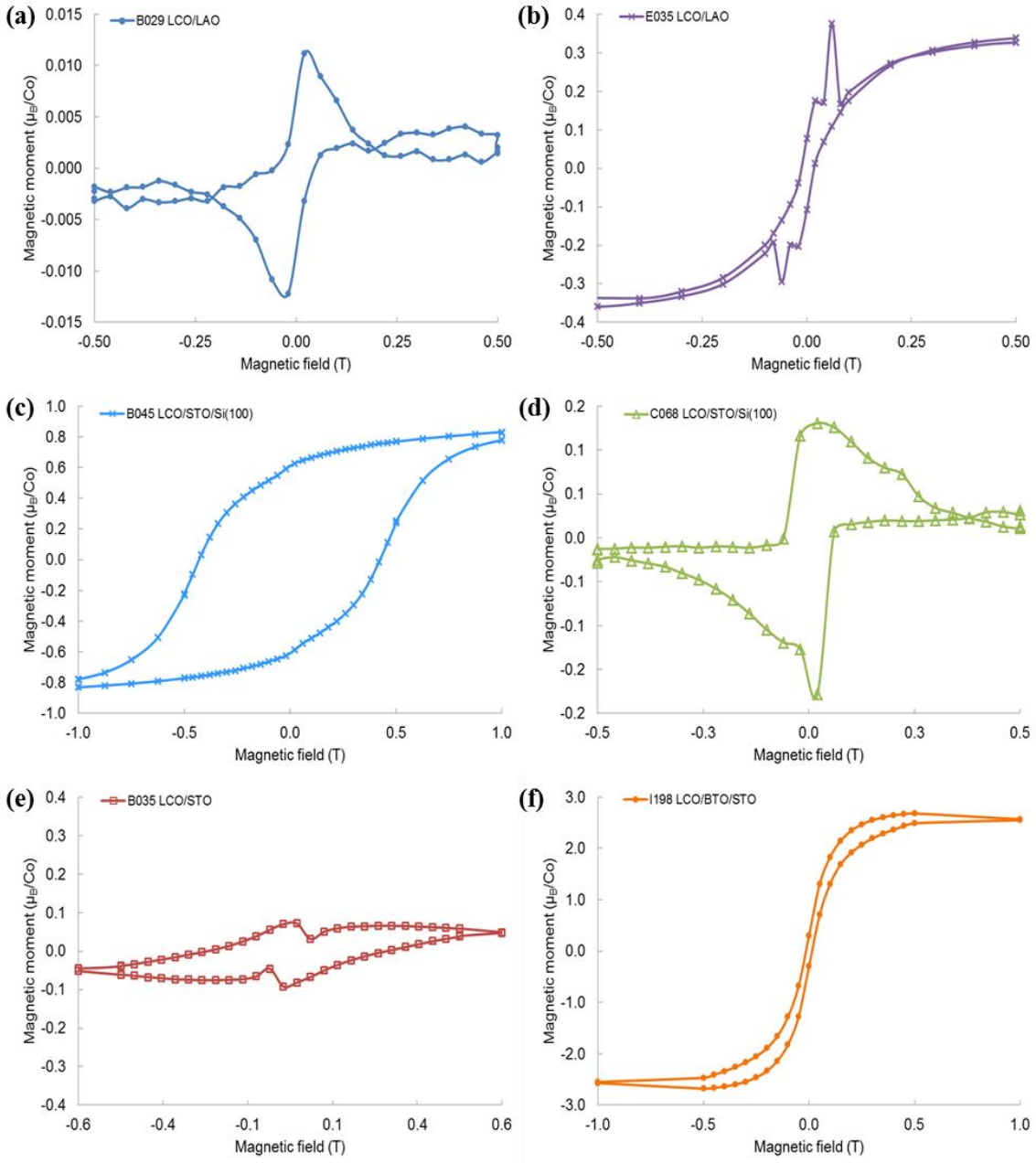

Figure 5.20 Variation of the normalized magnetic moment with applied magnetic field for a (a) 25 nm and (b) 40 nm $LaCoO_3$ thin film deposited on $LaAlO_3$, a (c) 40 nm and (d) 25 nm $LaCoO_3$ thin film deposited on $SrTiO_3$-buffered Si(100), a (e) 28 nm $LaCoO_3$ thin film deposited on $SrTiO_3$, and a (f) 20 nm $LaCoO_3$ thin film deposited on $BaTiO_3$-buffered $SrTiO_3$.

However, magnetization versus applied field profiles for $LaCoO_3$ thin films deposited on other substrates, shown in fig. 5.20, also have peaks at ±0.02 T with the exception of $LaCoO_3$ on $BaTiO_3$-buffered $SrTiO_3$. This peak may be an intrinsic feature of LCO thin films. The absence of peaks at ±0.02 T in $LaCoO_3$ on $BaTiO_3$-buffered $SrTiO_3$ indicate that the peaks for films on other substrates is not an artifact of the SQUID measurement which is performed in more or less the same manner for each sample. It is important to note that the raw data for these samples is on the order of 10^{-6}-10^{-5} emu, roughly equivalent to measuring a single flux quantum across the Josephson tunneling junction employed in the SQUID. SQUID measurements at this order of magnitude are susceptible to noise which brings the source of point fluctuations into question.

In the case of LCO on LAO and for one sample of LCO grown on STO-buffered Si (100) the peak values of magnetization exceed those of the saturation magnetization. If this is not an artifact of the SQUID measurement, it may indicate competing anisotropies in LCO. Because the slope of the magnetization curve with field in the raw data was different between saturation and low fields for a sample of LCO on STO-buffered Si (100) (fig. Figure 5.18(b) and fig. Figure 5.20(d)) and LCO on STO (fig. Figure 5.18(b) and fig. Figure 5.20(e)) the linear dependence at low fields was subtracted for these samples and hysteresis in the low field regime was highlighted here. Again if this is not an artifact introduced by errors in measurement, this behavior indicates competing anisotropy in LCO. Further characterization of field-dependent substrate properties is necessary to investigate this unusual behavior.

For $LaCoO_3$ under tensile strain it appears that the hysteresis loop widens and then narrows with increasing tensile strain (fig. 5.21). This can indicate a relationship

between magnetic anisotropy and strain for LCO thin films, perhaps shifting the preferred axis of the film from the in-plane direction to out-of-plane, and even differentiating between substrates that are the same material but that are prepared differently. The magnetic moment per Co atom for a thin film of LCO deposited on STO-buffered Si (100) is higher than what is expected given the literature and is not consistent with Co^{3+} atoms in either a LS/IS or a LS/HS configuration.

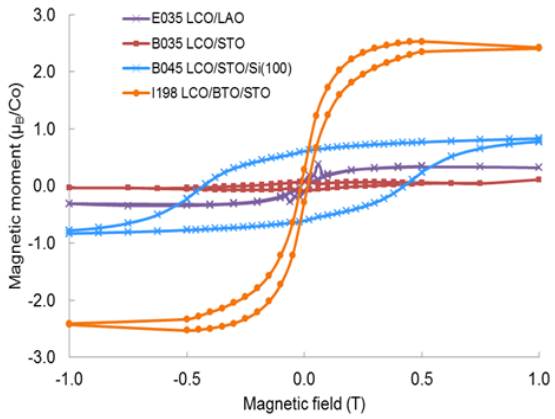

Figure 5.21 Variation of the normalized magnetic moment with applied magnetic field of $LaCoO_3$ thin films deposited $SrTiO_3$, $SrTiO_3$-buffered Si(100), and $BaTiO_3$-buffered $SrTiO_3$ substrates.

The Curie–Weiss law predicts a linear relationship between the reciprocal susceptibility and temperature in the paramagnetic region of $LaCoO_3$ films. Again, the susceptibility of these films remains unknown until the substrate contribution is background subtracted. However, the magnetic moment normalized for applied magnetic field and volume is akin to a volumetric susceptibility and we might expect the inverse normalized magnetic moment to depend linearly on temperature beyond the ferromagnetic to paramagnetic transition for these films. Data for all but one sample

confirms this linear dependence and results obtained for two samples are given as an example in fig. 5.22.

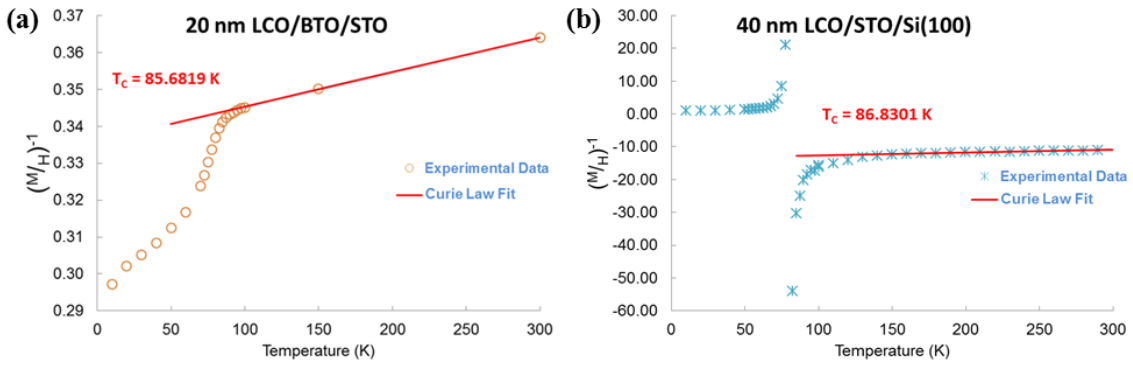

Figure 5.22 Curie–Weiss law fitting (solid red line) to the inverse normalized magnetic moment vs temperature plot for (a) 20 nm of $LaCoO_3$ deposited on a $BaTiO_3$-buffered $SrTiO_3$ substrate and (b) 40 nm of $LaCoO_3$ on a $SrTiO_3$-buffered Si(100) substrate.

In this manner estimates of the Curie temperature for all films versus the lattice mismatch of each substrate calculated from bulk values were obtained and are plotted in fig. 5.23. The 40 nm film of $LaCoO_3$ deposited on STO-buffered Si(100) has the highest T_C estimated from the temperature dependence of the inverse normalized magnetic moment, even higher than a 25 nm film deposited on STO-buffered Si(100). The 25 nm film of $LaCoO_3$ deposited on STO-buffered Si(100) has an estimated T_C very near to that of a 27 nm film deposited on a commercial STO substrate.

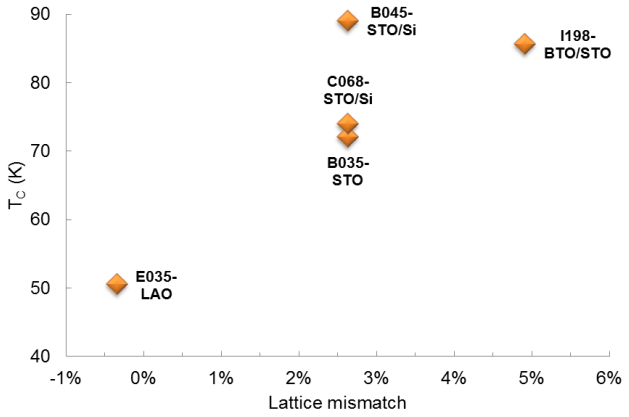

Figure 5.23 The Curie temperature T_C as a function of the lattice mismatch calculated from bulk values. The data points are labeled with the sample number and corresponding substrates.

Rather than a saturation of T_C at the limits of tensile strain, which may have been expected given previous results reported in ref. [112], the Curie temperature appears to increase with increasing in-plane tensile strain. The in-plane lattice constant of the $BaTiO_3$ buffer layer is debatable as a previous report has demonstrated that BTO layers grown on $SrTiO_3$ substrates have in-plane lattice constants that depend on the thickness of the $BaTiO_3$ layer.[146] The nominal thickness of our $BaTiO_3$ buffer layer is 12 nm.

5.3.4 Magnetic Force Microscopy

5.3.4.1 $LaCoO_3$ on STO-buffered Si(100)

A topographic image and MFM image simultaneously acquired at liquid helium temperature of the surface of a 40 nm LCO film deposited on STO-buffered Si(100) is given in fig. 5.24. The nominal thickness of the $SrTiO_3$ buffer layer is 8 nm. A bias between the tip and sample was applied to compensate for electrostatic artifacts in the

frequency shift image. There is no apparent correlation between the surface topography and MFM image.

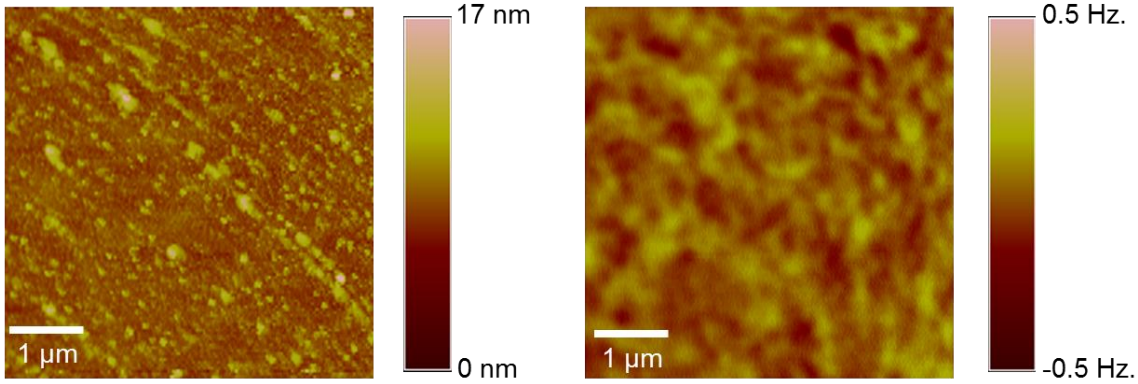

Figure 5.24 Topography image (left) and the corresponding frequency shift (right) image recorded of the same 5 x 5 μm^2 area of the surface of a 40 nm $LaCoO_3$ film on STO-buffered Si(100) at T = 4.3 K.

Fig. 5.25 shows a series of MFM images taken from T = 4.3 K to 90 K and the corresponding RMS frequency shift roughness of each MFM image. The images were acquired in the same region for both the warm-up and cool-down sequences. The color contrast of the MFM images was adjusted to highlight regions of domain rearrangement as the temperature is varied.

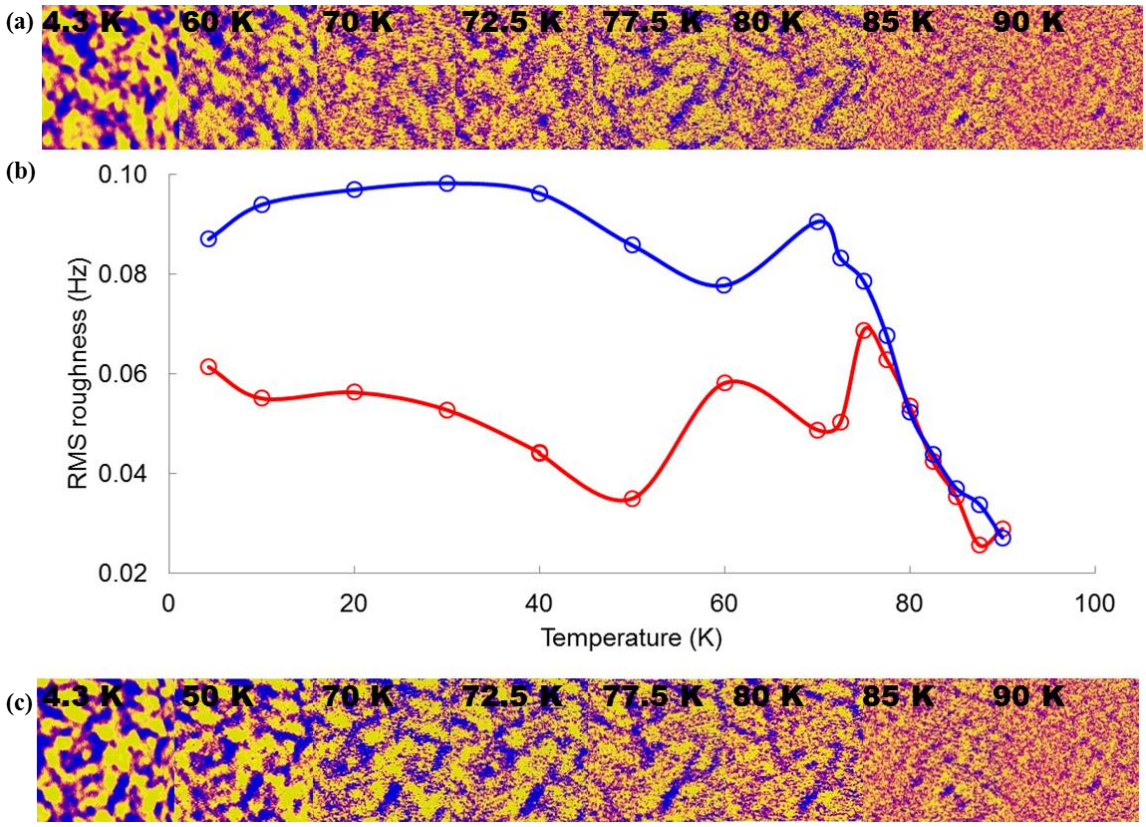

Figure 5.25 The temperature-dependent MFM image sequence (a) for warming and (c) cooling in a magnetic field H = 0.034 T directed normal to the sample surface, and the corresponding RMS frequency shift roughness values (b) of a 40 nm $LaCoO_3$ film on STO-buffered Si(100) over a thermal cycle. The red series in (b) corresponds to warming up and the blue series corresponds to cooling down. The images and corresponding frequency shift data are obtained at the same 5.4 × 5.4 μm^2 area. The frequency shift range of the MFM images is ±0.1 Hz.

The domain pattern in the MFM image changes upon warming to 75 K where stripe-like domains develop. At this temperature the orientation of some of the domains have changed likely due to the coercivity of those domains being lower than the applied field. As the film is cooled in the presence of an applied field, the stripe-like features reappear in the same locations as with warming and remnants of those features are still visible at 70 K. By 4.3 K, connected domains have broken up into smaller domains. It is

interesting to note that the domain patterns at low temperature at the beginning and end of a complete thermal cycle are not identical, that is, the process is not completely reversible.

The dissemination of streak-like features at low temperature initially appears to be contrary to those reported in ref. [126] where stripe-like domain patterns in the MFM images remain fixed and are clearly observable at low temperature. We also did not observe cross-hatch features in the surface topography. However, we did find that steak-like features can persist to low temperatures provided the sample is field cooled in a stronger magnetic field as shown in fig 5.26.

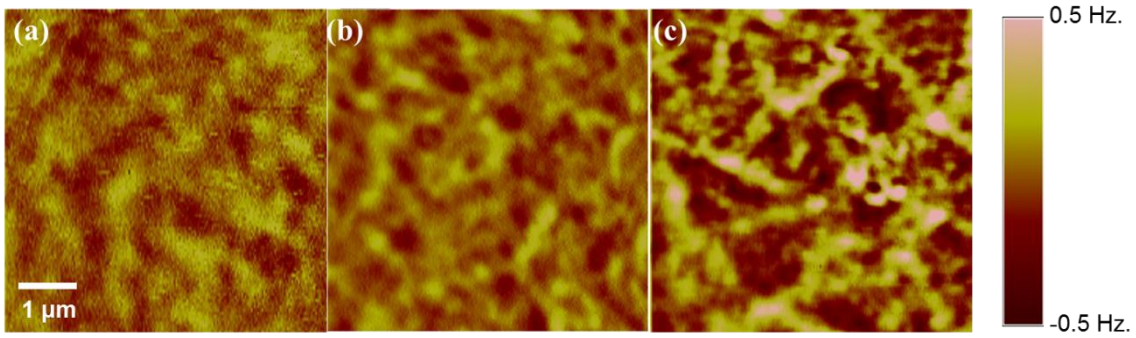

Figure 5.26 Frequency shift images of the surface of a 40 nm $LaCoO_3$ film on STO-buffered Si(100) taken at T = 4.3 K and H = 0 T after (a) zero-field cooling state and field cooling in a (b) H = 0.034 T field and (c) H = 0.4 T field. Streak-like domains are clearly discernible for the sample after field-cooling in a H = 0.4 T field.

According to the MFM data, T_C for the film is around 85 K, beyond which the contrast diminishes almost completely except for a few small, faint features. A comparison of the topography and MFM images at 90 K in fig. 5.27 reveals that these faint features in the MFM image may be due to cross-talk between the topography and

frequency shift signals. As in ref. [126] these features visible above 85 K may also indicate a susceptibility difference at that location.

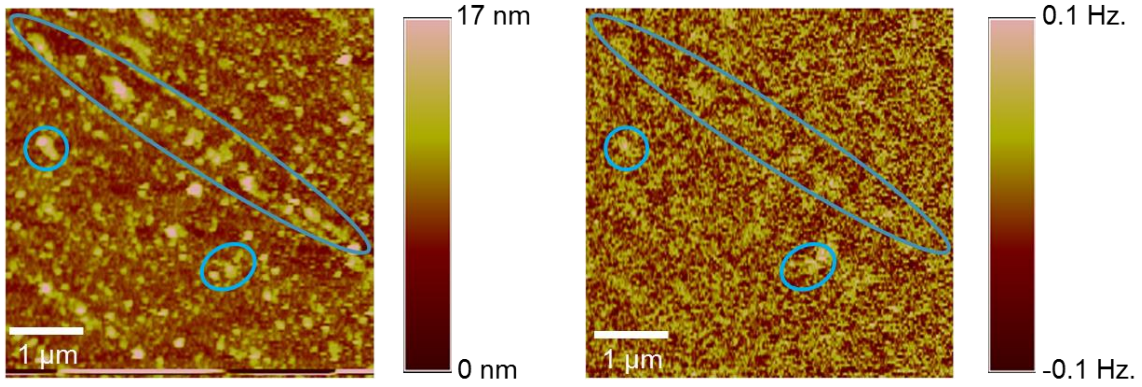

Figure 5.27 Topography image (left) and the corresponding frequency shift image (right) recorded of the same 5 x 5 μm^2 area of the surface of a 40 nm $LaCoO_3$ film on STO-buffered Si(100) at T = 90 K. Encircled in blue are regions where the topography and MFM images have features in common, indicating possible cross-talk between the height and frequency shift profiles in these regions.

The corresponding RMS frequency shift roughness values for each MFM image scale well with the global normalized magnetic moment versus temperature SQUID data for this film presented in fig. 5.28. Though the substrate background has not been precisely removed from the SQUID data, the dip in the zero-field cooled SQUID data between 40-60 K coincides with fluctuations of the local RMS frequency shift roughness values in that temperature range. Interesting to note is the reduction of these fluctuations in both the global and local data upon field-cooling the sample.

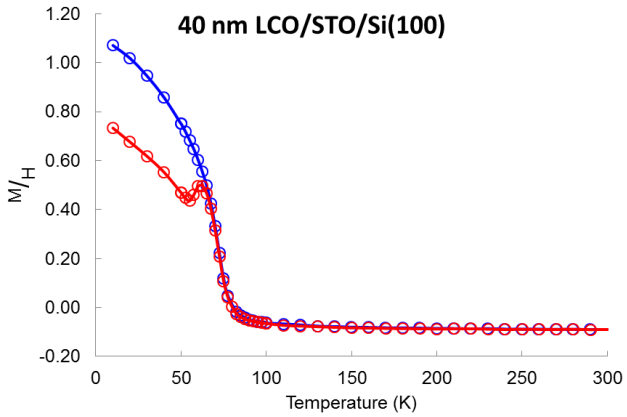

Figure 5.28 Variation of the normalized magnetic moment of a 40 nm $LaCoO_3$ thin film deposited on a $SrTiO_3$-buffered Si(100) substrate with temperature. The red series corresponds to warming up and the blue series corresponds to cooling down.

The derivative of the RMS frequency shift roughness curve with temperature for zero-field cooled LCO/STO/Si(100) shown in fig. 5.29 features a minimum centered about 85 K corresponding to the primary ferromagnetic-paramagnetic transition but also has two other minima, one centered around 65 K and the other around 40 K. The difference between the field cooled and zero-field cooled values of the RMS frequency shift roughness with respect to the zero-field cooled value at each temperature, also shown in fig. 5.29, display peaks between the temperatures at which the secondary minima in the derivative plot are located. This supports competing FM-AFM interactions and anisotropy driving the magnetic character in this sample.

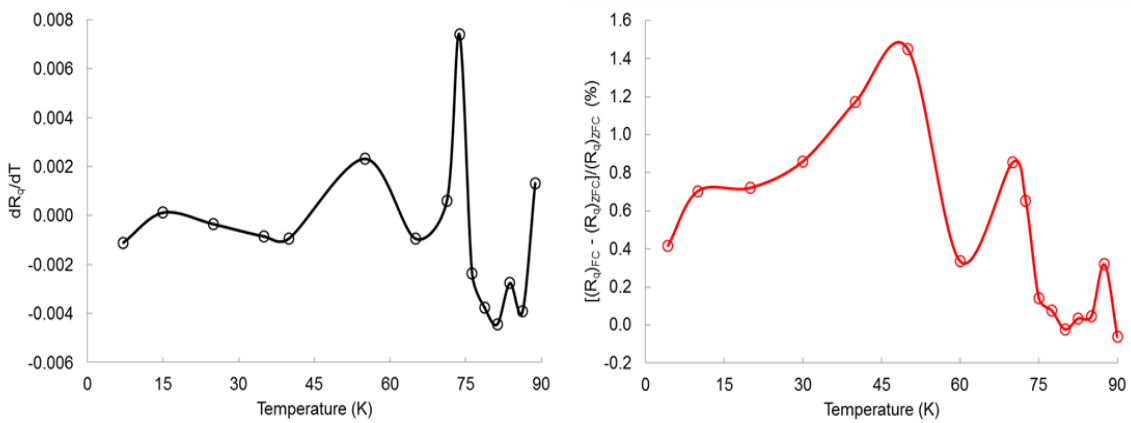

Figure 5.29 Temperature-dependence of the derivative of the RMS frequency shift roughness (left) of each frequency shift image taken for a zero-field cooled 40 nm $LaCoO_3$ film on $SrTiO_3$-buffered Si(100) and the difference of the RMS frequency shift roughness values (right) between field cooled and zero-field cooled 40 nm $LaCoO_3$ film on $SrTiO_3$-buffered Si(100). The image parameters are given in fig. 5.25.

2D autocorrelation and fast Fourier transform (FFT) (see fig.'s 5.30 and 5.31) reveal characteristic directions in real and reciprocal space for both the MFM height and frequency shift profiles. Without knowing the scan direction with respect to the orientation of the thin film we cannot assign directions to the features we observe in the 2D autocorrelation and FFT maps, however relative changes can be noted. In the case of the warming cycle for zero-field cooled 40 nm film of $LaCoO_3$ on STO-buffered Si(100) shown in fig. 5.30 there is a clear directionality to the distribution of topographic features and magnetic domains.

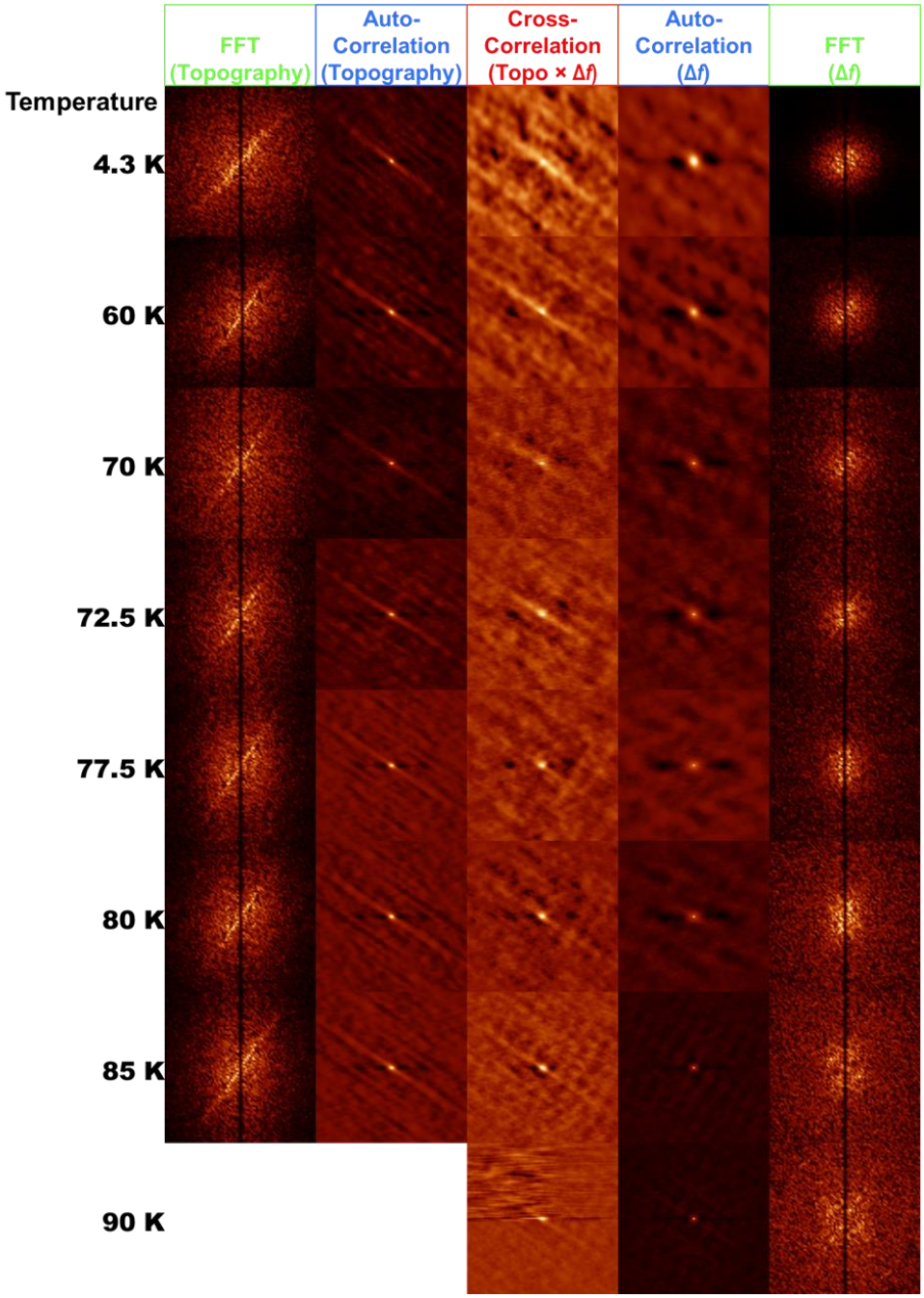

Figure 5.30 Temperature dependence of 2D autocorrelation and fast Fourier transform maps of topography and frequency shift images recorded at the same 5.4 µm x 5.4 µm location on the surface of a zero-field cooled 40 nm $LaCoO_3$ film on STO-buffered Si(100), and temperature dependence of the 2D cross-correlation map of the topography images with the frequency shift images.

Topography autocorrelation shows topographic features higher than the average feature height are likely to be distributed along two directions that appear to be perpendicular to one another. One of these directions is slightly more favored than the other as indicated by the asymmetry of the FFT maps. The autocorrelation and FFT maps of the topography change very little with temperature. On the other hand, autocorrelation maps of the frequency shift image show that at low temperature, the distribution of magnetic domains has a preferred direction which in the neighborhood of 75 K shifts to a direction perpendicular to the preferred direction at low temperature.

Considering that this sample is (001)-oriented with the z-axis pointing normal to the scanning surface, the appearance of characteristic in-plane directions perpendicular to one another reflects the four-fold symmetry of a tetragonal $LaCoO_3$ film. However, asymmetry in the FFT maps and the shift of magnetic domain distribution would indicate that these characteristic directions perpendicular to one another are not energetically equivalent. Magnetic domains at the surface presumably prefer relative easy directions of lowest energy. In the case of this $LaCoO_3$ film in its zero-field cooled state, the direction of lowest energy appears to shift by 90° between 75 K and 80 K. A reduction of the symmetry of the oxygen octahedra due to a change in Co-O-Co angles and/or a change in Co-O bond length with thermal expansion might drive this shift in the relative easy direction for surface domains.[105]

The periodicity observable in the frequency shift autocorrelation maps is also modulated from long to short wavelength with an increase in temperature which is supported by the FFT maps of the frequency shift. This indicates that surface domain width decreases as the temperature increases. The magnetization-dependent contributions to the free energy at the surface include domain wall energy, internal stray field energy

and closure energy. Flux-closure domains at the surface ensure the stray field remains a minimum and the closure energy is proportional to their width, while the domain wall energy is inversely proportional to their width. Thus, a reduction in domain width with temperature marks an increase in domain wall energy and a reduction in closure energy likely in response to a change in the internal stray field of the sample.

The temperature sequence of 2D autocorrelation and FFT maps shown in fig. 5.31 for field cooled 40 nm film of $LaCoO_3$ on STO-buffered Si(100) indicate that below 80 K surface domains are more evenly distributed amongst both diagonal directions and the periodicity observed in the 2D autocorrelation map at lowest temperatures is slightly increased from that observed in the 2D autocorrelation map of the zero-field cooled sample. Surface domain widths are narrower after field cooling than surface domain widths prior to field cooling.

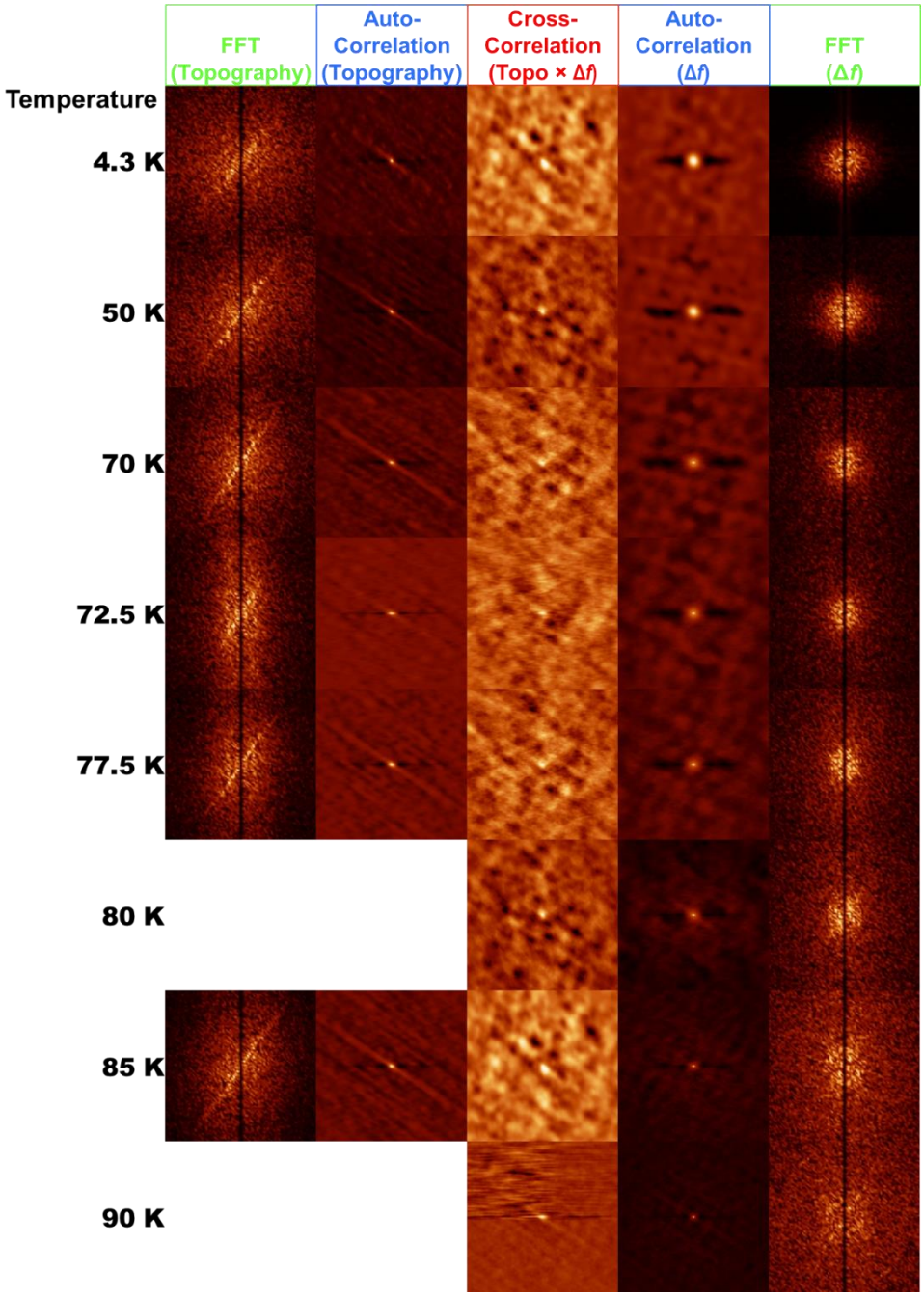

Figure 5.31 Temperature dependence of 2D autocorrelation and fast Fourier transform maps of topography and frequency shift images recorded at the same 5 µm x 5 µm location on the surface of a field cooled (H = 0.034 T) 40 nm $LaCoO_3$ film on STO-buffered Si(100), and temperature dependence of the 2D cross-correlation map of the topography images with the frequency shift images.

5.3.4.2 $LaCoO_3$ on a BTO layer deposited on STO-buffered Si(100)

MFM images (fig. 5.32) for a 15 nm $LaCoO_3$ on a 12 nm layer of $BaTiO_3$ deposited on STO-buffered Si(100) substrate (LCO/BTO/STO-Si) were recorded separately using a magnetic force microscope at Los Alamos National Laboratory.[147] The MFM setup is not configured to obtain topography and thus only the frequency shift images are recorded. The nominal thickness of the $SrTiO_3$ buffer layer is 2 nm.

Frequency shift autocorrelation images again show a competition between "easy" directions for magnetic domain distribution, but that are offset from one another by ~45°. Similar to $LaCoO_3$ on STO-buffered Si the distribution of magnetic domains in LCO/BTO/STO-Si shifts from a predominant direction to an alternate direction as temperature is increased. There also appears to be a shift in the periodicity in the frequency shift autocorrelation from long to short wavelength with an increase in temperature. Unlike $LaCoO_3$ on STO-buffered Si however, the autocorrelation map at higher temperature seems to be dominated by a wide central peak over which the smaller peaks are superimposed, which is reflected in the contraction of features in the FFT maps of the frequency shift. This may indicate the development of extended domains in the surface within which sub-domains have a width that decreases as the temperature increases. This would suggest a more complex energetic landscape where the stray field energy is reduced within sub-domains, allowing the closure domains to diminish in size locally, but extended closure domains begin to form as stray field of interactions between larger domains becomes the dominant contribution. Upon cooling, however, features in the FFT maps of the frequency shift remain disperse and the centralized peak in the autocorrelation map seems to vanish.

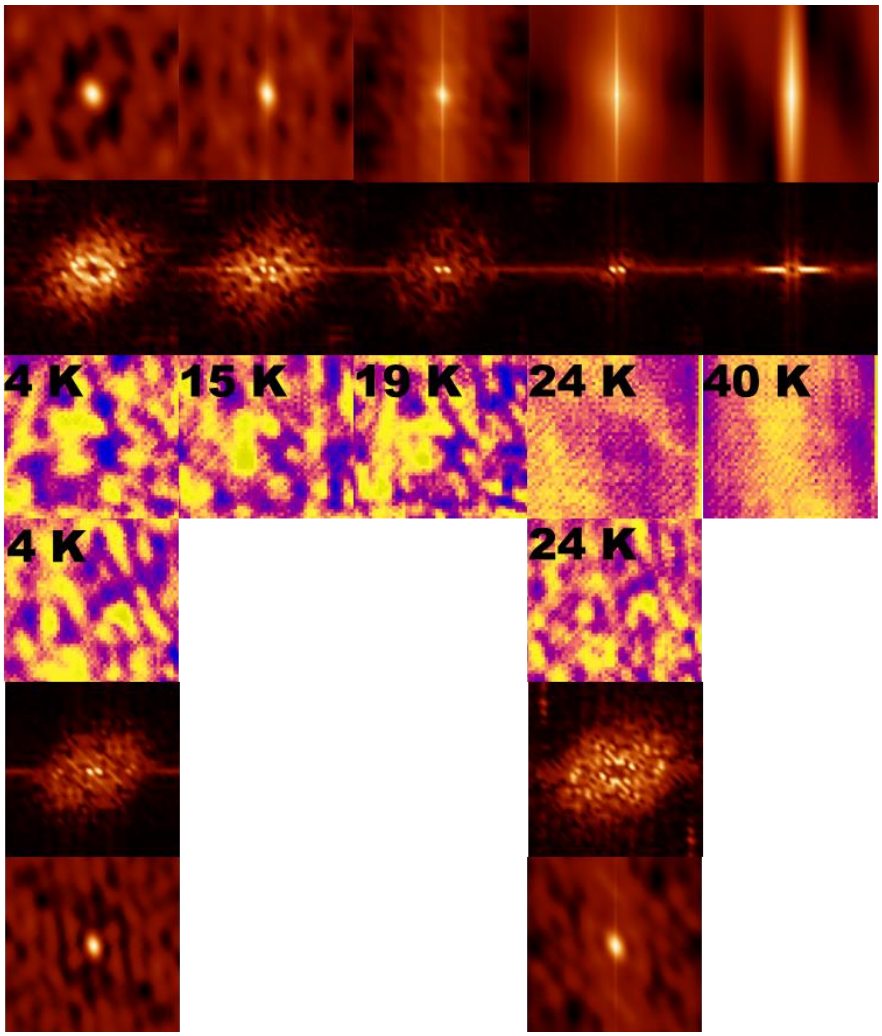

Figure 5.32 The temperature-dependent MFM image sequence (a) for warming and (c) cooling in a magnetic field H = 0.025 T directed normal to the sample surface, and the corresponding RMS frequency shift roughness values (b) of a 15 nm $LaCoO_3$ film on a BTO layer deposited on STO-buffered Si(100) prepared in the remnant state (T=105 K, H = 1 T) over a thermal cycle. The red series in (b) corresponds to warming up and the blue series corresponds to cooling down. The images and corresponding frequency shift data are obtained at the same 4 × 4 μm^2 area. The frequency shift range of the MFM images is ±150 mHz.

As was the case with $LaCoO_3$ on STO-buffered Si, streak-like domains develop with increasing temperature. The streak-like features appear to be slightly different as the film is cooled back through the ordering temperature in the presence of an applied magnetic field and they remain somewhat fixed in size and location over the cooling cycle. We suspect that the persistence of streak-like features through the cooling cycle are tied to the strength of the applied field as shown in the previous section for $LaCoO_3$ on STO-buffered Si, though a much weaker magnetic field was sufficient to fix the streak-like domains in temperature for LCO/BTO/STO-Si.

Magnetic contrast is completely gone by 24 K upon warming but returns upon cooling through 24 K, making the Curie temperature of the film unclear. This is consistent with SQUID results for the film (not shown) which did not indicate a clear transition from a ferromagnetic to a paramagnetic phase with a definitive T_C. There appears to be some hysteresis in temperature. The offset of the temperature at which the film magnetically orders depending on cooling or warming seems to imply that the strain imparted by the substrate is hysteretic in temperature. The structure of $BaTiO_3$ does feature multiple structural phase transitions and exhibits hysteresis with temperature. However, the first structural transition from rhombohedral to orthorhombic occurs near 180 K for bulk $BaTiO_3$. Clamping of the BTO buffer layer due to misfit strain from the substrate is expected to alter the structure of BTO[148] but it seems that an estimated misfit strain between the $BaTiO_3$ and $SrTiO_3$ buffer layers at 40 K of about -3.8%[149] is only enough to induce a cubic phase for the $BaTiO_3$ buffer layer and does not alter the hysteresis profile.

5.3.4.3 $LaCoO_3$ on $LaAlO_3$

We obtained few images for $LaCoO_3$ on $LaAlO_3$, under slight compressive strain. From SQUID measurements (fig. 5.33) it is not clear whether there is a ferromagnetic to paramagnetic transition and that this film has a negligibly small coercive field less than 20 mT. Repeating the same measurement, we find the magnetic characteristics of the film have changed, perhaps indicating that the film degraded over time.

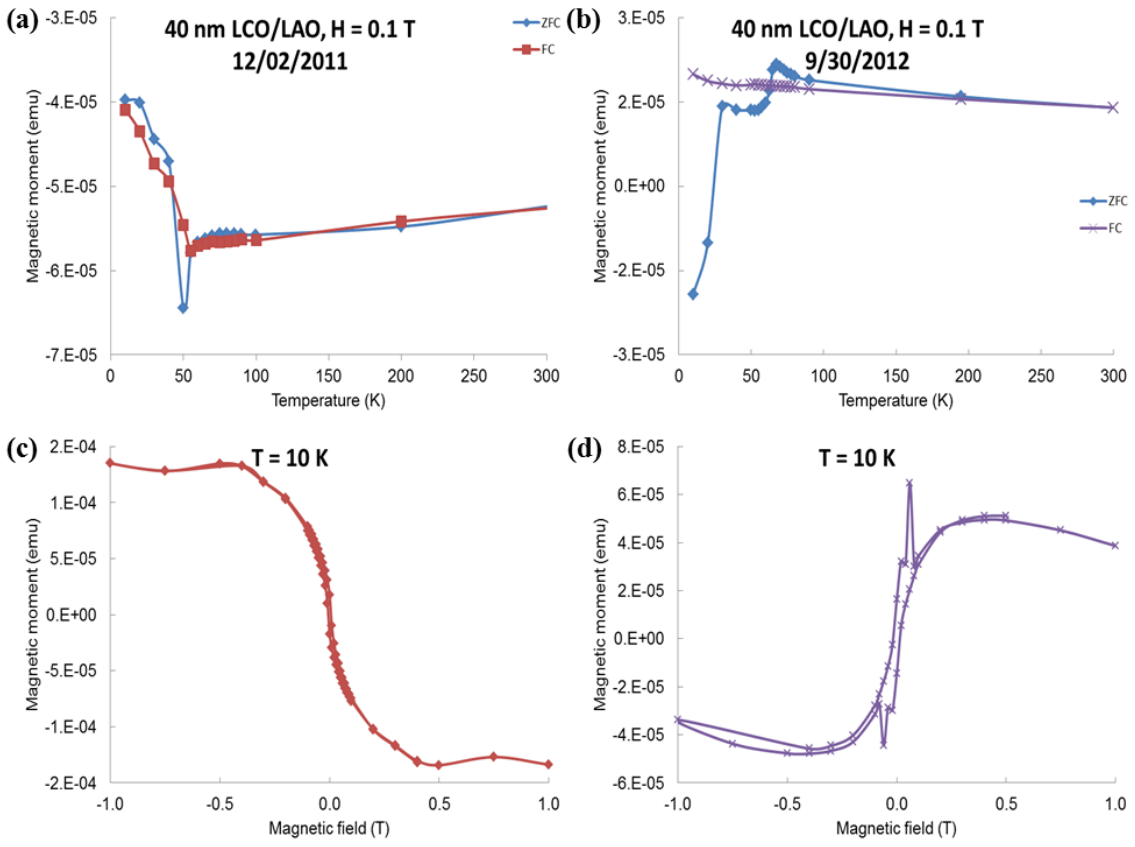

Figure 5.33 Variation of the magnetic moment with temperature measured on (a) 12/02/2011 and (b) 09/30/2012 and the variation of the magnetic moment with applied magnetic field at T = 10 K measured on (c) 12/02/2011 and (d) 09/30/2012 for a 40 nm $LaCoO_3$ thin film deposited on an $LaAlO_3$ substrate.

Despite the change in magnetic characteristics of the film, below 65 K we see some magnetic contrast in MFM data that is not correlated to topography (fig. 5.34). Topographical artifacts are visible in the frequency shift images are due to electrostatic interactions between larger features and the tip. A bias was applied to the tip to compensate for these interactions after which the artifacts disappeared, confirming their origination in topographic cross-talk, but those images are not shown in fig. 5.34 below. There was some difficulty proceeding with the experiment and the tip condition worsened, but before magnetic contrast was entirely lost, we obtained the images featured in fig. 5.35. This is a set of images was taken at the lateral limits of our scanner tube at liquid helium temperatures. There is no apparent correlation between the topographic and frequency shift images but we do note that there are bright, well-defined lines in the magnetic images indicating boundaries along which large in plane domains with orientations anti-parallel to each other meet.

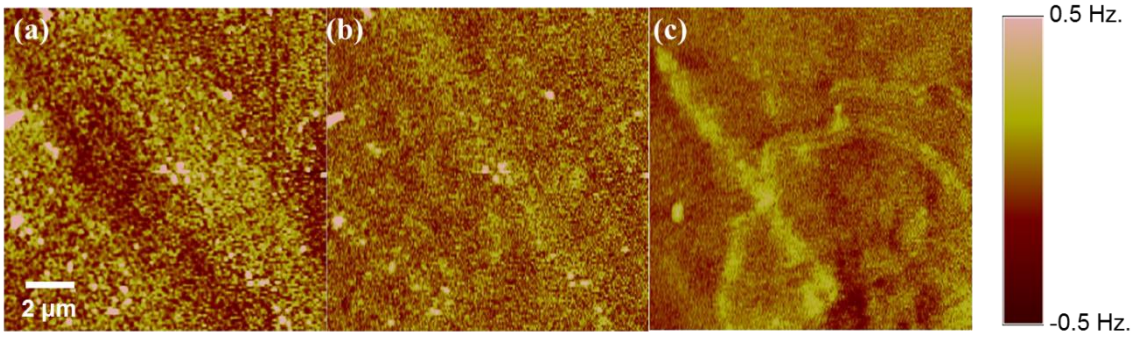

Figure 5.34 (a) Topography image and the corresponding frequency shift images obtained at (b) T = 88 K and (c) T = 62.1 K for the same 13 × 13 μm^2 area of a 40 nm-thick zero-field cooled sample of $LaCoO_3$ on $LaAlO_3$.

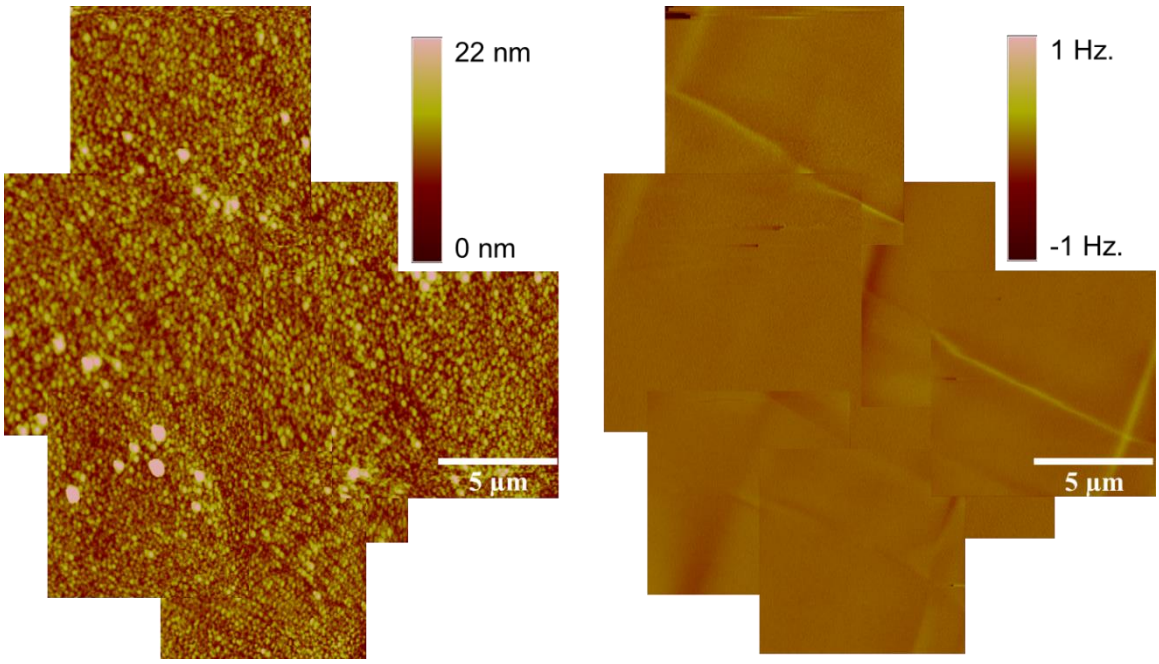

Figure 5.35 Topography image (left) and the corresponding frequency shift (right) image at T = 4.3 K obtained for the same area of a 40 nm-thick zero-field cooled sample of $LaCoO_3$ on $LaAlO_3$.

5.4 Conclusions and Future Work

Magnetic force microscopy is indispensable as a tool to spot local defects that are overlooked in more commonly used characterization techniques. Continuing to study the role of strain in LCO necessitates further studies on the contribution of impurities to the magnetic profile of $LaCoO_3$. In particular, spin-glass behavior for $LaCoO_3$ deposited on $LaAlO_3$ may provide a reference for efforts to optimize the deposition process.

AC susceptibility measurements and dynamic measurement of the zero-field magnetization of LCO thin films can tell us whether the cusps in the zero-field cooled magnetization and the lack of saturation may point to glassy behavior or canted antiferromagnetism.[150,151,152] SQUID data we obtained (not shown) have hinted at film degradation and in the future we must take care to thoroughly investigate whether glassy

behavior might be distinguishable in $LaCoO_3$ thin films on substrates other than $LaAlO_3$ using MFM and SQUID magnetometry. To better quantitatively compare $LaCoO_3$ films using SQUID magnetometry, further measurements are necessary to scrutinize substrate contributions more precisely as well.

Structural effects such a film relaxation with thicker films and with higher tensile strain are substantial contributions to the magnetic character of $LaCoO_3$ as well and warrant further examination. Hysteresis in the $LaCoO_3$ film deposited on $BaTiO_3$ requires further investigation and imposing higher tensile strain on LCO thin films continues to be a fairly uncharted area of research. The first results for LCO grown on LAO substrates with different surface terminations[117] were very intriguing and consideration should be extended to include alternative surface terminations of other substrates and also of $LaCoO_3$. The sensitivity of the magnetic character of $LaCoO_3$ thin films to strain is already being exploited for functional device heterostructures[108] which also alludes to the potential for exploring other compatible materials with complementary features that might be integrated with $LaCoO_3$ thin films.

It is still an open question whether or not domain rearrangement in LCO/LAO occurs as it was found to occur in LCO/STO/Si(100) and LCO/BTO/STO/Si(100). Further MFM studies will be required to determine the critical fields necessary to fix in place the local streak-like domain patterns that emerge with temperature and assess the implications of this phenomenon on the ongoing debate of the role of strain in magnetism in $LaCoO_3$ thin films. A reasonable explanation for local magnetic domain rearrangement with temperature is a response to structural distortion of the LCO lattice produced by thermal expansion. That the rearrangement is reversible in temperature could even allude to a reversible relaxation of strain at higher temperatures perhaps along twinning

boundaries or structural defects. But that this rearrangement also depends on the applied magnetic field suggests that $LaCoO_3$ as a strained thin film may be a magnetostrictive material.

Chapter 6: UMn_2Ge_2

The development of rare-earth magnetic materials has ushered in a modern technological landscape heavily reliant on a handful of rare-earth magnetic alloys for actuators, transducers, electric motors and generators, magnetic bearings and couplings. Neodymium magnets, as an example, are employed in power steering and drive motors for electric cars, generators for wind turbines, in speaker systems, surgical implants and magnetic resonance imaging.

Given the extensive range of applications for these materials, they pervade guidance, communications and propulsion systems employed for national defense, and their production is of national importance. After 1984, production of rare-earth metals in China surpassed that of domestic production in the United States and it continues to dominate rare-earth production. In 2010, China's share of rare-earth production exceeded 95%. In anticipation of strained supplies and increased dependence on foreign production and manufacturing, the United States Department of Energy is currently funding efforts to research alternative materials for permanent magnet technology.[153]

Figures of merit for permanent magnets include flux density, energy product, coercivity, usable temperature range, magnetization change with temperature, which are all influenced to a degree by magnetic anisotropy in the magnetic material. The degree to which magnetic anisotropy in materials like samarium cobalt and neodymium iron boride can be controlled (e.g.- through doping and/or thermal treatment in the presence of a magnetic field) make them favorable for industrial applications.

An interesting material similar in some respects to $Nd_2Fe_{14}B$ (NdFeB), UMn_2Ge_2 (UMG) is a ternary intermetallic permanent magnet that crystallizes in a $ThCr_2Sr_2$ structure (fig. Figure 6.1). Notably, related uranium germanide compounds such as UGe_2

and UCoGe and other uranium-based ternary compounds that crystallize in the "122" structure such as URu_2Si_2 exhibit magnetism-mediated superconductivity and even coexistence of antiferromagnetic and ferromagnetic phases with the superconducting phase.[154,155,156,157] Relatively little is published regarding UMG but it is generally agreed upon that UMG derives its magnetic character from interactions between uranium and manganese moments on their respective sublattices. At temperatures above 200 K manganese moments dominate and are fairly isotropic. Below 200 K however, as the lattice contracts, uranium moments with strong spin-orbit coupling order and introduce anisotropy causing electron spins to preferentially align along an easy axis. Previous reports of an abrupt change in the in-plane lattice constant at 150 K suggest a structural transition coincides with the ordering of uranium moments.[158]

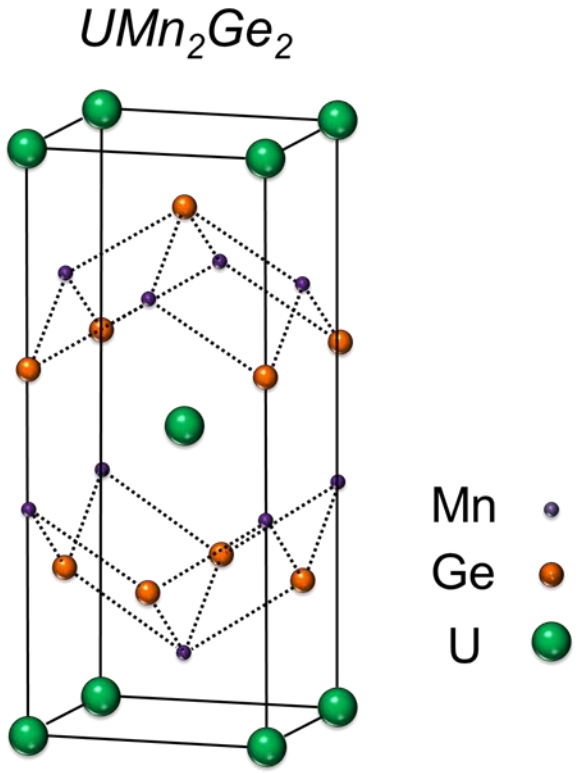

Figure 6.1 Crystal structure of UMn_2Ge_2.

In this chapter previous experimental results pertinent to the magnetic characteristics of UMn_2Ge_2 will be reviewed and compared with X-ray diffractometry, SQUID magnetometry, and magnetic force microscopy results we have obtained for a single crystal sample of UMn_2Ge_2. We investigate the possibility of a local domain structure and magnetization sensitive to a transition near 150 K and seek out indications of anisotropy in UMG. Given Kerr effect results for NdFeB, we are able to infer some important conclusions about UMG and draw parallels between UMG and NdFeB. The potential tunability and optimization of UMG as a permanent magnetic material will also be discussed.

6.1 PREVIOUS EXPERIMENTAL RESULTS FOR UMn_2Ge_2

6.1.1 Global Measurement

6.1.1.1 Diffraction Analysis

Due to the large variability in electronic behavior of $R_2T_2Ge_2$ and $R_2T_2Ge_2$ compounds (R = Ca, Y, La, Ce, Nd, Sm, Gd, U; T = Mn, Fe, Co, Ni, Cu, Ru, Rh, Pd), a great deal of effort has been devoted to tie characteristic interatomic distances to the electronic properties of these materials. As a result, X-ray diffraction and neutron diffraction data on UMn_2Ge_2 and related compounds is abundantly available. [158,159,160] An important criterion for this material which is repeatedly referred to in the X-ray diffraction reports is the Hill limit that indicates the distance between neighboring uranium atoms beneath which 5*f* electron orbitals will directly overlap with one another ($d_{U\text{-}U} \leq 3.5$ Å). Below this limit it is expected that 5*f* electrons will delocalize, diminishing the ability of uranium moments to polarize. A decrease in $d_{U\text{-}Mn}$ is also

expected to result in an increase in 5*f*-3*d* hybridization and reduction of the uranium and manganese magnetic moments. Antiferromagnetic interactions between neighboring manganese atoms is expected for distances between neighboring manganese atoms less than 2.87 Å. One group observed an abrupt jump in the lattice parameter for UMn_2Ge_2 at T = 150 K (fig. 6.2) which they ascribed to the magnetostriction contribution of the uranium sublattice.[158]

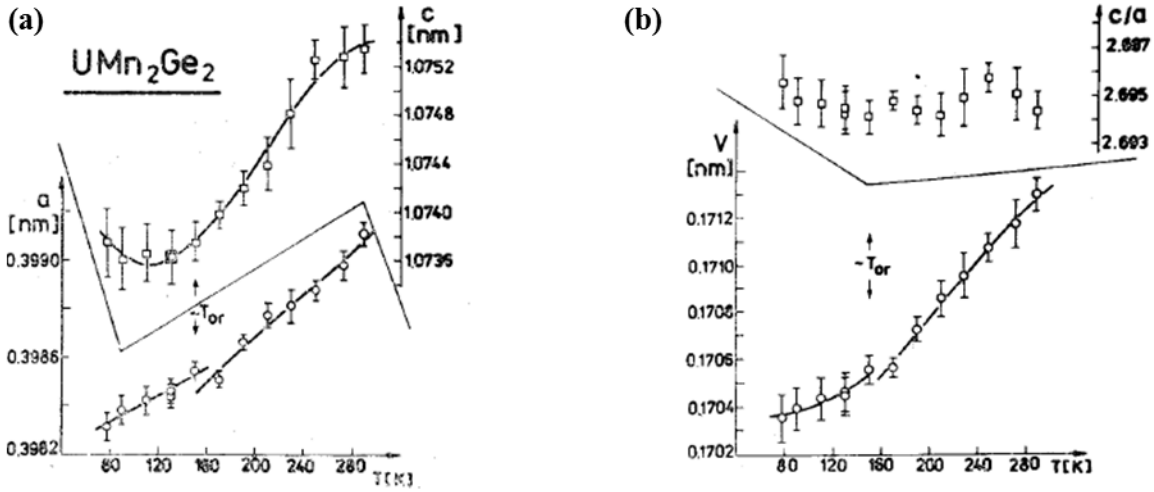

Figure 6.2 Temperature dependence of the (a) in-plane lattice constant, *a*, and out-of-plane lattice constant, *c*, and the corresponding variation in (b) the *c*/*a* ratio and unit-cell volume for UMn_2Ge_2 taken from ref. [158].

Given the dependence of magnetic properties on $d_{U\text{-}U}$, $d_{Mn\text{-}Mn}$, $d_{U\text{-}Mn}$, $d_{Mn\text{-}Ge}$, X-ray diffraction studies were extended to include measurement of UMn_2Ge_2 under pressure.[161] Up to a pressure of 12.4 GPa *a*, *c*, and the *c*/*a* ratio monotonically decrease and the tetragonal structure of UMn_2Ge_2 is preserved. A reversible phase transition to an indistinguishable structure was observed to occur for pressures above 16 GPa. The isothermal bulk modulus measured for UMn_2Ge_2 is comparatively smaller than that of other isostructural uranium compounds, suggesting that 5*f* electrons in UMn_2Ge_2 may be

comparatively less itinerant.[162] To draw more definitive conclusions about the effect of pressure on the electronic properties of UMn_2Ge_2 the experimental values for the lattice constants under pressure were utilized in density functional theory (DFT) calculations.[163] When spin-orbit coupling for uranium moments is taken into account, the DFT calculation of the total magnetic moment of UMn_2Ge_2 under ambient conditions agrees fairly well with experimental values. For increasing pressure, DFT predicts an increased 5*f*-3*d* hybridization resulting in delocalized electrons and a reduction in overall magnetic moment. Interestingly, calculations also suggest that an antiferromagnetic state is stabilized at high pressures rather than a complete suppression of magnetism.

6.1.1.2 Magnetic Measurements

One study employs nuclear magnetic resonance measurements to probe manganese spins in UMn_2Ge_2.[164] A single resonance due to ^{55}Mn nuclei that is independent of temperature is observed at 150.1 MHz. However, the spin-echo signal decreases in intensity as a function of temperature, dropping to zero by T = 60 K. The hyperfine field at the manganese nuclei measured for other isostructural manganese compounds had previously been attributed to the local moment on manganese atoms but, in principle, if this were also the case for UMn_2Si_2 and UMn_2Ge_2 the authors would have expected to observe higher resonance frequencies. The authors attribute this difference to additional contributions due to U-Mn coupling and claim the reduction in the uranium moments in UMn_2Si_2 and UMn_2Ge_2 (1.14 μ_B, 1.99 μ_B at T = 4.2 K, respectively) versus that of uranium ions (3.5 μ_B) as further evidence of their assertion. Remarkably, the ordering of the uranium sublattice at 80 K does not alter the decreasing trend in the spin-echo signal observed for UMn_2Si_2 in any noticeable way. This would imply that the

uranium moment is small or that it orders in such a way to produce a net zero contribution to the hyperfine field at Mn nuclei, contradictory to the observation of a low-temperature uranium moment for both UMn_2Si_2 and UMn_2Ge_2.

A number of Kerr effect studies have been conducted on UMn_2Ge_2 as well.[165,166] Because $LaMn_2Si_2$ and $LaMn_2Ge_2$ were both found to have a negligible Kerr rotation, the small finite Kerr rotation observed for UMn_2Si_2 and UMn_2Ge_2 were at first attributed entirely to uranium moments. But further examination of the temperature dependence of the Kerr rotation for UMn_2Ge_2 demonstrated the persistence of Kerr rotation up to T = 380 K, the T_C at which manganese orders magnetically. This gives one the impression that manganese moments do contribute to non-zero Kerr rotation at higher temperatures, even if only through uranium-mediated interactions. Granted that the effect of uranium moments on manganese ones is appreciable at temperatures well above the onset of magnetic ordering in the uranium sublattice, whether or not it is appropriate to state that the manganese sublattice orders at T_C, independently of the uranium sublattice is debatable.

The onset of ferromagnetism in UMn_2Ge_2 at T_C = 380 K has been confirmed by susceptibility measurements.[165,167] Further data regarding the temperature and field dependence of global magnetic properties of UMn_2Ge_2 available from a Kerr rotation study[166] and SQUID results published in a neutron diffraction study[160] are summarized in fig. 6.3. Saturation occurs near H = 0.8 T of the Kerr rotation hysteresis loop, with a Kerr rotation angle of 0.15° at saturation in good agreement with van Engelen et al. A coercive field $H_c \sim 3500$ Oe is observed for UMn_2Ge_2. The saturation magnetization and coercivity of UMn_2Ge_2 are comparable to that of the well-known magnetic material AlNiCo.

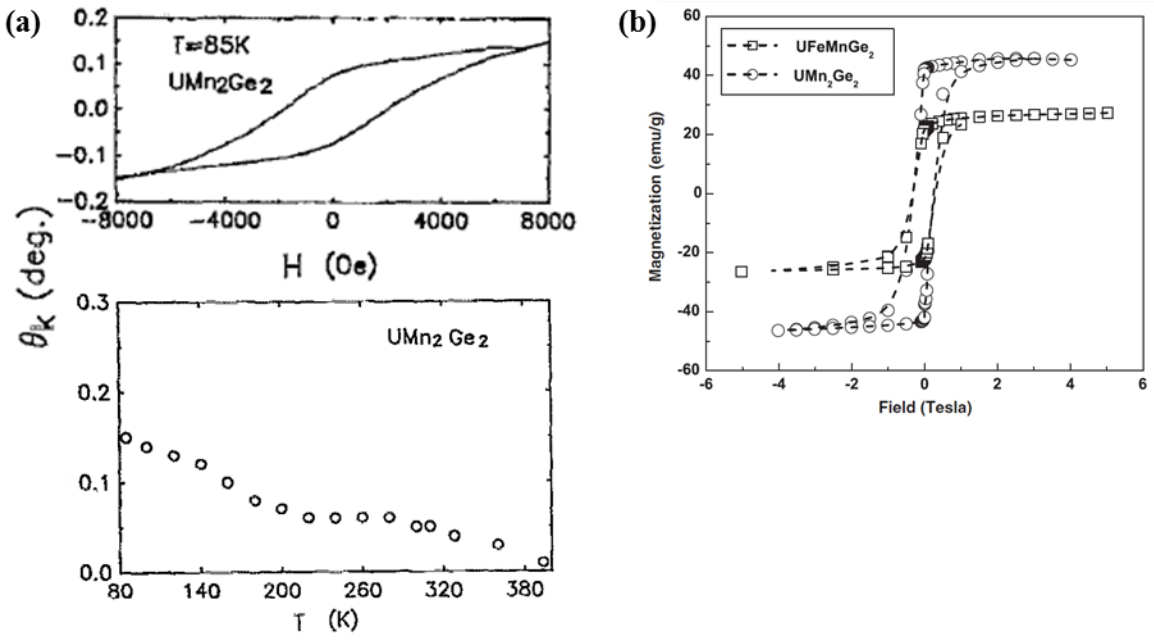

Figure 6.3 (a) Magnetic hysteresis loop (top) and temperature-dependence of the Kerr rotation angle (bottom) for UMn_2Ge_2 taken from ref. 165. (b) SQUID magnetometry measurement of magnetic hysteresis of $UFeMnGe_2$ and UMn_2Ge_2 taken from ref. [160].

6.2 EXPERIMENTAL RESULTS FOR UMn_2Ge_2

6.2.1 SQUID Magnetometry Data

Preliminary SQUID magnetometry results obtained for UMn_2Ge_2 are presented in fig. 6.4. The SQUID data indicates that there is a transition near 380 K, coinciding with the onset of ferromagnetic ordering. The temperature dependent magnetization peaks at 360 K and flattens out between 320 K and 200 K. Below 200 K a gradual increase in the magnetization occurs most likely due to an increase in the uranium moment. The saturation field and coercivity of the sample are higher at lower temperatures, $H_s \approx 1$ T at 80 K versus $H_s \approx 0.5$ T at 200 K. The sample coercivity is less than 0.02 T which is an order of magnitude less than the values previously published for UMn_2Ge_2 in the

literature. These results were obtained from SQUID measurements performed on multiple fragments of a UMn_2Ge_2 sample that were randomly oriented with respect to the direction of the applied magnetic field in the SQUID magnetometer. We would expect to observe the maximum coercivity of the sample provided that the orientation of the applied magnetic field lies along an easy axis of the sample. Without knowing the orientation of the applied magnetic field with respect to the orientation of the sample, our coercivity measurements are not conclusive and require further investigation.

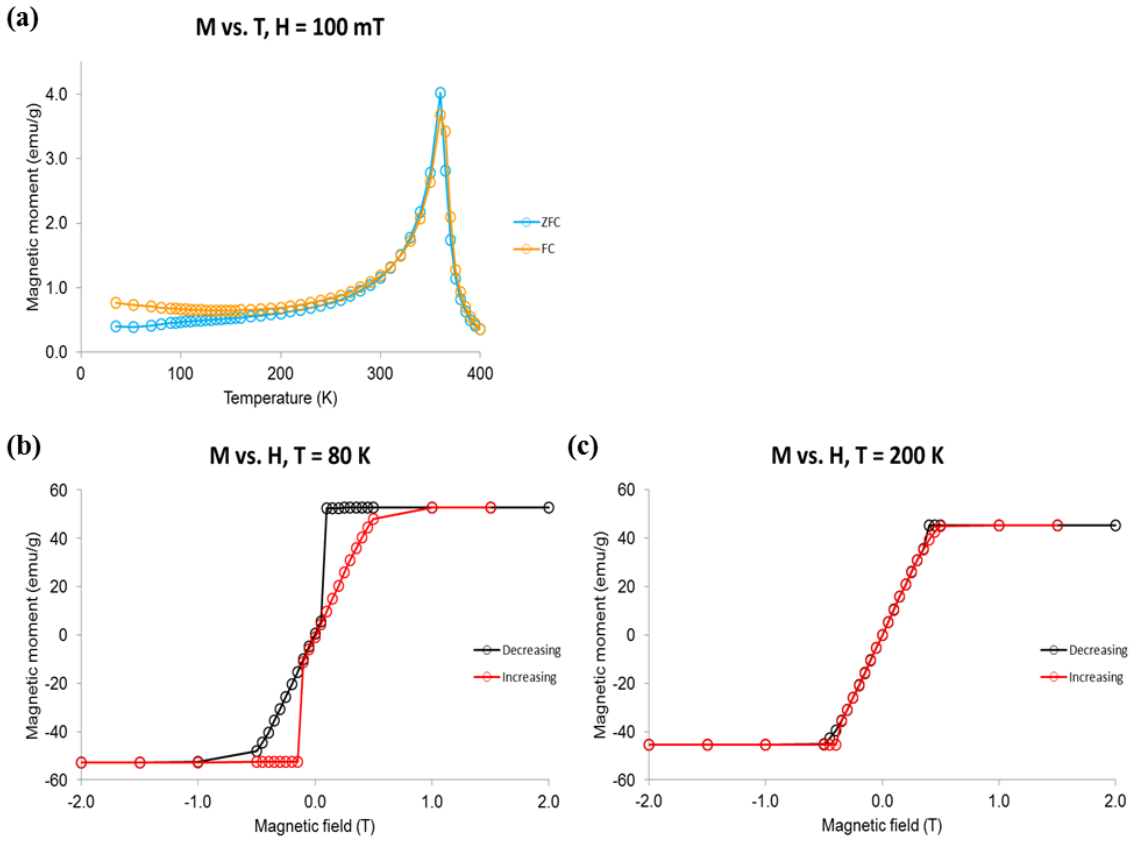

Figure 6.4 Variation of the magnetic moment of UMn_2Ge_2 with (a) temperature and applied magnetic field at (b) T = 80 K and (c) T = 200 K.

It is interesting to note that the hysteresis loop opens up at liquid nitrogen temperatures as opposed to being quite narrow at 200 K. This would indicate a higher anisotropy at lower temperatures possibly due to the influence of uranium moments. At lower temperatures both the width and the slope of the hysteresis loop are different at different field strengths which indicate the presence of different phases with different susceptibilities and differing degrees of anisotropy. Though UMn_2Ge_2 becomes a harder (more anisotropic) magnet at low temperature, SQUID data seems to indicate the co-existence of hard and soft phases at low temperature with different susceptibilities depending on the strength of the applied magnetic field.

6.2.2 Optical Images and X-ray Characterization

The UMn_2Ge_2 samples our group obtained from Los Alamos National Laboratory were relatively rough. We mechanically polished one of the samples to improve the smoothness of the surface. Optical microscopy images of the sample, obtained using a Leitz Leica ErgoLux Research Microscope, before and after polishing are shown in fig. 6.5. At first glance, the surface smoothness is much improved after polishing, but on closer inspection faint texturing due to the polishing process is visible. Given that the diffraction limit is roughly a few hundred nanometers using modern optics, optical microscope images can be used to qualify whether a surface is smooth enough to be imaged using an atomic force microscope. From experience, scanning features at or exceeding 100 nm in size using the multi-mode atomic force microscope for this study precludes resolving sample surface topography well, degrades scanning probe tips more

quickly and produces artifacts in lift-mode imaging for local magnetic and electrostatic mapping.

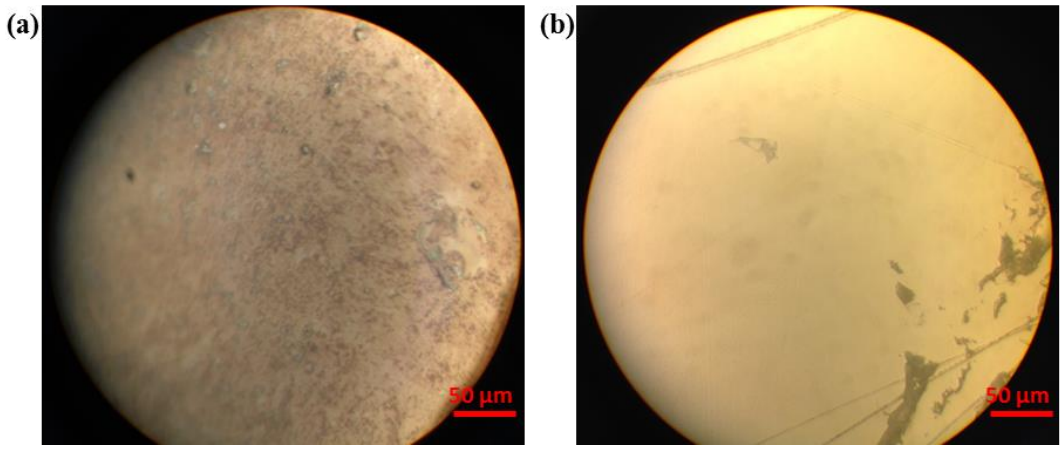

Figure 6.5 Optical microscopy images of (a) an unpolished and (b) a polished sample of UMn_2Ge_2 taken at 50X magnification. The images were not taken in the same location.

Laue diffractometry data obtained by Dr. Steve Swinnea, shown in fig. 6.6, confirm that the UMn_2Ge_2 sample is single crystal and c-axis oriented with a c-axis lattice constant around 10.8 Å.

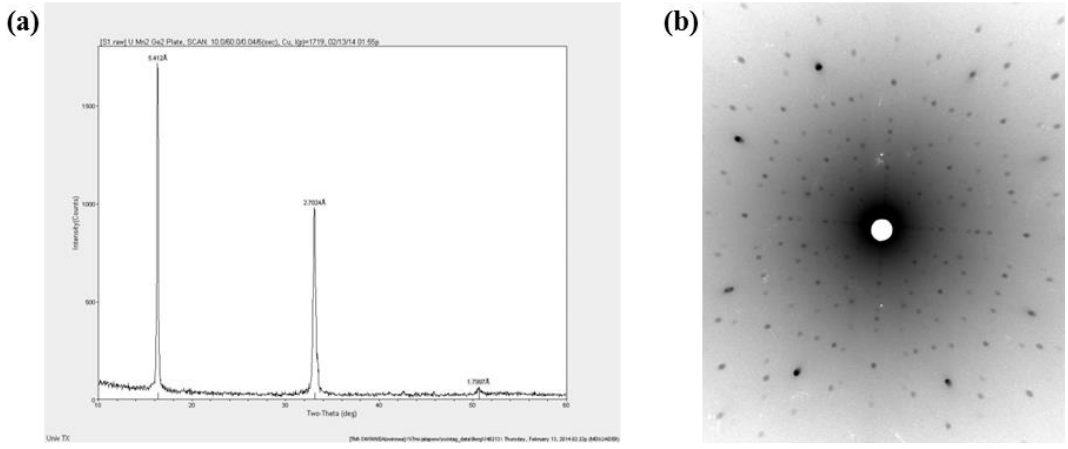

Figure 6.6 (a) 002, 004, and 006 peaks and (b) a diffraction image of UMn_2Ge_2 sample using the Laue method.

6.2.3 Magnetic Force Microscopy

Magnetic force microscopy scans were performed on the unpolished and polished samples in ambient conditions using a Veeco di Multimode V scanning probe microscope with a NanoScope V controller (fig. 6.7). The effect of polishing is readily apparent in both the topographic and frequency shift images of the polished sample. In order to preserve the intrinsic magnetic profile of the UMn_2Ge_2 surface, care must be taken when altering the surface condition. Interestingly, the phase shift images for the UMn_2Ge_2 surface greatly resemble magneto-optical Kerr effect (MOKE) images of NdFeB[168], a well-known ferromagnetic material, shown in fig. 6.8.

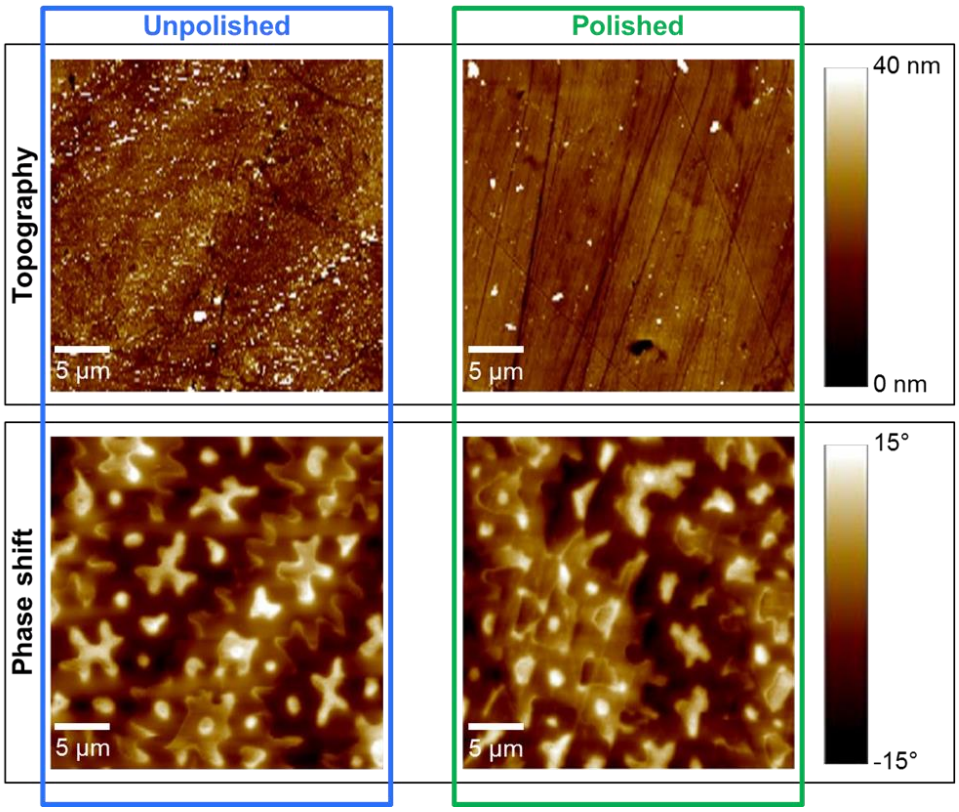

Figure 6.7 $30 \times 30\ \mu m^2$ topography and phase shift images of an unpolished and polished sample of UMn_2Ge_2 in air and zero-field (H = 0 T). The phase shift images were obtained at a lift height of 200 nm and the range of the phase shift in the MFM images is ± 15°.

High-anisotropy uniaxial materials, like NdFeB, feature branching magnetic domains that are arranged in broad, extended patterns in the bulk to reduce wall energy. Bulk domains achieve this by orienting anti-parallel to one another along the material's easy axis. Finer patterns of closure domains at the surface minimize the surface energy. This is clearly demonstrated for NdFeB in fig. 6.9 using the Kerr effect.[168] Depending on the crystallographic plane orientation with respect to the anisotropy axis, imaged domain patterns shift from a wide pattern of anti-parallel domains extending along the easy axis to fine-featured patterns of closure domains. Extending this conclusion to the MFM

images acquired for UMn_2Ge_2, we infer that the MFM images were obtained in a plane perpendicular or nearly perpendicular to the easy-axis of UMn_2Ge_2. With confirmation from Laue diffraction results in the previous section that the sample is *c*-axis oriented and the *c* axis is directed out of the surface normal of the UMn_2Ge_2 sample, we are led to the conclusion that the easy axis of the UMn_2Ge_2 sample lies along the *c*-axis of the material.

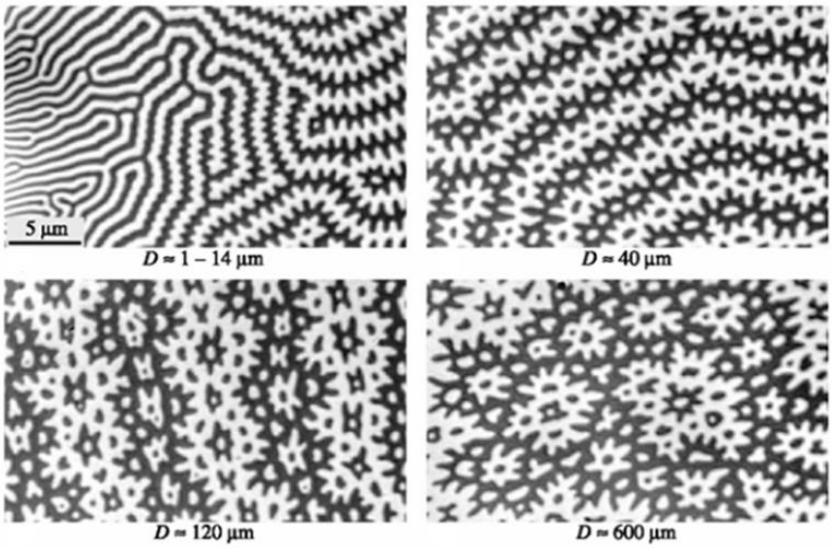

Figure 6.8 Magneto-optical Kerr effect images of the basal plane of Dy-modified NdFeB crystals of various thicknesses taken from ref. [168]. With increasing sample thickness, *D*, the degree of domain branching increases.

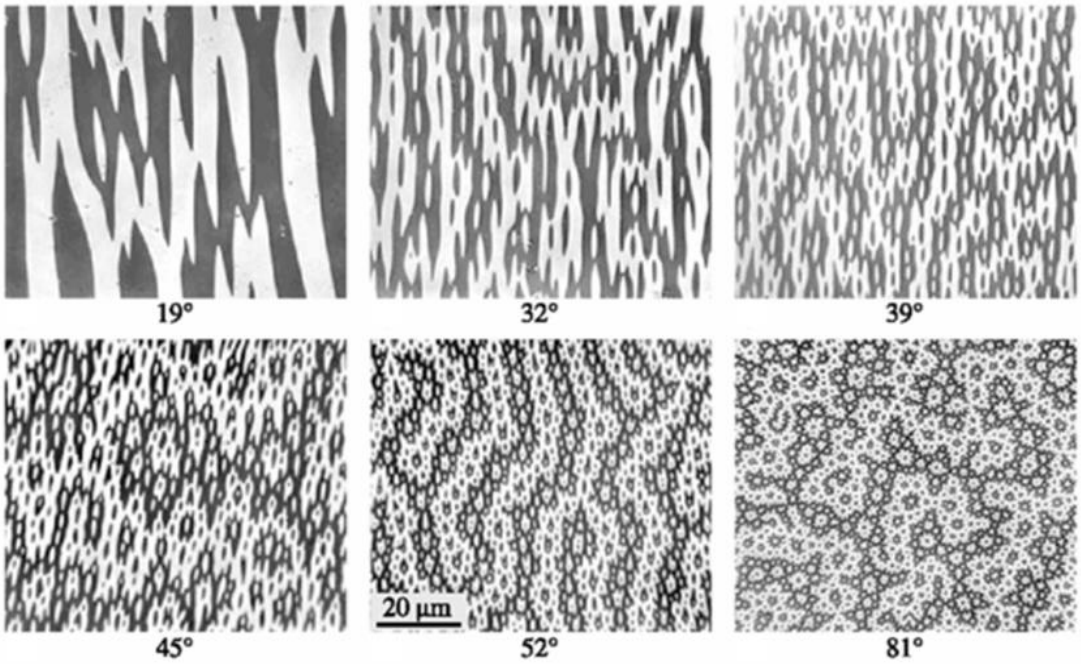

Figure 6.9 Magneto-optical Kerr effect images of Dy-modified NdFeB crystal grains of increasing misorientation taken from ref. [168].

Magnetic force microscopy images taken at three different scan sizes of the surface of UMn_2Ge_2 were obtained at various temperatures. Acquired MFM images with the largest field of view (27 μm × 27 μm) are presented in fig. 6.10. There is obvious correlation between topographic images and frequency shift images. Due to the choice of feedback parameters and charge contrast in MFM images, topographic artifacts are often observed in the frequency image. This sample is unique because the interaction between stray fields in the sample and the magnetic tip is strong enough that frequency shift artifacts become visible in the topographic images. Presumably, the stray magnetic field of the sample interacts with the cantilever during the entire swing of its oscillation and dominates near-field forces due to contact. The frequency shift values are also unusually larger than what we're accustomed to imaging. Over the course of these measurements

contrast switching in topographic images is visible where frequency shift artifacts appear and disappear depending on the condition of the tip.

Magnetic domain size and shape as seen in the frequency shift images remain fairly stable as the temperature is varied from liquid nitrogen temperatures up to 200 K and an abrupt structural transition is not apparent in either the surface topography or the frequency shift images. This is confirmed by fast Fourier analysis and correlation images presented in fig. 6.11. The directionality in correlation mapping and modulation in fast Fourier transform images remain fairly the same as temperature increases. Due to frequency shift artifacts in the topographic images with opposite contrast to features in the frequency shift image, topographic and frequency shift images obtained using MFM are anti-correlated as indicated by the black origin at the center of the cross correlation maps.

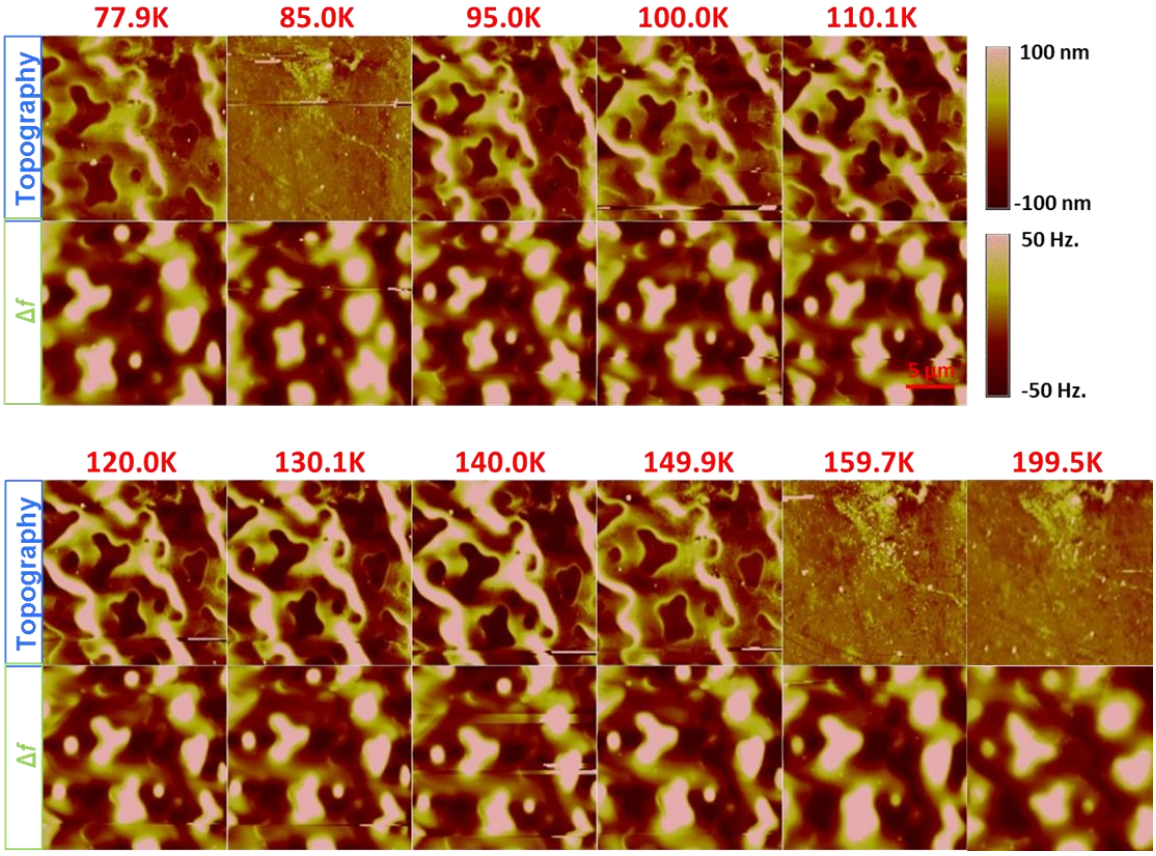

Figure 6.10 The temperature-dependent MFM image sequence for warming in zero-field (H = 0 T) of a UMn_2Ge_2 sample. The images and corresponding frequency shift data are obtained at the same 27 × 27 μm^2 area. The frequency shift images were obtained at a lift height of 200 nm and the range of the frequency shift in the MFM images is ± 50 Hz.

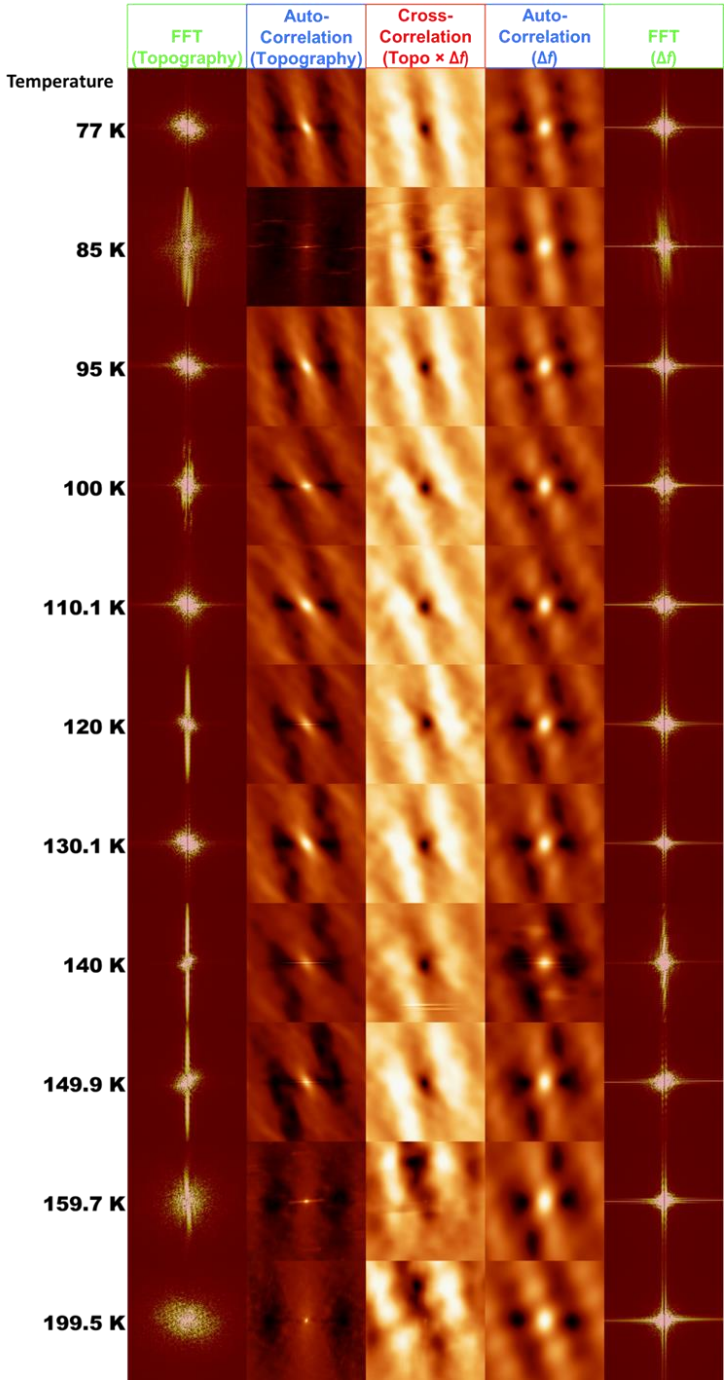

Figure 6.11 The temperature-dependent topography fast Fourier transform (FFT), topography auto-correlation, cross-correlation of topographic and frequency shift images, frequency shift auto-correlation, and frequency shift FFT maps taken from the MFM image sequence in fig. 6.10.

However, the Root Mean Square (RMS) roughness values of the frequency shift data as shown in fig. 6.12 clearly shows fluctuations in the magnetization of the sample stray field at 150 K that interrupt an otherwise decreasing trend in the frequency shift data. This data supports the prospect of magnetostrictive effects accompanying a structural transition in UMn_2Ge_2. Given the local nature of MFM measurement, trends in the local data can vary widely from their global counterparts and can vary even between imaging sites. Further investigation would be necessary to determine how universal an occurrence this behavior is.

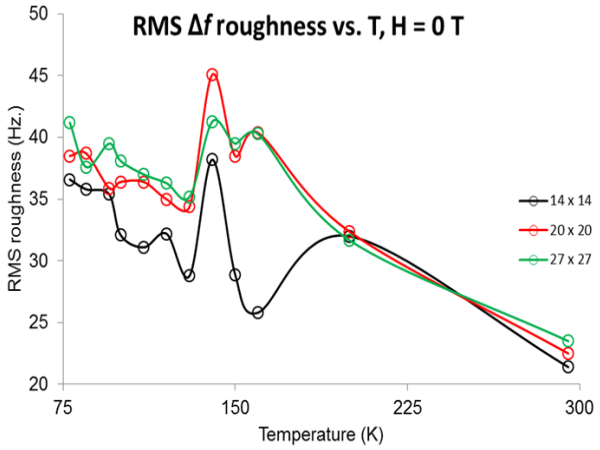

Figure 6.12 Temperature-dependence of the RMS frequency shift roughness for a 14 µm × 14 µm (black), 20 µm × 20 µm (red), and 27 µm × 27 µm (green) image taken of the surface of a zero-field cooled sample of UMn_2Ge_2. The image parameters are given in fig. 6.10.

MFM images acquired while varying the applied magnetic field at liquid nitrogen temperatures are given in fig. 6.13. As the field is increased to 190 G, ribbon-like domain structures alternate in contrast, some remaining dark while others begin to light up. The amorphous dot-like domains retain their contrast as the field is increased. However when

the direction of the applied magnetic field is reversed and the magnitude increased, the ribbon-like domains switch contrast and even the dot-like domains begin to change contrast. It appears that a higher field is required to flip the magnetization direction of the dot-like domains and a lower field to switch the ribbon-like domains. This is consistent with a multi-phase material with non-uniform coercivity.

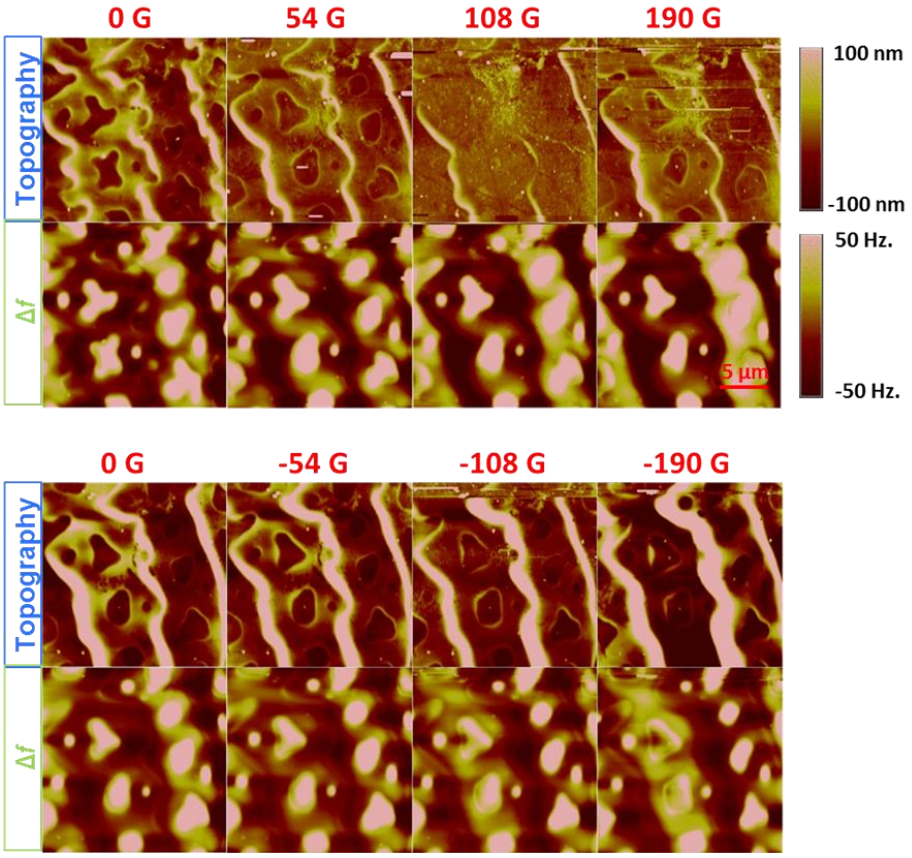

Figure 6.13 The field-dependent MFM image sequence for a zero-field cooled UMn_2Ge_2 sample at liquid nitrogen temperature. The images and corresponding frequency shift data are obtained at the same 27 × 27 μm^2 area. The frequency shift images were obtained at a lift height of 200 nm and the range of the frequency shift in the MFM images is ± 50 Hz.

Using the field-dependent Root Mean Square (RMS) roughness values of the frequency shift data as shown in fig. 6.14, we can infer a local coercive field strength of about one hundredth of a Tesla which agrees fairly well with the global coercive field measurement using the SQUID magnetometer.

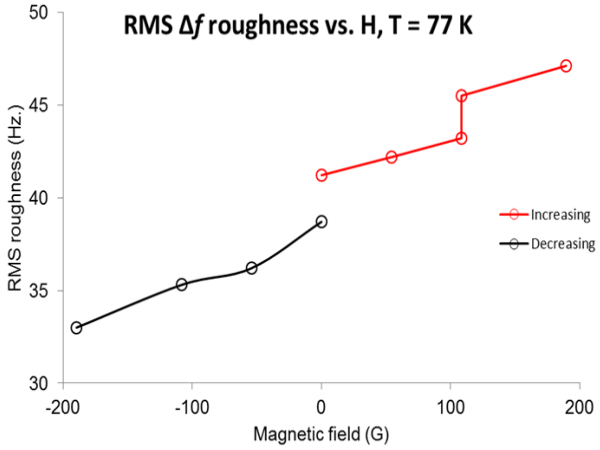

Figure 6.14 Field-dependence of the RMS frequency shift roughness for a 27 μm × 27 μm image taken of the surface of a zero-field cooled sample of UMn_2Ge_2. The image parameters are given in fig. 6.13.

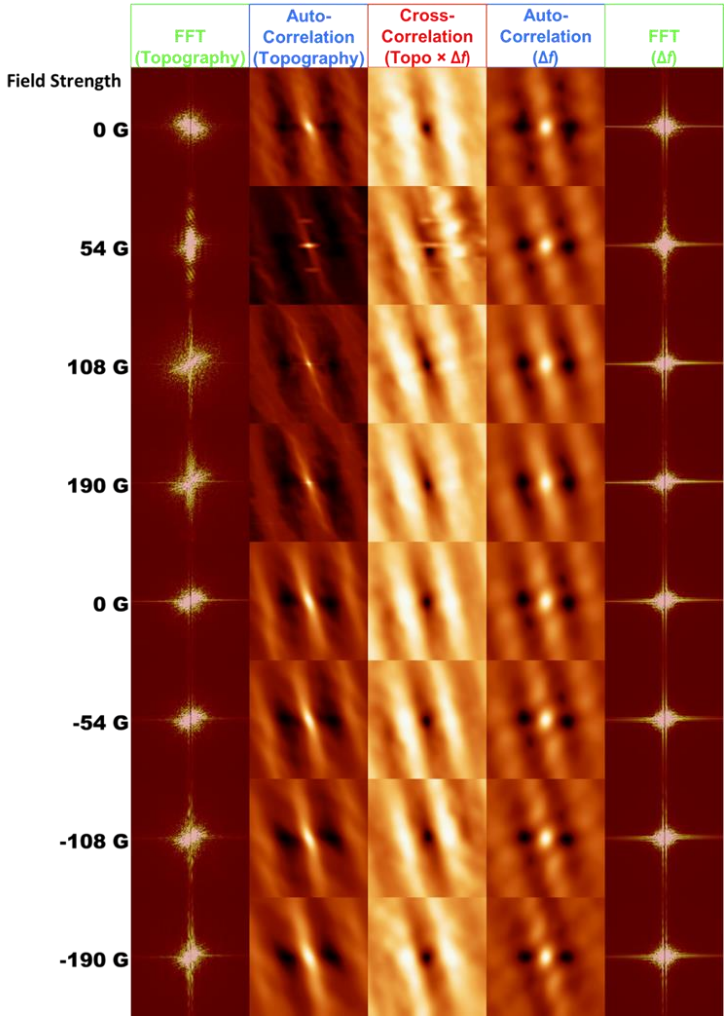

Figure 6.15 The field-dependent topography FFT, topography auto-correlation, cross-correlation of topographic and frequency shift images, frequency shift auto-correlation, and frequency shift FFT maps taken from the MFM image sequence in fig. 6.13.

MFM images at 160 K (fig. 6.16) show domains that behave fairly similarly to those at liquid nitrogen temperatures when the magnetic field is varied. However, the field-dependent RMS roughness values of the frequency shift data, shown in fig. 6.17, no longer coincides with low-field SQUID measurements and it is difficult to arrive at a local coercivity value. But deviations of local measurements from global ones are not unexpected.

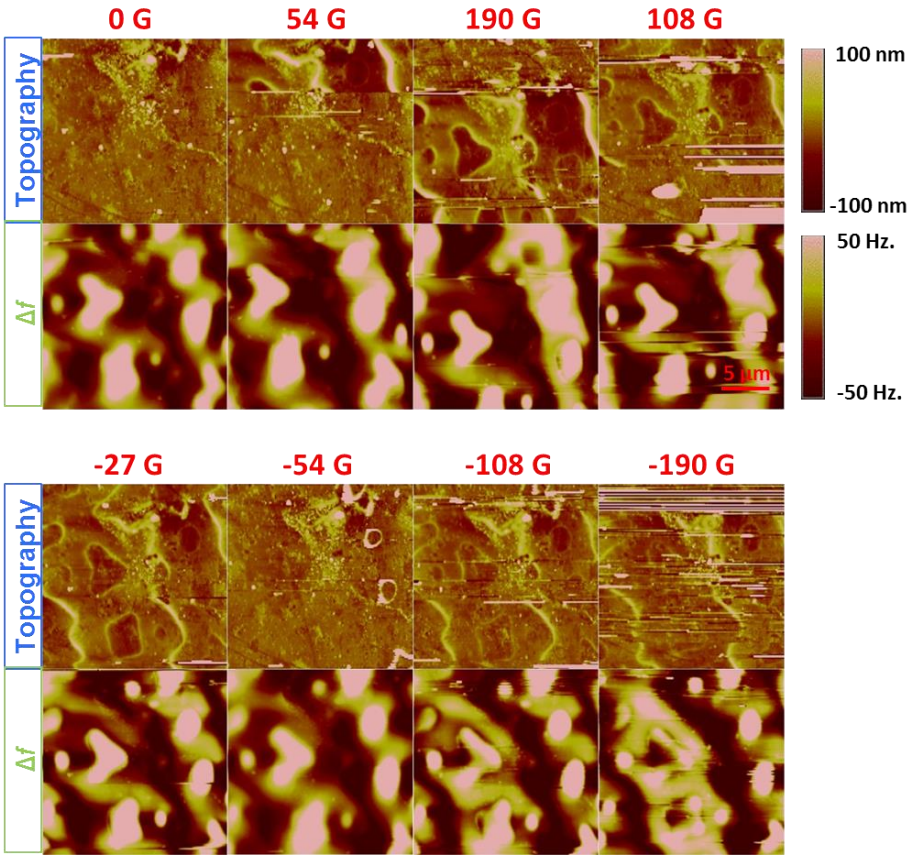

Figure 6.16 The field-dependent MFM image sequence for a zero-field cooled UMn_2Ge_2 sample at 160 K. The images and corresponding frequency shift data are obtained at the same 27 × 27 μm^2 area. The frequency shift images were obtained at a lift height of 200 nm and the range of the frequency shift in the MFM images is ± 50 Hz.

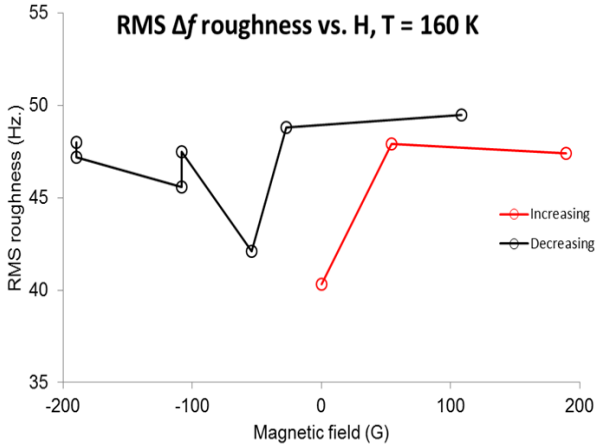

Figure 6.17 Field-dependence of the RMS frequency shift roughness for a 27 μm × 27 μm scan of the surface of a zero-field cooled sample of UMn_2Ge_2. The image parameters are given in fig. 6.16.

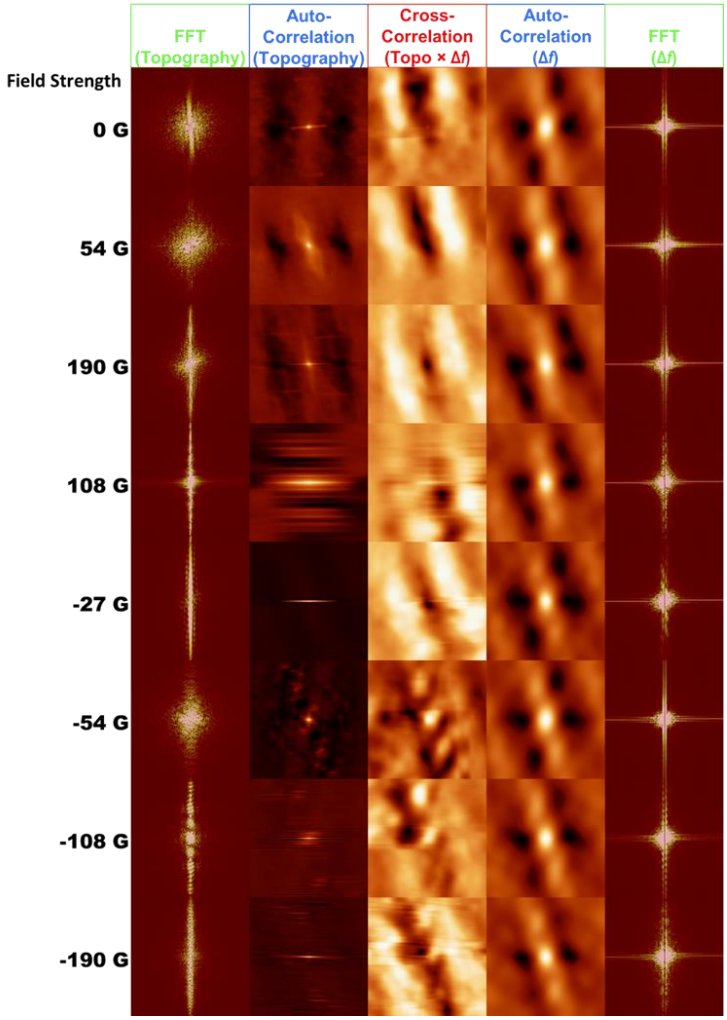

Figure 6.18 The field-dependent topography FFT, topography auto-correlation, cross-correlation of topographic and frequency shift images, frequency shift auto-correlation, and frequency shift FFT maps taken from the MFM image sequence in fig. 6.16.

6.3 Conclusions and Future Work

Our MFM data confirms that uniaxial anisotropy in this UMG develops at lower temperatures, likely influenced by ordering of U moments. Moments in UMG prefer to align along an easy axis that coincides with the *c*-axis of the material. Perhaps even more information regarding anisotropy and the distribution of stray field energy in UMG lies in

the repeated patterns and orientations of surface closure domains. Work is currently underway to devise a means to characterize this information using the MFM images presented in this work. But equally as vital will be constructing a micromagnetic model to simulate and extract information from surface closure domains sizes, shapes and distributions.

UMG becomes a harder (more anisotropic) magnet at low temperature, but the SQUID data lacks confirmation regarding the low field characteristics of the material. This can be addressed by further measurement with a single-crystal sample, preferably measured with the *c*-axis oriented parallel and perpendicular to the applied field. Based on the MFM data at 77 K, it appears that the low-field coercivity is small which supports the picture, however incomplete it may be, painted by the SQUID results. If there is this coexistence of magnetically hard and soft phases at low temperature with different susceptibilities depending on applied field we would need to access higher fields in future MFM measurements to probe the high-field characteristics of local magnetic domains. Because of the high stray fields in UMG, further MFM studies should employ low moment MFM probes.

A number of interesting avenues for continued research of UMG deal with synthesis. Coercivity enhancements in permanent magnetic materials like NdFeB, necessary to optimize them for industrial applications, were made possible by decreasing the size of single domains and by varying the compositions of grain boundaries between domains.[169] Similar enhancements may be possible for UMG. UMG becomes increasingly anisotropic at low temperatures due to distortion of the uranium sublattice and so synthesis under pressure has the potential to alter the ordering temperatures and anisotropy in the material. For this reason, synthesis of UMG under pressure may

produce intriguing results. In addition, magnetization measurements while applying pressure in the c-axis direction and alternatively in-plane would make a straightforward and rather interesting study in the future, especially with regard to probing the effect of reducing atomic separations on nearest-neighbor versus next-nearest neighbor interactions between uranium atoms.

Appendix

A. PI Controller for Fiber Piezo

The circuit (fig. A.1) provides proportional and integral feedback to maximize the DC portion of the interference signal given the cantilever deflection. Voltage followers stabilize the deflection input, the output of the reference voltage and the setpoint voltage. Rather than using the reference voltage to provide an offset, the offset is fed in directly from a 125 V source in series with the PI control output. In the original design the PI feedback and offset were fed in parallel into a PA08V high-voltage summing amplifier. The high-voltage summing amplifier in this design is entirely omitted. OP37's are widely available and provide low-noise and high-speed operation at relatively low cost. Diodes and a fuse protect the PI circuit.

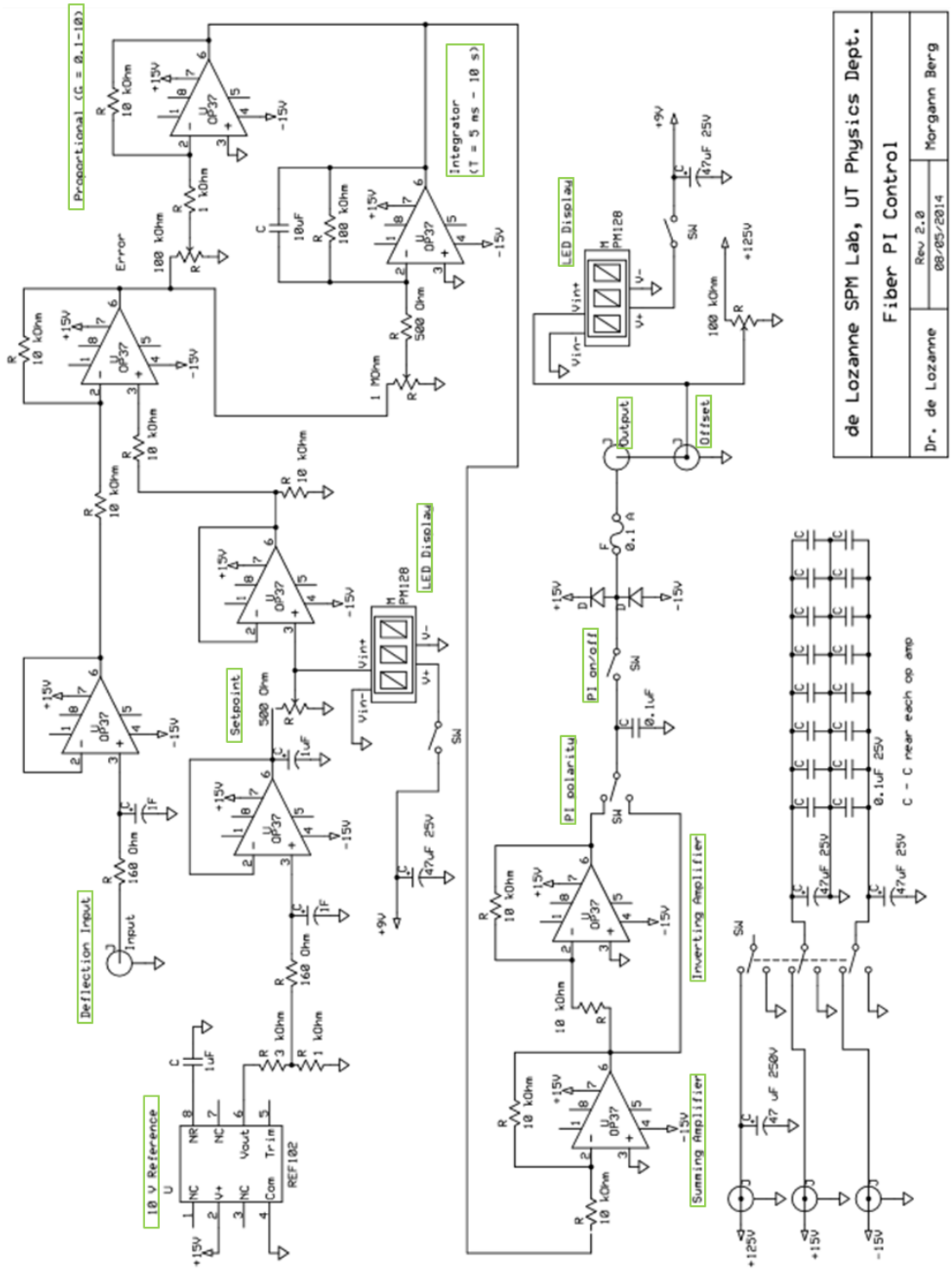

Figure A.1: Circuit diagram of PI Controller for fiber piezo.

Bibliography

1. J. R. Arthur Jr., J. Appl. Phys., 39, 4032 (1968).

2. A. Y. Cho, Surf. Sci., 17, 494 (1969).

3. DCA Instruments Oy, Turku, Finland.

4. Telemark, Battle Ground, WA.

5. Oxford Applied Research Ltd., Witney, Oxfordshire, United Kingdom.

6. STAIB INSTRUMENTS GmbH, Langenbach, Germany.

7. k-Space Associates, Inc., Dexter, MI.

8. P. Bodin, S. Sakai, and Y. Kasai, Jpn. J. Appl. Phys., 31, L949 (1992).

9. K. Iijima, T. Terashima, Y. Bando, K. Kamigaki, and H. Terauchi, J. Appl. Phys., 72, 2840 (1992).

10. J.H. Haeni, C.D. Theis, and D.G. Schlom, J. Electroceram., 4, 385 (2000).

11. K. Tsuchida, S. Takase, Y. Shimizu, Sens. Mater., 16 (3), 171-180, (2004).

12. H. J. Hwang, M. Awano, J. Eur. Ceram. Soc., 21, 2103 (2001).

13. C. S. Cheng, L. Zhang, Y. J. Zhang, S. P. Jiang, Solid State Ionics, 179, 282 (2008).

14. H. Ichinose, Y. Shiwa, M. Nagano, Jap. J. Appl. Phys., 33, 5907, (1994).

15. C. H. Chen, E. M. Kelder, J. Schoonman, J. Electrochem. Soc., 144 (11), L289 (1997).

16. B. Trummer, O. Fruhwirth, K. Reichmann, J. Eur. Ceram. Soc., 19, 827 (1999).

17. M. Losurdo, A. Sacchetti, P. Capezzuto, G. Bruno, L. Armelao, D. Barreca, G. Bottaro, A. Gasparotto, C. Maragno, E. Tondello, Appl. Phys. Lett., 87, 061909, (2005).

18. L. Armelao, D. Barreca, G. Bottaro, Chem. Mater., 17 (2), 427 (2005).

19. E. Bontempi, L. Armelao, D. Barreca, L. Bertolo, G. Bottaro, E. Pierangelo, L. E. Depero, Crys. Engr., 5, 291 (2002).

20. Y. F. Zhu, R. Q. Tan, L. L. Cao, Surf. Interface Anal., 32, 183 (2001).

21. Y. X. Zhang, Y. F. Zhu, X. Y. Ye, Surf. Interface Anal., 32, 310 (2001).

22. Q. X. Jia, T. M. McCleskey, A. K. Burrell, Y. Lin, G. E. Collis, H. Wang, A. D. Q. Li, S. R. Foltyn, Nat. Mat., 3, 529 (2004).

23. H. Liu,L. Shi, Y. Guo, J. Alloy. Compd., 594, 158 (2014).

24. P. H. T. Ngamou, K. Kohse-Hoeinghaus, N. Bahlawanea, J. Appl. Phys., 106, 073714 (2009).

25. L. Yingnan, L. Fenghua, S. Yue, Z. G. Fan, C. S. Li, Y. F. Lu, Rare Metal Mat. Eng., 40, 685 (2011).

26. J. W. Fergus, Sensor. Actuat. B- Chem., 123, 1169 (2007).

27. M. R. Catalano, R. G. Toro, A. Gulino, G. Malandrino, Surf. Coat. Tech., 230, 174 (2013).

28. E. L. Brosha, R. Mukundan, D. R. Brown, F. H. Garzon, J. H. Visser, M. Zanini, Z. Zhou, E. M. Logothetis, Sensor. Actuat. B- Chem., 69, 171 (2000).

29. E. Fischer, W. Shen, J. L. Hertz, J. Electroceram., 29, 262 (2012).

30. F. Capon, A. Boileau, C. Carteret, N. Martin, P. Boulet, J. F. Pierson, J. Appl. Phys., 114, 113510 (2013).

31. M. A. Torija, M. Sharma, M. R. Fitzsimmons, M. Varela, C. Leighton, J. Appl. Phys., 104, 023901 (2008).

32. J. Gazquez, W. Luo, M. P. Oxley, M. Prange, M. A. Torija, M. Sharma, C. Leighton, S. T. Pantelides, S. J. Pennycook, M. Varela, Nano Lett., 11 (3), 973 (2011).

33. M. A. Torija, M. Sharma, J. Gazquez, M. Varela, C. He, J. Schmitt, J. A. Borchers, M. Laver, S. El-Khatib, C. Leighton, Adv. Mater., 23 (24), 2711 (2011).

34. Q. X. Zhu, W. Wang, X. Q. Zhao, X. M. Li, Y. Wang, H. S. Luo, H. L. W. Chan, R. K. Zheng, J. Appl. Phys., 111, 103702 (2012).

35. S. G. Ghonge, E. Goo, R. Ramesh, R. Haakenaasen, D. K. Fork, Appl. Phys. Lett., 64, 3407 (1994).

36. J. Zippel, M. Lorenz, A. Setzer, G. Wagner, N. Sobolev, P. Esquinazi, M. Grundmann, Phys. Rev. B, 82, 125209 (2010).

37. P. S. Sankara Rama, Q. M. Ramasse, W. I. Liang, Y. H. Chu, V. Nagarajan, P. Munroe, J. Appl. Phys., 112, 104102 (2012).

38. V. Foglietti, N. Yang, A. Tebano, C. Aruta, E. Di Bartolomeo, S. Licoccia, C. Cantoni, G. Balestrino, Appl. Phys. Lett., 104, 081612 (2014).

39. M.N. Luckyanova, D. Chen, W. Ma, H. L. Tuller, G. Chen, B. Yildiz, Appl. Phys. Lett., 104, 061911 (2014).

40. M. Ozegowski, K. Meteva, S. Metev, G. Sepold, Appl. Surf. Sci., 138–139, 68 (1999).

41. D. Fuchs, E. Arac, T. Schwarz, R. Schneider, Advances in Solid State Physics Vol. 47 (Springer-Verlag, Berlin, 2008).

42. V. Mehta, Y. Suzuki, J. Appl. Phys., 109, 07D717 (2011).

43. V. Siruguri, S.K. Paranjpe, P. Raj, A. Sathyamoorthy, J.-P. Itié, A. Polian, Physica B, 344, 255 (2004)

44. F. Lihl, Z. Metallkd., 46, 434 (1955).

45. Quantum Design International, San Diego, CA.

46. H. K. Onnes, Proceedings of the Koninklijke Akademie Van Wetenschappen Te Amsterdam, 14, 818 (1912).

47. W. Meissner, R. Ochsenfeld, Naturwissenschaften, 21, 787 (1933).

48. C. J. Gorter. H. Casimir, Physica, 1, 306 (1934).

49. J. N. Rjabinin, L.W. Schubnikow, Nature, 135(3415), 581 (1935).

50. F. London, H. London, P. Roy. Soc. A- Math. Phy., 149(866), 71 (1935).

51. F. London, Superfluids (Wiley, New York, 1950).

52. B. D. Josephson, Physics Letters, 1(7), 251 (1962).

53. R. Feynman, R. B. Leighton, M. Sands, The Feynman Lectures on Physics Vol. 3 (Addison–Wesley, Reading, 1965).

54. H. Ibach, H. Lüth, Solid-State Physics: An Introduction to Principles of Materials Science (Springer-Verlag, Berlin Heidelberg, 2nd ed., 1995).

55. R. C. Jaklevic, J. Lambe, A. H. Silver, J. E. Mercereau, Phys. Rev. Lett., 12, 159 (1964).

56. R. C. Jaklevic, J. Lambe, J. E. Mercereau, A. H. Silver, Phys. Rev., 140, A1628 (1965).

57. G. Binnig, H. Rohrer, "Scanning tunneling microscope," U.S. Patent: 4 343 993 A, issued August 10, 1982.

58. G. Binnig, H. Rohrer, Sci. Am., 253(2), 50 (1985).

59. G. Binnig, C. F. Quate, Ch. Gerber, Phys. Rev. Lett., 56, 930 (1986).

60. G. Binnig, H. Rohrer, Ch. Gerber, E. Weibel, Phys. Rev. Lett., 49(1), 57 (1982).

61. F.J. Giessibl, G. Binnig, Ultramicroscopy, 42-44(1), 281 (1992).

62. M. J. Yoo, T. A. Fulton, H. F. Hess, R. L. Willett, L. N. Dunkleberger, R. J. Chichester, L. N. Pfeiffer, K. W. West, Science, 276(5312), 579 (1997).

63. H.J. Mamin, R. Budakian, B.W. Chui, D. Rugar, Phys. Rev. B, 72, 024413 (2005).

64. Jeehoon Kim, L. Civale, E. Nazaretski, N. Haberkorn, F. Ronning, A. S. Sefat, T. Tajima, B. H. Moeckly, J. D. Thompson and R. Movshovich, Supercond. Sci. Technol., 25, 112001 (2012).

65. Q. Lu, K. Mochizuki, J. T. Markert, A. de Lozanne, Physica C, 371, 146 (2002).

66. H. W. Hao, A. M. Baró, J. J. Sáenz, J. Vac. Sci. Technol. B, 9, 1323 (1991).

67. E. Meyer, R. Lüthi, L. Howald, H.-J. Güntherodt, "Friction Force Microscopy", Forces in Scanning Probe Methods, NATO ASI Series E: Applied Sciences Vol. 286, Eds. H.-J. Guntherodt, D. Anselmetti, E. Meyer (Dordrecht, Kluwer Academic Publishers, 1995), p. 285.

68. F. J. Giessibl, Rev. Mod. Phys. 75, 949 (2003).

69. U. Hartmann, Phys. Lett. A, 137(9), 475 (1989).

70. T. R. Albrecht, P. Grütter, D. Horne, D. Rugar, J. Appl. Phys., 69, 668 (1991).

71. M. Born, E. Wolf, Principles of Optics: Electromagnetic Theory of Propagation of Interference and Diffraction of Light, 6th ed., (Pergamon Press, Oxford, 1980).

72. G. P. Agrawal, N. K. Dutta, Semiconductor Lasers, 2nd ed., (Van Nostrand-Reinhold, New York, 1993).

73. D. Sarid, Scanning Force Microscopy: with Applications to Electric, Magnetic and Atomic Forces, Oxford Series in Optical & Imaging Sciences 5, (Oxford University Press, New York, 1991).

74. T. M. Chuang, A. L. de Lozanne, Rev. Sci. Instrum., 78(5), 053710 (2007).

75. F. J. Giessibl, B. M. Trafas, Rev. Sci. Instrum., 65, 1923 (1994).

76. D. Rugar, H. J. Mamin, P. Guethner, Appl. Phys. Lett., 55, 2588 (1989).

77. S. H. Pan, E. W. Hudson, and J. C. Davis, Rev. Sci. Instrum., 70, 1459 (1999).

78. L. Chen, S. H. Kim, A. K. Lee, A. de Lozanne, Rev. Sci. Instrum., 83, 013708 (2012).

79. G. H. Jonker, J. H. Van Santen, Physica, 16(3), 337 (1950).

80. R. J. Cava, B. Batlogg, R. B. van Dover, D. W. Murphy, S. Sunshine, T. Siegrist, J. P. Remeika, E. A. Rietman, S. Zahurak, G. P. Espinosa, Phys. Rev. Lett., 58(16) 1676 (1987).

81. D. J. Singh, J. Appl. Phys., 79(8), 4818 (1996).

82. J. Wang, J. B. Neaton, H. Zheng, V. Nagarajan, S. B. Ogale, B. Liu, D. Viehland, V. Vaithyanathan, D. G. Schlom, U. V. Waghmare, N. A. Spaldin, K. M. Rabe, M. Wuttig, R. Ramesh, Science, 299(5613), 1719 (2003).

83. G. Briceño, H. Chang, X. Sun, P. G. Schultz, X. D. Xiang, Science, 270(5234), 273 (1995).

84. P. G. Radaelli, S. W. Cheong, Phys. Rev. B, 66, 094408 (2002).

85. K. Knížek Z. Jirák, J. Hejtmánek, M. Veverka, M. Maryško, G. Maris, T. T. M. Palstra, Eur. Phys. J. B, 47, 213 (2005).

86. K. Asai, P. Gehring, H. Chou, G. Shirane, Phys. Rev. B, 40, 10982 (1989).

87. M. Abbate, J. C. Fuggle, A. Fujimori, L. H. Tjeng, C. T. Chen, R. Potze, G. A. Sawatzky, H. Eisaki, S. Uchida, Phys. Rev. B, 47, 16124 (1993).

88. M. Abbate, R. Potze, G. A. Sawatzky, A. Fujimori, Phys. Rev. B, 49, 7210 (1994).

89. S. Yamaguchi, Y. Okimoto, Y. Tokura, Phys. Rev. B, 54(16), 11022 (1996).

90. S.M. Zhou, L. Shi, J. Zhao, L. He, H. Yang, S. Zhang, Phys. Rev. B, 76, 172407 (2007).

91. N. Orlovskaya, Y. Gogotsi, M. Reece, B. Cheng, I. Gibson, Acta. Mater., 50(4), 715 (2002).

92. A. Aman, Y. Chen, M. Lugovy, N. Orlovskaya, M. J. Reece, D. Ma, A. D. Stoica, Ke An, J. Appl. Phys., 116, 013503 (2014).

93. J. Q. Yan, J. S. Zhou, J. B. Goodenough, Phys. Rev. B, 70, 014402 (2004).

94. S.R. Giblin, I. Terry, S. J. Clark, T. Prokscha, D. Prabhakaran, A. T. Boothroyd, J. Wu, C. Leighton, Europhys. Lett., 70, 677 (2005).

95. A. Harada, T. Taniyama, Y. Takeuchi, T. Sato, T. Kyômen, M. Itoh, Phys. Rev. B, 75, 184426 (2007).

96. J. Androulakis, N. Katsarakis, J. Giapintzakis, J. Phys. Rev. B, 64, 174401 (2001).

97. L. Armelao, D. Barreca, G. Bottaro, C. Maragno, E. Tondello, A. Caneschi, C. Sangregorio, S. Gialanella, J. Nanosci. Nanotechnol., 6(4), 1060 (2006).

98. Y. Wang, H.J. Fan, J. Appl. Phys,, 108, 053917 (2010).

99. S. Zhou, L. He, S. Zhao , Y. Guo, J. Zhao, L. Shi, J. Phys. Chem. C, 113(31), 13522 (2009).

100. D. Fuchs, C. Pinta, T. Schwarz, P. Schweiss, P. Nagel, S. Schuppler, R. Schneider, M. Merz, G. Roth, H. v. Löhneysen, Phys. Rev. B, 75, 144402 (2007).

101. J.W. Freeland, J. X. Ma, J. Shi, Appl. Phys. Lett., 93, 212501 (2008).

102. A. Herklotz, A. D. Rata, L. Schultz, K. Dörr, Phys. Rev. B, 79, 092409 (2009).

103. V.V. Mehta, M. Liberati, F. J. Wong, R. V. Chopdekar, E. Arenholz, Yuri Suzuki, J. Appl. Phys., 105, 07E503 (2009).

104. A.D. Rata, A. Herklotz, L. Schultz, K. Dörr, Euro. Phys. J. B, 76(2), 215 (2010).

105. A. Posadas, M. Berg, H. Seo, D.J. Smith, A.P. Kirk, D. Zhernokletov, R.M. Wallace, A. de Lozanne, A. A. Demkov, Microelectron. Eng., 88(7), 1444 (2011).

106. S.W. Kim, J. Lee, Integr. Ferroelectr., 18(1-4), 405 (1997).

107. E.L. Brosha, R Mukundan, D. R Brown, F. H. Garzon, J. H. Visser, M. Zanini, Z. Zhou, E. M. Logothetis, Sensor. Actuat. B-Chem., 69(1-2), 171 (2000).

108. C. Hu, K. W. Park, A. Posadas, J. L. Jordan-Sweet, A. A. Demkov, E. T. Yu, J. Appl. Phys., 114, 183909 (2013).

109. D. Fuchs, E. Arac, T. Schwarz, R. Schneider, Advances in Solid State Physics Vol. 47 (Springer-Verlag, Berlin, 2008).

110. K. Gupta, P. Mahadevan, Phys. Rev. B, 79, 020406 (2009).

111. C. Pinta, D. Fuchs, M. Merz, M. Wissinger, E. Arac, H. v. Löhneysen, A. Samartsev, P. Nagel, and S. Schuppler, Phys. Rev. B, 78, 174402 (2008).

112. D. Fuchs, E. Arac, C. Pinta, S. Schuppler, R. Schneider, H. v. Löhneysen, Phys. Rev. B, 77, 014434 (2008).

113. R.F. Klie, T. Yuan, M. Tanase, G. Yang, Q. Ramasse, Appl. Phys. Lett., 96, 082510 (2010).

114. G.E. Sterbinsky, P. J. Ryan, J. W. Kim, E. Karapetrova, J. X. Ma, J. Shi, J. C. Woicik, Phys. Rev. B, 85, 020403 (2012).

115. H. Seo, A. Posadas, A. A. Demkov, Phys. Rev. B, 86, 014430 (2012).

116. W. S. Choi, J. H. Kwon, H. Jeen, J. E. Hamann-Borrero, A. Radi, S. Macke, R. Sutarto, F. He, G. A. Sawatzky, V. Hinkov, M. Kim, H. N. Lee, Nano Lett., 12, 4966 (2012).

117. H.F. Liu, L. Shi, Y. Guo, S. Zhou, J. Zhao, C. Wang, L. He, Y. Lia, J. Alloy. Compd,, 594, 158 (2014).

118. H.F. Liu, L. Shia, S. Zhou, J. Zhao, Y. Guo, C. Wanga, L. Hea, Surf. Coat. Tech., 226, 108 (2013).

119. D. Fuchs, L. Dieterle, E. Arac, R. Eder, P. Adelmann, V. Eyert, T. Kopp, R. Schneider, D. Gerthsen, H. v. Löhneysen, Phys. Rev. B, 79, 024424 (2009).

120. J. Rondinelli, N. A. Spaldin, Phys. Rev. B, 79, 054409 (2009).

121. H. Hsu, P. Blaha, R. M. Wentzcovitch, Phys. Rev. B, 85, 140404 (2012).

122. M. R. Catalano, R. G. Toro, A. Gulino, G. Malandrino, Surf. Coat. Tech., 230, 174 (2013).

123. M. Itoh, I. Natori, S. Kubota, K. Motoya, J. Phys. Soc. Jpn., 63, 1486 (1994).

124. M.A. Señarís-Rodríguez, J.B. Goodenough, J. Solid State Chem., 118(2), 323 (1995).

125. Y. Wang, H. J. Fan, Acta Mater., 60(3), 1238, (2012).

126. S. Park, P. Ryan, E. Karapetrova, J. W. Kim, J. X. Ma, J. Shi, J. W. Freeland, W. Wu, Appl. Phys. Lett., 95, 072508 (2009).

127. V. Mehta, Y. Suzuki, J. Appl. Phys., 109, 07D717 (2011).

128. Z. H. Wang, O. I. Lebedev, G. Van Tendeloo, G. Cristiani, H. U. Habermeier, Phys. Rev. B, 77, 115330 (2008).

129. J. Gazquez, W. Luo, M. P. Oxley, M. Prange, M. A. Torija, M. Sharma, C. Leighton, S. T. Pantelides, S. J. Pennycook, M. Varela, Nano Lett., 11 (3), 973 (2011).

130. Y. M. Kim, J. He, M. D. Biegalski, H. Ambaye, V. Lauter, H. M. Christen, S. T. Pantelides, S. J. Pennycook, S. V. Kalinin, A. Y. Borisevich, Nat. Mat., 11, 888 (2012).

131. W. S. Choi, J. H. Kwon, H. Jeen, J. E. Hamann-Borrero, A. Radi, S. Macke, R. Sutarto, F. He, G. A. Sawatzky, V. Hinkov, M. Kim, H. N. Lee , Nano Lett., 12, 4966 (2012).

132. N. Biškup, J. Salafranca, V. Mehta, M. P. Oxley, Y. Suzuki, S. J. Pennycook, S. T. Pantelides, M. Varela, Phys. Rev. Lett., 112, 087202 (2014).

133. Ferreira, P. J., Department of Mechanical Engineering, University of Texas at Austin, Austin, TX. Personal communication, August 2014.

134. D. B. Williams, C. B. Carter, Transmission Electron Microscopy: A Textbook for Materials Science, 2nd ed., (Springer, New York, 2008).

135. A. Kushima, S. Yip, B. Yildiz, Phys. Rev. B, 82, 115435 (2010).

136. A. Posadas, M. Berg, H. Seo, A. de Lozanne, A. A. Demkov, D. J. Smith, A. P. Kirk, D. Zhernokletov, R. M. Wallace, Appl. Phys. Lett., 98, 053104 (2011).

137. H. Li, X. Hu, Y. Wei, Z. Yu, X. Zhang, R. Droopad, A.A. Demkov, J. Edwards, K. Moore, W. Ooms, J. Kulik, P. Fejes, J. Appl. Phys., 93, 4521 (2003).

138. F. Niu, B. W. Wessels, J. Vac. Sci. Technol. B, 25, 1053 (2007).

139. A. A. Demkov, X. Zhang, J. Appl. Phys. 103, 103710 (2008).

140. Y. Wei, X. Hu, Y. Liang, D.C. Jordan, B. Craigo, R. Droopad, Z. Yu, A.A. Demkov, J.L. Edwards, W.J. Ooms, J. Vac. Sci. Technol. B, 20 1402 (2002).

141. T. Q. Ngo, A. B. Posadas, M. D. McDaniel, C. Hu, J. Bruley, E. T. Yu, A. A. Demkov, J. G. Ekerdt, Appl. Phys. Lett., 104, 082910 (2014).

142. B.V. Crist, Handbook of Monochromatic XPS Spectra, 3 vols., (Wiley, New York, 2000).

143. C.A.F. Vaz, D. Prabhakaran, E.I. Altman, V.E. Henrich, Phys. Rev. B, 80, 155457 (2009).

144. K. Bolwin, W. Schnurnberger, G. Schiller, Z. Phys. B, 72, 203 (1998).

145. M.M. Natile, A. Galenda, A. Glisneti, Surf. Sci. Spectra, 15, 1 (2008).

146. T. Zhao, F. Chen, H. Lu, G. Yang, Z. Chen, J. Appl. Phys., 87, 7442 (2000).

147. E. Nazaretski, K. S. Graham, J. D. Thompson, J. A. Wright, D. V. Pelekhov, P. C. Hammel, R. Movshovich, Rev. Sci. Instrum., 80, 083704 (2009).

148. N. A. Pertsev, A. G. Zembilgotov, A. K. Tagantsev, Phys. Rev. Lett., 80, 1988 (1998).

149. $(a_{p\text{-}s})_{STO,\ 300K}$ = 3.905 Å, $(\alpha)_{STO\text{-}Si}$ = 5.4 x 10^{-5} K^{-1}, $(a_{p\text{-}s})_{BTO,\ 300K}$ = 4.006 Å, $(\alpha)_{BTO}$ = 10.1 x 10^{-6} K^{-1}

150. J. Wu, C. Leighton, Phys. Rev. B, 67, 174408 (2003).

151. M. A. Señarís-Rodríguez, J. B. Goodenough, J. Solid State Chem., 118, 323 (1995).

152. M. A. Gîrţu, C. M. Wynn, W. Fujita, K. Awaga, A. J. Epstein, Phys. Rev. B, 61, 4117 (2000).

153. U.S. Department of Energy Advanced Research Projects Agency, REACT | ARPA-E, http://www.arpa-e.energy.gov/?q=arpa-e-programs/react, (accessed Aug 23, 2014).

154. D. J. Hykel, C. Paulsen, D. Aoki, J. R. Kirtley, K. Hasselbach, Phys. Rev. B 90, 184501 (2014).

155. S. S. Saxena, P. Agarwal, K. Ahilan, F. M. Grosche, R. K. W. Haselwimmer, M. J. Steiner, E. Pugh, I. R. Walker, S. R. Julian, P. Monthoux, G. G. Lonzarich, A. Huxley, I. Sheikin, D. Braithwaite , J. Flouquet, Nature 406, 587 (2000).

156. T. Hattori, Y. Ihara, Y. Nakai, K. Ishida, Y. Tada, S. Fujimoto, N. Kawakami, E. Osaki, K. Deguchi, N. K. Sato, I. Satoh, Phys. Rev. Lett., 108, 066403 (2012).

157. D. Aoki, A. Huxley, E. Ressouche, D. Braithwaite, J. Flouquet, J. Brison, E. Lhotel, C. Paulsen, Nature 413, 613 (2001).

158. A. Budkowski, A. Szytula, Z. Ban, Croat Chem Acta, 62 (1), 51 (1989).

159. G. Venturini, B. Malaman, J. Alloy. Compd., 235, 201 (1996).

160. S. K. Paranjpe, V. Siruguri, P. Raj, A. Sathyamoorthy, T. V. Chandrasekhar Rao, Physica B, 385-386, 366 (2006).

161. V. Siruguri, S. K. Paranjpe, P. Raj, A. Sathyamoorthy, J.-P. Itié, A. Polian, Physica B, 344, 255 (2004).

162. J.-P. Itié, J. Staun Olsen, L. Gerward, U. Benedict, J.C. Spirlet, Physica B, 139–140, 330 (1986).

163. S. F. Matar, V. Siruguri, J. Alloy. Compd., 436, 34 (2007).

164. R. S. Chaughule, R. Nagarajan, L. C. Gupta, R. Vijayaraghavan, A. D. Kulkarni, P. Raj, P. Suryanarayana, A. Sathyamoorthy, K. Shashikala, R. J. Begum, J Alloy. Compd., 178, 385 (1992).

165. P. P. J. van Engelen, D. B. de Mooij, K. H. J. Buschow, IEEE T. Magn., 24 (2), 1728 (1988).

166. R. D. Kirby, J. X. Shen, J. A.Woollam, D. J. Sellmyer, J. Appl. Phys., 69, 4574 (1991).

167. M. Ślaski, T. Laegrid, K. Fossheim, Z. Tomkowicz, A. Szytula, J. Alloy. Compd., 178 (1), 249 (1992).

168. A. Hubert, R. Schäfer, Magnetic Domains (Springer, Heidelberg, 1998).

169. G. C. Hadjipanayis, J. Mag. Magn. Mater., 200, 373 (1999).